



POZNAŃ UNIVERSITY OF TECHNOLOGY

DOCTORAL THESIS

Method for direct noise analysis of transonic axial compressor blade

Author:

MSc. Eng. Jędrzej MOSIEŻNY

Supervisor:

Prof. DSc. Eng. Michał CIAŁKOWSKI

*A thesis submitted in fulfilment of the requirements
for the degree of Doctor of Philosophy. Engineer.*

in the

Faculty of Work Machines and Transportation
Chair of Thermal Engineering

September 18, 2018

Declaration of Authorship

I, MSc. Eng. Jędrzej MOSIEŻNY, declare that this thesis titled, 'Method for direct noise analysis of transonic axial compressor blade' and the work presented in it are my own. I confirm that:

- This work was done wholly or mainly while in candidature for a research degree at this University.
- Where any part of this thesis has previously been submitted for a degree or any other qualification at this University or any other institution, this has been clearly stated.
- Where I have consulted the published work of others, this is always clearly attributed.
- Where I have quoted from the work of others, the source is always given. With the exception of such quotations, this thesis is entirely my own work.
- I have acknowledged all main sources of help.
- Where the thesis is based on work done by myself jointly with others, I have made clear exactly what was done by others and what I have contributed myself.

Signed:

Date:

Abstract

This thesis proposes a method of assessing flow generated noise in transonic flows by direct formulation.

First a steady state Reynolds Averaged Navier-Stokes analysis of NASA R67 transonic axial compressor is performed as a validation study of the mesh and numerical setup. The result of the steady state analysis is then used as an initialization for transient DDES analysis performed on high quality, 11 million cells hexagonal mesh. The transient analysis covers 0.05s of physical flow time, which corresponds to about 800 revolutions of the rotor. Both steady state and transient simulations are performed on PL-Grid HPC infrastructure.

Transient results are analyzed with an in-house build program. The program uses information about static pressure, transient particle velocity and vorticity from each timestep. This data is then postprocessed into sound pressure levels, sound frequency and effective sound power level.

Information on generation of sound phenomena occurring in the blade passage are gathered from direct formulation and may be used as a validation case for FW-H or other computational aeroacoustic analogies dealing with flows in transonic regimes in rotating machinery.

Acknowledgements

In this place I would like to thank the Chair of Thermal Engineering of Poznań University of Technology, with special recognition to MSc. Eng. Bartosz Ziegler and PhD Eng. Przemysław Grzymisławski for thorough scientific and personal support during this project.

A big recognition goes to the owners and maintainers of the PLGRID - Polish HPC infrastructure, especially team in HPC Cyfronet center in AGH University of Science and Technology in Kraków. Being able to use the state of the art HPC clusters for analyses made this project possible.

Contents

Declaration of Authorship	iii
Abstract	v
Acknowledgements	vii
Contents	ix
List of Figures	xi
List of Tables	xv
Abbreviations	xvii
Symbols	xix
1 Introduction	1
1.1 Main Section 1	1
1.1.1 Subsection 1	1
1.1.2 Subsection 2	1
1.2 Main Section 2	2
2 Current research on Computational Aeroacoustics	3
2.1 Classification of CAA methods	3
2.2 Lighthill-Curle theory of aerodynamic sound	4
2.3 FW-H Analogy	6
2.4 Limitations to acoustic analogies	9
3 Approach and direct formulation of noise analysis	11
3.1 Direct formulation of noise analysis	11
3.2 CFD analysis requirements	13
3.2.1 Governing equations	14
3.2.2 Direct Numerical Simulation	14
3.2.3 Large Eddy Simulation	15
3.2.4 Reynolds Averaged Navier Stokes	18
3.2.5 Hybrid RANS/LES Methods	20
3.3 Mesh sizing requirements	22
3.4 Timestep requirements	25
3.5 Limiting factors of the direct approach	26

4 Test case	27
4.1 NASA Rotor 67 transonic axial compressor	27
4.2 3D geometry preparation	28
4.3 Meshing approach	30
5 CFD Analysis	35
5.1 Case preprocessing	35
5.2 Flowfield initialization & RANS	36
5.3 DDES analysis	38
5.4 Validation of the results	40
6 Results of flow field noise analysis	43
6.1 Transition from flow-field to sound signal data	43
6.2 RMS results	43
6.2.1 Results postprocessing	43
6.2.2 Qualitative analysis	44
6.3 FFT results	46
6.3.1 Results postprocessing	46
6.3.2 Qualitative analysis	47
7 Conclusions & Further work	49
7.1 Results discussion	49
7.2 Improvements to the method	50
7.3 Further work	51
7.4 Closing remarks	52
A RMS values plots	53
B FFT plots	81
C CFD validation	111
D Code for direct formulation of noise analysis	123
E Folder Structure	125
F Code for RMS computation	127
G Code for discrete Fourier analysis	129
H Blade design surface coordinates	131
Bibliography	145

List of Figures

3.1	Resolving eddies in different kinds of CFD analyses	14
3.2	Scenario 1. Wavelength smaller than cell edge length	23
3.3	Scenario 2. Wavelength equal to cell edge length	23
3.4	Scenario 3. Wavelength equal four minimum edge lengths	24
3.5	Scenario 4. Wavelength larger than four minimum edge lengths	24
4.1	Geometry of NASA R67	27
4.2	Final single passage geometry. Some features hidden for clarity	30
4.3	Mesh topology with conforming periodic boundaries	31
4.4	Mesh h-topology	31
4.5	Mesh non-orthogonality histogram	33
4.6	Completed Mesh	33
5.1	Flowchart of the PISO algorithm	39
5.2	Schematic representation of constant pitch (left) and constant chord (right) to plot data [17]	41
5.3	Inlet pressure validation	41
5.4	Outlet pressure validation	42
6.1	Tip gap streamlines. Velocity in [m/s]	45
6.2	Exemplary FFT heatmap of magnitude. Random data.	47
A.1	Blade surface RMS Sound pressure [Pa]	53
A.2	Blade surface RMS SPLdB [dB]	54
A.3	RMS Sound pressure at int-01 mark	55
A.4	RMS Sound pressure decibel level at int-01 mark	55
A.5	RMS Sound intensity at int-01 mark	56
A.6	RMS Sound intensity decibel level at int-01 mark	56
A.7	RMS Sound pressure at int-02 mark	57
A.8	RMS Sound pressure decibel level at int-02 mark	57
A.9	RMS Sound intensity at int-02 mark	58
A.10	RMS Sound intensity decibel level at int-02 mark	58
A.11	RMS Sound pressure at int-03 mark	59
A.12	RMS Sound pressure decibel level at int-03 mark	59
A.13	RMS Sound intensity at int-03 mark	60
A.14	RMS Sound intensity decibel level at int-03 mark	60
A.15	RMS Sound pressure at int-04 mark	61
A.16	RMS Sound pressure decibel level at int-04 mark	61
A.17	RMS Sound intensity at int-04 mark	62

A.18 RMS Sound intensity decibel level at int-04 mark	62
A.19 RMS Sound pressure at int-05 mark	63
A.20 RMS Sound pressure decibel level at int-05 mark	63
A.21 RMS Sound intensity at int-05 mark	64
A.22 RMS Sound intensity decibel level at int-05 mark	64
A.23 RMS Sound pressure at int-06 mark	65
A.24 RMS Sound pressure decibel level at int-06 mark	65
A.25 RMS Sound intensity at int-06 mark	66
A.26 RMS Sound intensity decibel level at int-06 mark	66
A.27 RMS Sound pressure at int-07 mark	67
A.28 RMS Sound pressure decibel level at int-07 mark	67
A.29 RMS Sound intensity at int-07 mark	68
A.30 RMS Sound intensity decibel level at int-07 mark	68
A.31 RMS Sound pressure at int-08 mark	69
A.32 RMS Sound pressure decibel level at int-08 mark	69
A.33 RMS Sound intensity at int-08 mark	70
A.34 RMS Sound intensity decibel level at int-08 mark	70
A.35 RMS Sound pressure at int-09 mark	71
A.36 RMS Sound pressure decibel level at int-09 mark	71
A.37 RMS Sound intensity at int-09 mark	72
A.38 RMS Sound intensity decibel level at int-09 mark	72
A.39 RMS Sound pressure at int-10 mark	73
A.40 RMS Sound pressure decibel level at int-10 mark	73
A.41 RMS Sound intensity at int-10 mark	74
A.42 RMS Sound intensity decibel level at int-10 mark	74
A.43 RMS Sound pressure at int-11 mark	75
A.44 RMS Sound pressure decibel level at int-11 mark	75
A.45 RMS Sound intensity at int-11 mark	76
A.46 RMS Sound intensity decibel level at int-11 mark	76
A.47 RMS Sound pressure at int-12 mark	77
A.48 RMS Sound pressure decibel level at int-12 mark	77
A.49 RMS Sound intensity at int-12 mark	78
A.50 RMS Sound intensity decibel level at int-12 mark	78
A.51 RMS Sound pressure at int-tip mark	79
A.52 RMS Sound pressure decibel level at int-tip mark	79
A.53 RMS Sound intensity at int-tip mark	80
A.54 RMS Sound intensity decibel level at int-tip mark	80
B.1 Blade surface amplitude weighted average frequency [dB]	81
B.2 Blade surface frequency of peak amplitude[Hz]	82
B.3 Blade surface peak amplitude [dB]	83
B.4 Spectrum plot at int-01 mark	84
B.5 Amplitude weighted average frequency at int-01 mark	84
B.6 Peak amplitude frequency int-01 mark	85
B.7 Peak magnitude at int-01 mark	85
B.8 Spectrum plot at int-02 mark	86
B.9 Amplitude weighted average frequency at int-02 mark	86

B.10 Peak amplitude frequency int-02 mark	87
B.11 Peak magnitude at int-02 mark	87
B.12 Spectrum plot at int-03 mark	88
B.13 Amplitude weighted average frequency at int-03 mark	88
B.14 Peak amplitude frequency int-03 mark	89
B.15 Peak magnitude at int-03 mark	89
B.16 Spectrum plot at int-04 mark	90
B.17 Amplitude weighted average frequency at int-04 mark	90
B.18 Peak amplitude frequency int-04 mark	91
B.19 Peak magnitude at int-04 mark	91
B.20 Spectrum plot at int-05 mark	92
B.21 Amplitude weighted average frequency at int-05 mark	92
B.22 Peak amplitude frequency int-05 mark	93
B.23 Peak magnitude at int-05 mark	93
B.24 Spectrum plot at int-06 mark	94
B.25 Amplitude weighted average frequency at int-06 mark	94
B.26 Peak amplitude frequency int-06 mark	95
B.27 Peak magnitude at int-06 mark	95
B.28 Spectrum plot at int-07 mark	96
B.29 Amplitude weighted average frequency at int-07 mark	96
B.30 Peak amplitude frequency int-07 mark	97
B.31 Peak magnitude at int-07 mark	97
B.32 Spectrum plot at int-08 mark	98
B.33 Amplitude weighted average frequency at int-08 mark	98
B.34 Peak amplitude frequency int-08 mark	99
B.35 Peak magnitude at int-08 mark	99
B.36 Spectrum plot at int-09 mark	100
B.37 Amplitude weighted average frequency at int-09 mark	100
B.38 Peak amplitude frequency int-09 mark	101
B.39 Peak magnitude at int-09 mark	101
B.40 Spectrum plot at int-10 mark	102
B.41 Amplitude weighted average frequency at int-10 mark	102
B.42 Peak amplitude frequency int-10 mark	103
B.43 Peak magnitude at int-10 mark	103
B.44 Spectrum plot at int-11 mark	104
B.45 Amplitude weighted average frequency at int-11 mark	104
B.46 Peak amplitude frequency int-11 mark	105
B.47 Peak magnitude at int-11 mark	105
B.48 Spectrum plot at int-12 mark	106
B.49 Amplitude weighted average frequency at int-12 mark	106
B.50 Peak amplitude frequency int-12 mark	107
B.51 Peak magnitude at int-12 mark	107
B.52 Spectrum plot at int-tip mark	108
B.53 Amplitude weighted average frequency at int-tip mark	108
B.54 Peak amplitude frequency int-tip mark	109
B.55 Peak magnitude at int-tip mark	109

C.1	Relative Mach number at S10P20 streamline	111
C.2	Relative velocity angle at S10P20 streamline	111
C.3	Relative Mach number at S10P50 streamline	112
C.4	Relative velocity angle at S10P50 streamline	112
C.5	Relative Mach number at S10P80 streamline	113
C.6	Relative velocity angle at S10P80 streamline	113
C.7	Relative Mach number at S50P20 streamline	114
C.8	Relative velocity angle at S50P20 streamline	114
C.9	Relative Mach number at S50P50 streamline	115
C.10	Relative velocity angle at S50P50 streamline	115
C.11	Relative Mach number at S50P80 streamline	116
C.12	Relative velocity angle at S50P80 streamline	116
C.13	Relative Mach number at S90P20 streamline	117
C.14	Relative velocity angle at S90P20 streamline	117
C.15	Relative Mach number at S90P50 streamline	118
C.16	Relative velocity angle at S90P50 streamline	118
C.17	Relative Mach number at S90P80 streamline	119
C.18	Relative velocity angle at S90P80 streamline	119
C.19	RANS Mach number contour plot at int-01 mark	120
C.20	DDES Mach number contour plot at int-01 mark	120
C.21	RANS Mach number contour plot at int-07 mark	121
C.22	DDES Mach number contour plot at int-07 mark	121
C.23	RANS Mach number contour plot at int-12 mark	122
C.24	DDES Mach number contour plot at int-12 mark	122

List of Tables

3.1	Test case boundary conditions	24
4.1	Basic R67 parameters	28
4.2	Location of compressor desing surfaces	32
5.1	Standard air properties	35
5.2	Test case boundary conditions	36
H.1	int-00 coordinates	131
H.2	int-01 coordinates	132
H.3	int-02 coordinates	133
H.4	int-03 coordinates	134
H.5	int-04 coordinates	135
H.6	int-05 coordinates	136
H.7	int-06 coordinates	137
H.8	int-07 coordinates	138
H.9	int-08 coordinates	139
H.10	int-09 coordinates	140
H.11	int-10 coordinates	141
H.12	int-11 coordinates	142
H.13	int-12 coordinates	143
H.14	int-tip coordinates	144

Abbreviations

CAA	Computational Aero Acoustics
CFD	Computational Fluid Dynamics
DDES	Delayed Detached Eddy Simulation
DES	Detached Eddy Simulation
HPC	Hight Power Computing
LES	Large Eddy Simulation
N-S	Navier Stokes
SRS	Scale Rresolving Simulation

Symbols

a	distance	m
P	power	W (Js ⁻¹)
ω	angular frequency	rads ⁻¹

To my wife. For limitless patience. . .

Chapter 1

Introduction

1.1 Main Section 1

Loreum ipsum dolor sit amet, consectetur adipiscing elit. Aliquam ultricies lacinia euismod. Nam tempus risus in dolor rhoncus in interdum enim tincidunt. Donec vel nunc neque. In condimentum ullamcorper quam non consequat. Fusce sagittis tempor feugiat. Fusce magna erat, molestie eu convallis ut, tempus sed arcu. Quisque molestie, ante a tincidunt ullamcorper, sapien enim dignissim lacus, in semper nibh erat lobortis purus. Integer dapibus ligula ac risus convallis pellentesque.

Loreum ipsum dolor sit amet, consectetur adipiscing elit. Aliquam ultricies lacinia euismod. Nam tempus risus in dolor rhoncus in interdum enim tincidunt. Donec vel nunc neque. In condimentum ullamcorper quam non consequat. Fusce sagittis tempor feugiat. Fusce magna erat, molestie eu convallis ut, tempus sed arcu. Quisque molestie, ante a tincidunt ullamcorper, sapien enim dignissim lacus, in semper nibh erat lobortis purus. Integer dapibus ligula ac risus convallis pellentesque.

1.1.1 Subsection 1

Nunc posuere quam at lectus tristique eu ultrices augue venenatis. Vestibulum ante ipsum primis in faucibus orci luctus et ultrices posuere cubilia Curae; Aliquam erat volutpat. Vivamus sodales tortor eget quam adipiscing in vulputate ante ullamcorper. Sed eros ante, lacinia et sollicitudin et, aliquam sit amet augue. In hac habitasse platea dictumst.

1.1.2 Subsection 2

Morbi rutrum odio eget arcu adipiscing sodales. Aenean et purus a est pulvinar pellentesque. Cras in elit neque, quis varius elit. Phasellus fringilla, nibh eu tempus

venenatis, dolor elit posuere quam, quis adipiscing urna leo nec orci. Sed nec nulla auctor odio aliquet consequat. Ut nec nulla in ante ullamcorper aliquam at sed dolor. Phasellus fermentum magna in augue gravida cursus. Cras sed pretium lorem. Pellentesque eget ornare odio. Proin accumsan, massa viverra cursus pharetra, ipsum nisi lobortis velit, a malesuada dolor lorem eu neque.

1.2 Main Section 2

Sed ullamcorper quam eu nisl interdum at interdum enim egestas. Aliquam placerat justo sed lectus lobortis ut porta nisl porttitor. Vestibulum mi dolor, lacinia molestie gravida at, tempus vitae ligula. Donec eget quam sapien, in viverra eros. Donec pellentesque justo a massa fringilla non vestibulum metus vestibulum. Vestibulum in orci quis felis tempor lacinia. Vivamus ornare ultrices facilisis. Ut hendrerit volutpat vulputate. Morbi condimentum venenatis augue, id porta ipsum vulputate in. Curabitur luctus tempus justo. Vestibulum risus lectus, adipiscing nec condimentum quis, condimentum nec nisl. Aliquam dictum sagittis velit sed iaculis. Morbi tristique augue sit amet nulla pulvinar id facilisis ligula mollis. Nam elit libero, tincidunt ut aliquam at, molestie in quam. Aenean rhoncus vehicula hendrerit.

Chapter 2

Current research on Computational Aeroacoustics

2.1 Classification of CAA methods

Computational aeroacoustics is a branch of aeroacoustics that aims to analyze the generation of noise by turbulent flows through numerical methods. A following classification of available methods is currently in use.

1. Hybrid Approach.
 - (a) Integral Method
 - i. Lighthill's Analogy
 - ii. Kirchoff Integral
 - iii. FW-H
 - (b) Linearized Euler Equations
 - (c) Pseudo Spectral
 - (d) EIF
 - (e) APE
2. Direct approach.

The direct approach is the core of this thesis and will be described in detail in chapter 3. A brief introduction to Lightill's analogy with Curle's modification is provided below. Ffowcs Williams Hawkings analogy as an extension to the theory is also provided.

2.2 Lighthill-Curle theory of aerodynamic sound

A mathematically formulated linkage between description of fluid flow and sound generation phenomena was proposed and solved by M. J. Lighthill. His work [10] focused on sound generation as a byproduct of airflow as distinct from sound generated by vibration of solids.

Consider a system with fluctuating flow occupying a very large volume of fluid, at which the non fluctuating part is at rest. Three mechanism of introducing kinetic energy to the system and transforming it to "acoustic energy" are following:

- I By forcing a mass of the fluid in a fixed region to fluctuate, as in the loudspeaker diaphragm
- II By forcing the momentum in fixed space to fluctuate or by forcing the rates of flux through a given control surface to vary, as in vibrating part of a machine (or after striking a tuning-fork)
- III By forcing the rates of flux through a given control surface to vary, without the vibrating motion of solid boundaries, as in noise generated turbulence in flow.

Efficiency of transformation the kinetic energy do sound decreases down the list. First two phenomena are well established in current knowledge and were described in many sources. The research on sound generated aerodynamically starts (probably) with aforementioned work [11].

Lighthill proposes, that Reynolds momentum equation (derived in chapter 3) already expresses that the momentum changes at exactly the same rate as if the medium was at rest under the combined action of real stresses and fluctuating Reynolds stresses. Uniform acoustic medium at rest experiences stresses only from variation of density proportional to the speed of sound squared. A Lighthill stress tensor is therefore introduced to describe the fluctuations of the fluid medium subject to acoustic stresses:

$$T_{ij} = \rho v_i v_j + P_{ij} - a_0^2 \rho \delta_{ij} \quad (2.1)$$

Term P_{ij} is the compression tensor defined as:

$$P_{ij} = (p - p_0) \delta_{ij} - \sigma_{ij} \quad (2.2)$$

where σ_{ij} is the stress tensor due to molecular viscosity defined by:

$$\sigma_{ij} \equiv \left[\mu \left(\frac{\partial \bar{u}_i}{\partial x_j} + \frac{\partial \bar{u}_j}{\partial x_i} \right) \right] - \frac{2}{3} \mu \frac{\partial \bar{u}_l}{\partial x_l} \delta_{ij} \quad (2.3)$$

Propagation of sound in fluid medium without external forces is presented by following governing equations:

$$\frac{\partial \rho}{\partial t} + \frac{\partial}{\partial x_i} (\rho v_i) = 0 \quad (2.4)$$

$$\frac{\partial}{\partial t} (\rho v_i) + a_0^2 \frac{\partial \rho}{\partial x_i} = 0 \quad (2.5)$$

$$\frac{\partial^2 \rho}{\partial t^2} - a_0^2 \nabla^2 \rho = 0 \quad (2.6)$$

The equation 2.4 is the continuity equation for a compressible fluid, equation 2.5 is an approximate equation of momentum and equation 2.6 is established by eliminating the ρv_i term from the previous equations.

By implementing the T_{ij} tensor to the equations 2.4 thru 2.6, the following form is obtained:

$$\frac{\partial \rho}{\partial t} + \frac{\partial}{\partial x_i} (\rho v_i) = 0 \quad (2.7)$$

$$\frac{\partial}{\partial t} (\rho v_i) + a_0^2 \frac{\partial \rho}{\partial x_i} = - \frac{\partial T_{ij}}{\partial x_j} \quad (2.8)$$

$$\frac{\partial^2 \rho}{\partial t^2} - a_0^2 \nabla^2 \rho = \frac{\partial^2 T_{ij}}{\partial x_i \partial x_j} \quad (2.9)$$

Therefore a term describing the fluctuations related to acoustic phenomena is now linked to the flow governing equations. It can now be assumed, that resolving fluid flow along with the appropriate stress, strain and deformation terms can be now used to asses the sound phenomena in the flow field.

Should the receiver of the acoustical signal be outside the computational domain, further investigation must be concluded. Consider an unbounded flow field with a fluctuating point source, so that mass $Q(x, t)$ is introduced to the system at point x and time t , with total rate of introduction of $q(t)$. The density field is than given by the equation:

$$\rho - \rho_0 = \frac{1}{4\pi a_0^2} \frac{q' \left(\frac{t-r}{a_0} \right)}{r} \quad (2.10)$$

where r is the distance from source and $q'(t)$ is the time derivative of $q(t)$ and is defined as instantaneous source strength. For distributed source the equation 2.10 takes form:

$$\rho - \rho_0 = \frac{1}{4\pi a_0^2} \int \frac{\partial}{\partial t} Q \left(y, t - \frac{|x-y|}{a_0} \right) \frac{dy}{|x-y|} \quad (2.11)$$

The equation 2.11 is then solved to a form:

$$\rho - \rho_0 = \frac{1}{4\pi a_0^2} \frac{\partial^2}{\partial x_i \partial x_j} \int T_{ij} \left(y, t - \frac{|x-y|}{a_0} \right) \frac{dy}{|x-y|} \quad (2.12)$$

The equation 2.12 considers an unbounded flow field with point or volumetric source of fluctuations considered as quadrupole sources of acoustic fluctuations. This concept was evolved by Curle [7] to include the effect of solid boundaries on their reflection and diffraction. The modification of the original equation 2.12 is:

$$\begin{aligned} \rho - \rho_0 &= \frac{1}{4\pi a_0^2} \frac{\partial^2}{\partial x_i \partial x_j} \int_V T_{ij} \left(y, t - \frac{r}{a_0} \right) \frac{dy}{r} \\ &\quad - \frac{1}{4\pi a_0^2} \frac{\partial}{\partial x_i} \int_S P_i \left(y, t - \frac{r}{a_0} \right) \frac{dS(y)}{r} \end{aligned} \quad (2.13)$$

where:

$$P_i = -l_j P_{ij} \quad (2.14)$$

where: $l_i = (l_1, l_2, l_3) = n$ is the direction cosines of the outward normal from the fluid, and the sound generated in a medium at rest by a distribution of dipoles of strength P_i per unit area and therefore P_i is the force per unit area exerted on the fluid by the solid boundaries in the x_i direction.

2.3 FW-H Analogy

Further development of analogies developed in references [10], [11] and [7] is presented in work [20]. The extension to the theory includes the effect of arbitrary convective motion of fluid. More over, the FW-H analogy switches from Lighthill's unbounded fluid to a bounded volume. Thus it is possible to compute the flow phenomena within the acoustic near field (which in this case would be a CFD domain) and compute the sound propagation outwards to the acoustic far field (outside the CFD domain) using wave propagation equations.

FW-H analogy derives its governing equation from a volume of fluid V enclosed by a surface Σ , divided into regions 1 and 2 with surface of the discontinuity S moving into region 2 with velocity v . By formulating the rate of change of mass within volume V and deriving a generalized continuity and momentum equations, an equation governing the generation and propagation of sound is obtained.

$$\left(\frac{\partial^2}{\partial t^2} - a^2 \frac{\partial^2}{\partial x_i^2} \right) (\overline{\rho - \rho_0}) = \frac{\partial^2 \overline{T_{ij}}}{\partial x_i \partial x_j} - \frac{\partial}{\partial x_i} \left(P_{ij} \delta(f) \frac{\partial f}{\partial x_j} \right) + \frac{\partial}{\partial t} \left(\rho_0 v_i \delta(f) \frac{\partial f}{\partial x_i} \right) \quad (2.15)$$

where: $(\overline{\rho - \rho_0})$ is the generalized density perturbation - the amplitude of sound and $\overline{T_{ij}}$ is equal to T_{ij} (eq. 2.1) outside any surfaces and equal 0 when within them. Equation $f = 0$ defines the division surface surface S , such that $f < 0$ is in the region 1 and $f > 0$ in region 2 (Heavyside function). The $\delta(f)$ is the Dirac delta function.

The equation 2.15 shows that sound can be regarded as generated by three source distributions: in volume - the quadrupole distribution of strength T_{ij} , on surface - the distribution of dipoles of strength density $P_{ij}n_j$ and monopole distributions from the displacement of volume by the moving surface.

Equation 2.15 can be rewritten to a different form:

$$\begin{aligned} \frac{1}{a_0^2} \frac{\partial^2 (p')}{\partial t^2} - \nabla^2 (p') &= \frac{\partial^2}{\partial x_i \partial x_j} \{ T_{ij} H(f) \} \\ &- \frac{\partial}{\partial x_i} \{ [P_{ij} n_j + \rho u_i (u_n - v_n)] \delta(f) \} \\ &+ \frac{\partial}{\partial t} \{ [\rho_0 v_n + \rho (u_n - v_n)] \delta(f) \} \end{aligned} \quad (2.16)$$

where:

$p' = p - p_0$ — sound pressure fluctuation

u_i — fluid velocity in the x_i direction

u_n — fluid velocity component normal to the surface $f = 0$

v_i — surface velocity in the x_i direction

v_n — surface velocity component normal to the surface

$H(f)$ — Heaviside function

$\delta(f)$ — Dirac delta function

The rewritten equation 2.16 represents an inhomogeneous wave equation can be integrated under specific assumptions and the solutions consists of surface (mono-pole and dipole sources) and volume integrals (quadrupole sources). Software package used

for further computations omits the effect of volume integral, therefore the result is of following form:

$$p'(x, t) = p'_T(x, t) + p'_L(x, t) \quad (2.17)$$

with further development of the solution:

$$\begin{aligned} 4\pi p'_T(x, t) &= \int_{f=0} \left[\frac{\rho_0 (\dot{U}_n + U_{\dot{n}})}{r (1 - M_r)^2} \right] dS \\ &+ \int_{f=0} \left[\frac{\rho_0 U_n \{ r \dot{M}_r + a_0 (M_r - M^2) \}}{r^2 (1 - M_r)^3} \right] dS \end{aligned} \quad (2.18)$$

$$\begin{aligned} 4\pi p'_L(x, t) &= \frac{1}{a_0} \int_{f=0} \left[\frac{\dot{L}_r}{r (1 - M_r)^2} \right] dS \\ &+ \int_{f=0} \left[\frac{L_r - L_M}{r^2 (1 - M_r)^2} \right] dS \\ &+ \frac{1}{a_0} \int_{f=0} \left[\frac{L_r \{ r \dot{M}_r + a_0 (M_r - M^2) \}}{r^2 (1 - M_r)^3} \right] dS \end{aligned} \quad (2.19)$$

where:

$$U_i = v_i + \frac{\rho}{\rho_0} (u_i - v_i) \quad (2.20)$$

$$L_i = P_{ij} n_j + \rho v_i (u_i - v_i) \quad (2.21)$$

When the integration surface coincides with an impenetrable wall, the two terms equation 2.17, $p'_T(x, t)$ and $p'_L(x, t)$ are often referred to as thickness and loading terms, respectively, in light of their physical meanings. The square brackets in equations 2.18 and 2.19 denote that the kernels of the integrals are computed at the corresponding retarded times, τ , defined as in equation 2.22, given the receiver time, t , and the distance to the receiver, r .

$$\tau = t - \frac{r}{a_0} \quad (2.22)$$

The various subscripted quantities appearing in equations 2.18 and 2.19 are the inner products of a vector and a unit vector implied by the subscript. For instance, $L_r = \vec{L} \cdot \vec{r} = L_i r_i$ and $U_n = \vec{U} \cdot \vec{n} = U_i n_i$, where \vec{r} and \vec{n} denote the unit vectors in the radiation and wall-normal directions, respectively. The Mach number vector M_i in equations 2.18 and 2.19 relates to the motion of the integration surface: $M_i = \frac{v_i}{a_0}$. The L_i quantity is a scalar product $L_i M_i$. The dot over a variable denotes source-time differentiation of that variable [1] [20] [3].

FW-H analogy is therefore the general form of Lighthill's acoustic analogy for aerodynamically generated noise, including volume sources of quadrupole kind, such as turbulence in free stream, and dipole and monopole sources of the moving solid body surface within the flow. Solution of the governing equation 2.15 given in equations 2.17, 2.19 & 2.18 omits the sources as weak.

2.4 Limitations to acoustic analogies

Hybrid methods, including the presented Ffowks Williams – Hawking analogy provide a computationally efficient task for engineering problems such as air frame noise, jet injection to atmosphere noise (that is jet engine noise problem), effect of wake generated by automobile mirror on noise in the vehicle cabin. The solution to the FW-H governing equation presented in equations 2.18 and 2.19 may reach instability when the Mach number in the sound radiation direction M_r approaches 1, that is: when the freestream flow velocity approaches sonic conditions. Using the hybrid approach with acoustic analogies may be challenging and pose risk of obtaining "non-physical" results for case considered in this thesis, that is blade of axial compressor in stationary reference frame.

For phenomena characteristic to axial compressor flow, that is strong shock waves, shock wave with boundary layer interaction, high separation of flow enforced by shock waves, and mostly, high adverse pressure gradient may cause mathematical and numerical instabilities to the solution. Considering the pressure change within the computational domain, or, from the governing equation's standpoint, the volume enclosed by a surface, poses some difficulty to choosing free-stream values of density and pressure.

Further attempts towards gaining insight of the sound generation phenomena shall be performed by attempting to use a direct formulation of such.

Chapter 3

Approach and direct formulation of noise analysis

3.1 Direct formulation of noise analysis

The intention behind this study is to perform a flow field noise analysis in CFD without implementation of acoustical analogies to the CFD code itself. Moreover, very limited information on direct formulation of noise analysis was found during the research, with even fewer research on acoustical near field of transonic axial compressors or axial fans of twin spool jet engines.

The process for the direct formulation noise analysis is following:

1. Obtain raw flow field data of static pressure, velocity magnitude from CFD analysis.
2. Perform averaging over time of pressure and velocity magnitude for each point or cell in the flow field (equation 3.1).
3. Obtain offset from mean static pressure and velocity magnitude for every timestep for every point/cell in the saved flow field (equation 3.2).

$$\bar{p} = \frac{1}{n} \sum_{n=1}^N p_k \quad \text{and} \quad \bar{u} = \frac{1}{n} \sum_{n=1}^N u_k \quad (3.1)$$

$$p_{n \text{ sound}} = p_n - \bar{p} \quad \text{and} \quad u_{n \text{ particle}} = u_n - \bar{u} \quad (3.2)$$

Sound pressure signal and flow velocity offset is obtained for every node or cell centroid throughout the simulation flowtime. This dataset can be now post processed. Dataset obtained in described manner now contains sound pressure of the flow field in

every mesh node or cell centroid throughout the computational time. The dataset is now post processed to obtain quantity information of the acoustic nearfield.

Sound intensity for cells/nodes in fluid volume is calculated using formula 3.3.

$$I_n = p_{n \text{ sound}} \cdot u_{n \text{ particle}} \quad (3.3)$$

RMS sound pressure level and intensity level can be obtained from the respective data with use of the formula 3.4.

$$p_{rms} = \sqrt{\frac{\sum_{n=1}^N p_{n \text{ sound}}^2}{N}} \quad I_{rms} = \sqrt{\frac{\sum_{n=1}^N u_{n \text{ particle}}^2}{N}} \quad (3.4)$$

Sound pressure decibel level (SPLdB) for time specific $p_{k \text{ sound}}$ values and RMS values p_{rms} is computed using formula 3.5 with standard reference pressure $p_{ref} = 20 \mu Pa$, whereas for sound intensity with formula 3.6 and with reference intensity $I_{ref} = 1 pW/m^2$.

$$SPLdB = 20 \cdot \log_{10} \left(\frac{|p_{n \text{ sound}}|}{p_{ref}} \right) \quad (3.5)$$

$$SILdB = 10 \cdot \log_{10} \left(\frac{|I_n|}{I_{ref}} \right) \quad (3.6)$$

The signal obtained by direct approach is stored in discrete time samples, therefore using a continuous Fourier Transform would require approximation of the sampled signal to a continuous function, which for large datasets is unjustified. In order to obtain ordinary sinuses of the acoustic signal a Discrete Fourier Transform is performed (eq. 3.7).

$$X_k = \sum_{n=0}^{N-1} x_n \cdot e^{-\frac{j2\pi kn}{N}} \quad (3.7)$$

Let's assume that:

$$b_n = \frac{2\pi kn}{N} \quad (3.8)$$

Therefore, the equation 3.7 can be written as:

$$X_k = x_0 e^{-jb_0} + x_1 e^{-jb_1} + x_2 e^{-jb_2} + \dots + x_N e^{-jb_{N-1}} \quad (3.9)$$

Using Euler's identity the exponent is decomposed (eq. 3.10) to a complex sum:

$$e^{jx} = \cos(x) + j \cdot \sin(x) \quad (3.10)$$

Therefore the equation 3.7 can be written as:

$$X_k = x_0[\cos(-b_0) + j \sin(-b_0)] + \dots + x_n[\cos(-b_{N-1}) + j \sin(-b_{N-1})] \quad (3.11)$$

Rearranging the equation 3.11 and summing up the real and imaginary components will return a complex vector X_k for "k-th" frequency bin.

$$X_k = A_k + jB_k \quad (3.12)$$

The frequency resolution of the DFT depends on the sampling frequency and number of samples, and is calculated by formula 3.13.

$$f_{bin} = \frac{f_s}{N} \quad (3.13)$$

Fourier coefficients are then used to compute the amplitude (eq. 3.14) and phase shift (eq. 3.15) for the "k-th" frequency bin ordinary sinus.

$$\text{Amp}_k = 2 \cdot \sqrt{A_k^2 + B_k^2} \cdot \frac{1}{N} \quad (3.14)$$

$$\theta_k = \arctan \frac{B_k}{A_k} \quad (3.15)$$

3.2 CFD analysis requirements

References [10], [11], [20] and [7] provide a theoretical insight on generating sound in fluid flow due to shear mixing of flows or by implementing a solid boundary in the flow. General remark is: any source of turbulence that result in pressure fluctuation will result in generating sound. Therefore the main requirement for used CFD code for direct noise analysis is the capability of resolving turbulent flow and corresponding fluctuations of the pressure.

Let's consider the effect of injection of energy to the fluid resulting in creation of eddies (Fig. 3.1)

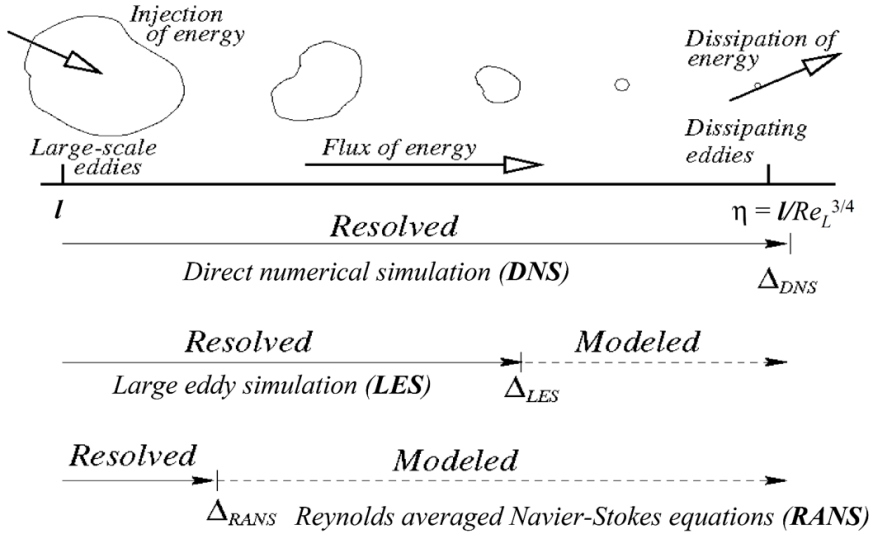


FIGURE 3.1: Resolving eddies in different kinds of CFD analyses

3.2.1 Governing equations

Fluid flow as understood in CFD analyses is described by continuity (3.16) and momentum (3.17) equations.

$$\frac{\partial \rho}{\partial t} + \nabla(\rho U) = 0 \quad (3.16)$$

$$\frac{dU}{dt} = -\frac{1}{\rho} \nabla p + \nu \nabla^2 U \quad (3.17)$$

A number of special treatments to these equations is performed in order to obtain a solved flowfield at the end of the CFD workflow.

3.2.2 Direct Numerical Simulation

Considering the direct formulation of noise, the Direct Numerical Simulation is seemingly the best tool of choice. The DNS formulation of flow solves directly the discrete form of Navier-Stokes Equation without any turbulence models. Size limit of the resolved eddies is the Kolmogorov limit (eq. 3.18). In order to properly resolve the DNS simulation up to this scale, the mesh sizing must be at least as small as the expected Kolmogorov limit at given Reynolds number.

$$\eta \approx \frac{l}{Re^{3/4}} \quad (3.18)$$

Reference [4] provides information on calculating the mesh grid node count for DNS calculations (eq. 3.19) for flat plate airfoil of aspect ratio L_z/L_x . The computational box for this case is of size $L_x \times \delta \times L_z$ in streamwise, normal to plate and spanwise direction respectively, where δ is the boundary layer thickness.

$$N_{DNS} = 0.000153 \frac{L_z}{L_x} Re_{L_x}^{37/14} \left[1 - \left(\frac{Re_{x_0}}{Re_{L_x}} \right)^{23/14} \right] \quad (3.19)$$

Point x_0 is the location where formulas 3.20 and 3.21 are valid for Reynolds number range ($10^6 \leq Re_x \leq 10^9$).

$$\delta = x \cdot 0.16 Re_x^{(-1/7)} \quad (3.20)$$

$$c_f = 0.027 Re_x^{(-1/7)} \quad (3.21)$$

For aspect ratio $L_z/L_x = 4$ and $Re_{x_0} = 5 \cdot 10^5$ the node count for streamwise $Re = 10^6$ is roughly $2.99 \cdot 10^{12}$ nodes and for $Re = 10^7$ is roughly $1.92 \cdot 10^{15}$ nodes.

Such node and cell counts are impossible to solve within practical walltime, therefore usage of DNS for sound analysis is limited to small Reynolds numbers.

3.2.3 Large Eddy Simulation

Large eddy simulation (LES) is a mathematical model for turbulence used in computational fluid dynamics. It was initially proposed in 1963 by Joseph Smagorinsky to simulate atmospheric air currents [14].

The principal idea behind LES is to reduce the computational cost by ignoring the smallest length scales, which are the most computationally expensive to resolve, via low-pass filtering of the Navier–Stokes equations. Such a low-pass filtering, which can be viewed as a time- and spatial-averaging, effectively removes small-scale information from the numerical solution. This information is not irrelevant, however, and its effect on the flow field must be modeled, a task which is an active area of research for problems in which small-scales can play an important role such as acoustics [19].

The governing equations employed for LES are obtained by filtering the time dependent Navier-Stokes equations in either Fourier (wave-number) space or configuration (physical) space. The filtering process effectively filters out the eddies whose scales are smaller than the filter width or grid spacing used in the computations. The resulting equations therefore govern the dynamics of large eddies [1].

A filtered variable is defined by:

$$\bar{\phi}(x) = \int_D \phi(x') G(x, x') dx' \quad (3.22)$$

where D is the fluid domain, and G is the filter function that determines the scale of the resolved eddies. The finite volume discretization itself implicitly provides the filtering operation:

$$\bar{\phi}(x) = \frac{1}{V} \int_{\nu} \phi(x') dx', \quad x' \in \nu \quad (3.23)$$

where V is the volume of a computational cell. The filter function, $G(x, x')$ implied here is then:

$$G(x, x') = \begin{cases} \frac{1}{V}, & \text{if } x' \in \nu \\ 0, & \text{otherwise} \end{cases} \quad (3.24)$$

For compressible flows, it is convenient to introduce the density-weighted (or Favre) filtering operator:

$$\tilde{\phi} = \frac{\overline{\rho\phi}}{\overline{\phi}} \quad (3.25)$$

Filtering the continuity 3.16 and momentum 3.17 equations following form is obtained:

$$\frac{\partial \rho}{\partial t} + \frac{\partial}{\partial x_i} (\rho \bar{u}_i) = 0 \quad (3.26)$$

$$\frac{\partial}{\partial t} \rho \bar{u}_i + \frac{\partial}{\partial x_j} (\rho \bar{u}_i \bar{u}_j) = \frac{\partial}{\partial x_j} (\sigma_{ij}) - \frac{\partial \bar{p}}{\partial x_i} - \frac{\partial \tau_{ij}}{\partial x_j} \quad (3.27)$$

where σ_{ij} is the stress tensor due to molecular viscosity defined by:

$$\sigma_{ij} \equiv \left[\mu \left(\frac{\partial \bar{u}_i}{\partial x_j} + \frac{\partial \bar{u}_j}{\partial x_i} \right) \right] - \frac{2}{3} \mu \frac{\partial \bar{u}_l}{\partial x_l} \delta_{ij} \quad (3.28)$$

and τ_{ij} is the subgrid-scale stress defined by:

$$\tau_{ij} \equiv \rho \bar{u}_i \bar{u}_j - \rho \bar{u}_i \bar{u}_j \quad (3.29)$$

The Favre Filtered Navier-Stokes equation takes the same form as equation 3.27. The compressible form of the subgrid stress tensor is defined as:

$$\tau_{ij} = \bar{\rho} u_i \tilde{u}_j - \bar{\rho} \tilde{u}_i \tilde{u}_j \quad (3.30)$$

The subgrid-scale stresses resulting from the filtering operation are unknown, and require modeling. The subgrid-scale turbulence models employ the Boussinesq hypothesis [9] in the RANS models, computing subgrid-scale turbulent stresses from:

$$\tau_{ij} - \frac{1}{3} \tau_{kk} \delta_{ij} = -2\mu_t \overline{S}_{ij} \quad (3.31)$$

where μ_t is the subgrid-scale turbulent viscosity. The isotropic part of the subgrid-scale stresses τ_{kk} is not modeled, but added to the filtered static pressure term. S_{ij} is the rate-of-strain tensor for the resolved scale defined by:

$$\overline{S}_{ij} \equiv \frac{1}{2} \left(\frac{\partial \bar{u}_i}{\partial x_j} + \frac{\partial \bar{u}_j}{\partial x_i} \right) \quad (3.32)$$

Equation 3.30 is split into its isotropic and deviatoric parts:

$$\tau_{ij} - \frac{1}{3} \tau_{kk} \delta_{ij} = -2\mu_t \left(S_{ij} - \frac{1}{3} S_{kk} \delta_{ij} \right) \quad (3.33)$$

Using LES approach is viable for resolving directly formulated noise, yet the computational cost of such calculations is still relatively large due to mesh sizing requirements. As stated by [4] the required node count for the analysis can be described by formulas 3.34 and 3.35 for modeled and resolved boundary layers.

$$N_{wm} = 54.7 \frac{L_z}{L_x} n_x n_y n_z Re_{L_x}^{2/7} \left[\left(\frac{Re_{L_x}}{Re_{x_0}} \right)^{(5/7)} - 1 \right] \quad (3.34)$$

$$N_{wr} = 0.021 \frac{n_y}{\Delta x_w^+ \Delta z_w^+} \frac{L_z}{L_x} Re_{L_x}^{13/7} \left[1 - \left(\frac{Re_{L_x}}{Re_{x_0}} \right)^{(6/7)} \right] \quad (3.35)$$

The computational box for this case is of size $L_x \times \delta \times L_z$ in streamwise, normal to plate and spanwise direction respectively, where δ is the boundary layer thickness.

For $L_z/L_x = 4$ and $Re_{x_0} = 5 \cdot 10^5$ the node count for streamwise $Re = 10^6$ and $Re = 10^7$ is computed. The $n_x n_y n_z$ product is the number of grid points to resolve the cubic computational volume δ^3 exterior to the viscous wall region. Suggested value of $n_x n_y n_z = 2500$, where $n_x = 10$ $n_y = 25$ $n_z = 10$ was used for the computation of node count with equation 3.34. Suggested $\Delta x_w^+ \approx 100$, $\Delta z_w^+ \approx 20$ and $n_y \approx 10$ was used for computation of node count with equation 3.35.

Node count for $Re = 10^6$ is roughly $1.82 \cdot 10^7$ nodes for modelled and $2.61 \cdot 10^7$ nodes for resolved wall flow. For $Re = 10^7$ the figures are $4.10 \cdot 10^8$ and $3.88 \cdot 10^9$ nodes respectively [4].

It must be noted that provided cell count is solely for a flow box of boundary layer width. Respective mesh sizing should be propagated towards volume of the computational domain thus enlarging the mesh even further.

LES analyses are commonly used in research and engineering and the method used is feasible for the direct noise formulation. However the computational expense of running such cases is high, but manageable. Second limiting factor for LES is the amount of data generated during the process. As the direct approach requires storing at least every second time step for further processing, terabytes of data are predicted.

3.2.4 Reynolds Averaged Navier Stokes

The most computationally efficient method for resolving turbulent flows is using Reynolds Averaged Navier Stokes equation. Consider a conservation variable ϕ of fluid described by spatial and temporal variables. The quantity may be decomposed to a sum of time averaged value in given spatial coordinates and time dependent fluctuations (eq. 3.36).

$$\phi(x, y, z, t) = \overline{\phi(x, y, z, t)} + \phi'(x, y, z, t) \quad (3.36)$$

Consider at first the continuity equation 3.16. By applying Reynolds decomposition to velocity vector we obtain:

$$\frac{\partial \rho}{\partial t} + \frac{\partial \overline{\rho u_i}}{\partial x_i} + \frac{\partial \rho u'_i}{\partial x_i} = 0 \quad (3.37)$$

By averaging the both sides of the equation 3.37 and applying averaging rules to its components we obtain:

$$\frac{\partial \rho}{\partial t} + \frac{\partial \overline{\rho u_i}}{\partial x_i} + \frac{\partial \overline{\rho u'_i}}{\partial x_i} = 0 \quad (3.38)$$

Because the average of an average is equal average, and the average of the fluctuation component is equal 0 we obtain equation 3.39, the Reynolds averaged continuity equation.

$$\frac{\partial \rho}{\partial t} + \frac{\partial \overline{\rho u_i}}{\partial x_i} = 0 \quad (3.39)$$

By taking the momentum equation 3.17, switching to the index notation and applying the Reynolds decomposition we obtain the equation 3.40

$$\underbrace{\frac{\partial(\bar{u}_i + u'_i)}{\partial t}}_1 + \underbrace{(\bar{u}_j + u'_j) \frac{\partial(\bar{u}_j + u'_j)}{\partial x_j}}_2 = -\underbrace{\frac{1}{\rho} \frac{\partial(\bar{p} + p')}{\partial x_i}}_3 + \nu \underbrace{\frac{\partial^2(\bar{u}_i + u'_i)}{\partial x_j^2}}_4 \quad (3.40)$$

Components 1, 3 and 4 of the above equation are treated in the same manner as the continuity equation and thus we obtain:

$$\underbrace{\frac{\partial \bar{u}_i}{\partial t}}_1 \quad \underbrace{\frac{1}{\rho} \frac{\partial \bar{p}}{\partial x_i}}_3 \quad \underbrace{\nu \frac{\partial^2 \bar{u}_i}{\partial x_j^2}}_4 \quad (3.41)$$

The decomposition of component 2 from the equation 3.40 requires multiplication of the components within the braces and performing Reynolds averaging on each of the products:

$$\underbrace{\left((\bar{u}_j + u'_j) + \frac{\partial(\bar{u}_i + u'_i)}{\partial x_j} \right)}_2 = \underbrace{\overline{(\bar{u}_j \frac{\partial \bar{u}_i}{\partial x_j})}}_{M \cdot M \neq 0} + \underbrace{\overline{(\bar{u}_j \frac{\partial u'_i}{\partial x_j})}}_{M \cdot F = 0} + \underbrace{\overline{(u'_j \frac{\partial \bar{u}_i}{\partial x_j})}}_{F \cdot M = 0} + \underbrace{\overline{(u'_j \frac{\partial u'_i}{\partial x_j})}}_{F \cdot F \neq 0} \quad (3.42)$$

The $F \cdot F \neq 0$ product can be further simplified by equation:

$$\frac{\partial u'_j u'_i}{\partial x_j} = \underbrace{u'_j \frac{\partial u'_j}{\partial x_j}}_{= 0} + \underbrace{u'_j \frac{\partial u'_i}{\partial x_j}}_{F \cdot F \neq 0} \quad (3.43)$$

By inserting the components 1 through 4 from equations 3.41 and 3.42 modified by equation 3.43 to the equation 3.40 we obtain the Reynolds averaged momentum equation:

$$\frac{d\bar{U}}{dt} = -\frac{1}{\rho} \frac{\partial \bar{p}}{\partial x_i} + \frac{\partial}{\partial x_j} \left[\nu \frac{\partial \bar{u}_j}{\partial x_j} - \overline{u'_i u'_j} \right] \quad (3.44)$$

By representing the viscous terms as a stress tensor (eq. 3.45) we obtain the momentum equation with turbulent stress (eq 3.46)

$$\nu \frac{\partial^2 \bar{u}_i}{\partial x_j^2} = \frac{1}{\rho} \frac{\partial}{\partial x_j} \tau_{ij} \quad (3.45)$$

$$\frac{d\bar{U}}{dt} = -\frac{1}{\rho} \nabla \bar{p} + \frac{1}{\rho} \frac{\partial}{\partial x_j} \left[\tau_{ij} - \rho \overline{u'_i u'_j} \right] \quad (3.46)$$

The $\rho \overline{u_i u_j}$ term can be further transformed to Reynolds stress tensor linked to shear stress. The remaining fluctuating component is then modeled rather than resolved, by one of many turbulence model based on Boussinesque theory.

3.2.5 Hybrid RANS/LES Methods

At first, the concepts of Reynolds Averaging and Spatial Filtering seem incompatible, as they result in different additional terms in the momentum equations (Reynolds Stresses and sub-grid stresses). This would preclude hybrid models like Scale-Adaptive Simulation (SAS), Detached Eddy Simulation (DES), Shielded DES (SDES), or Stress-Blended Eddy Simulation (SBES), which are based on one set of momentum equations throughout the RANS and LES portions of the domain. However, it is important to note that once a turbulence model is introduced into the momentum equations, they no longer carry any information concerning their derivation (averaging). Case in point is that the most popular models, both in RANS and LES, are eddy viscosity models that are used to substitute either the Reynolds- or the sub-grid stress tensor. After the introduction of an eddy viscosity (turbulent viscosity), both the RANS and LES momentum equations are formally identical. The difference lies exclusively in the size of the eddy-viscosity provided by the underlying turbulence model. This allows the formulation of turbulence models that can switch from RANS to LES mode, by lowering the eddy viscosity in the LES zone appropriately, without any formal change to the momentum equations [1].

For further calculations, Delayed Detached Eddy Simulation with $SSTk - \omega$ model was chosen. In the DES approach, the unsteady RANS models are employed in the boundary layer, while the LES treatment is applied to the separated regions. The LES region is normally associated with the core turbulent region where large unsteady turbulence scales play a dominant role. In this region, the DES models recover LES-like subgrid models. In the near-wall region, the respective RANS models are recovered [1].

Formulation of DES is the development of the Spalart-Allmaras turbulence model for RANS formulation [16], therefore the theoretical formulations are derived from the S-A model.

The S-A model uses modified turbulent viscosity $\tilde{\nu}$ in place of the turbulent kinematic viscosity.

$$\frac{\partial}{\partial t} (\rho \tilde{\nu}) + \frac{\partial}{\partial x_i} (\rho \tilde{\nu} u_i) = G_\nu + \frac{1}{\sigma_{\tilde{\nu}}} \left[\frac{\partial}{\partial t} \left\{ (\mu + \rho \tilde{\nu}) \frac{\partial \tilde{\nu}}{\partial x_j} \right\} + C_{b2} \rho \left(\frac{\partial \tilde{\nu}}{\partial x_j} \right)^2 \right] - Y_\nu + S_{\tilde{\nu}} \quad (3.47)$$

Turbulence production G_ν and destruction Y_ν terms are modeled as:

$$G_\nu = C_{b1} \rho \tilde{S} \tilde{\nu} \quad (3.48)$$

$$Y_\nu = C_{wq} \rho f_w \left(\frac{\tilde{\nu}}{d} \right)^2 \quad (3.49)$$

Where d is the length scale calculated as the distance to the closest wall and \tilde{S} being the measure of deformation tensor:

$$\tilde{S} \equiv S + \frac{\tilde{\nu}}{\kappa^2 d^2} f_{v2} \quad (3.50)$$

where:

$$S \equiv |\Omega_{ij}| + C_{prod} \min(0, |S_{ij}| - |\Omega_{ij}|) \quad (3.51)$$

where:

$$C_{prod} = 2.0, \quad |\Omega_{ij}| \equiv \sqrt{2\Omega_{ij}\Omega_{ij}}, \quad |S_{ij}| \equiv \sqrt{2S_{ij}S_{ij}} \quad (3.52)$$

with the mean strain rate defined as:

$$S_{ij} = \frac{1}{2} \left(\frac{\partial u_j}{\partial x_i} + \frac{\partial u_i}{\partial x_j} \right) \quad (3.53)$$

The equation 3.49 shows that $\tilde{\nu}$ is proportional to the local deformation rate and wall distance: $\tilde{\nu} \propto Sd^2$. Smagorinsky model for "Sub-Grid-Scale" (SGS) scales the turbulent viscosity with local deformation and grid spacing: $\tilde{\nu} \propto S\Delta^2$.

By replacing the d in the S-A destruction term (eq. 3.49) with \tilde{d} :

$$\tilde{d} \equiv \min(d, C_{DES}\Delta) \quad (3.54)$$

a single model is obtained, acting as RANS with S-A turbulence modeling in regions where $d \ll \Delta$ and with LES behavior where $d \gg \Delta$. Grid spacing Δ is defined as the largest dimension of the computational cell $\Delta \equiv \max(\Delta x, \Delta y, \Delta z)$. In case of an ambiguous grid definition, where $\Delta < \delta$ the DES limiter can activate the LES mode inside the boundary layer, where the grid is not fine enough to sustain resolved turbulence. Therefore, a new formulation [15] of DES is available to preserve the RANS mode throughout the boundary layer. This is known as the delayed option or DDES for delayed DES [1].

DES and DDES methods can be used with other RANS turbulence models. Further analyses presented in this thesis use a $k - \omega SST$ model. For hybrid model the dissipation of turbulent kinetic energy is modified:

$$Y_k = \rho \beta^* k \omega F_{DES} \quad (3.55)$$

where:

$$F_{DES} = \max \left(\frac{L_t}{C_{DES} \Delta_{max}} (1 - F_{SST}), 1 \right) \quad (3.56)$$

where C_{DES} is a calibration constant used in the DES model and has a value of 0.61, with $F_{SST} = 0, F_1, F_2$ where F_1 and F_2 are the blending functions of the Baseline and $SSTk - \omega$ model. The turbulent length scale is the parameter that defines this RANS model:

$$F_{DES} = \max \left(\frac{L_t}{C_{DES} \Delta_{max}}, 1 \right) \quad (3.57)$$

The F_{DDES} blending function is given by equation 3.57 with model constants $C_{d1} = 20$, $C_{d2} = 3$ and r_d as defined by eq. 3.59:

$$F_{DDES} = \tanh \left[(C_{d1} r_d)^{C_{d2}} \right] \quad (3.58)$$

$$r_d = \frac{\nu_t + \nu}{\kappa^2 y^2 \sqrt{0.5 (S^2 + \Omega^2)}} \quad (3.59)$$

3.3 Mesh sizing requirements

Let's assume a sinusoidal pressure fluctuation $y(t)$ (equation 3.60) of ordinary frequency of f and amplitude A moving through ambient medium, for more than 5 cycles at speed of sound 3.61. The mathematical and numerical methods for solving flow field described in section above are capable of computing such pressure fluctuation in a fine resolution mesh.

$$y(t) = A \sin(2\pi f t + \phi) \quad (3.60)$$

$$a = \sqrt{\kappa R T} \quad (3.61)$$

Both cell size and time step size are limited by the wave length, and therefore frequency of the discussed pressure fluctuation. The wavelength is calculated by formula 3.62.

$$\lambda = \frac{v}{f} \quad (3.62)$$

Considered fluctuation travels through the finite volumes in the stationary CFD mesh. Pressure value is measured at the cell center for each timestep. At this stage, it is assumed that timestep is "good enough" for the analysis. Four possibilities are to be discussed

Scenario 1: wavelength is smaller than the edge length of the cell in the direction of propagation. In this condition, the pressure fluctuation performs a number of cycles within one cell (Fig. 3.2). Due to the numerical approach, such fluctuation will not be computed and recorded by data acquisition at the cell centroid or at node coordinates.



FIGURE 3.2: Scenario 1. Wavelength smaller than cell edge length

Scenario 2: wavelength and cell edge length in the direction of propagation are equal. In this condition, the pressure fluctuation performs one cycle within one cell in the direction of the fluctuation propagation (Fig. 3.3). Such pressure change will be also filtered out by the numerical scheme.



FIGURE 3.3: Scenario 2. Wavelength equal to cell edge length

Scenario 3: wavelength is equal to 4 minimum cell lengths in the direction of propagation. This is the minimum cell size condition for discussed approach. In this condition,

the pressure fluctuation performs one cycle within four cells in the direction of the fluctuation propagation (Fig. 3.4). FVM method is now capable of computing the pressure resulting from sound wave propagation.



FIGURE 3.4: Scenario 3. Wavelength equal four minimum edge lengths

Scenario 4: wavelength is larger than 4 minimum cell edge lengths. In this condition, the pressure fluctuation performs one cycle within multiple cells in the direction of the fluctuation propagation (Fig. 3.5). FVM method computes pressure from the sound wave propagation across multiple cells.



FIGURE 3.5: Scenario 4. Wavelength larger than four minimum edge lengths

Based on these possibilities, the edge sizing of the finite volume cell should be at least four times smaller than the shortest wavelength expected in the flow field.

As there is no information on the pressure fluctuations in the flow field, the range of the further analyses will be limited to audible range of 20Hz to 20 000Hz. The wavelengths are calculated by formula 3.62 and divided by four to obtain the required cell sizing. The velocity of sound obtained by equation 3.61 with reference temperature $T = 300K$. The results for outermost sound frequencies of the audible range are presented in table 3.1

TABLE 3.1: Test case boundary conditions

Frequency [Hz]	Wave length [m]	Cell size [m]
20	17.390	4.347
20 000	0.01739	0.004347

3.4 Timestep requirements

There are two limiting factors for timestep requirements. The high frequency signal is limited by the timestep size, whereas the low frequencies are limited to the total number of timesteps and physical flow time calculated. The timestep size is calculated first.

Once sizing of the mesh is established, time at which the fluctuation passes the cell is established by simple formula 3.63. Distance s is the cell edge sizing, obtained as in section 3.3 and the relation between cell size and wave length is presented in equation 3.65.

$$a = \frac{s}{t} \quad (3.63)$$

Where

$$t = \frac{1}{f} \quad (3.64)$$

$$s = \frac{\lambda}{4} \quad (3.65)$$

By rearranging the equation 3.63 to solve for t and substituting λ by 3.62 we obtain:

$$t = \frac{s}{a} = \frac{\lambda}{4a} = \frac{a}{f} \cdot \frac{1}{4a} = \frac{1}{4f} \quad (3.66)$$

Time step t becomes also a sampling frequency for the pressure signal therefore it must be compared with the requirements stated by Shannon-Nyquist-Whitaker theorem: *If a function $x(t)$ contains no frequencies higher than B hertz, it is completely determined by giving its ordinates at a series of points spaced $1/(2B)$ seconds apart.* Presented time stepping approach fulfills that theorem.

Equation 3.66 shows that time step for the analysis is dependent from the expected value of high frequency fluctuations.

In order to capture frequencies on the low end of the spectrum, the analysis must be performed long enough to capture at least a single, with optimum 5 or more periods, of the desired low frequency. Assuming lower end of the audible frequency spectrum, the 20Hz frequency, the simulation time must resemble at least 0.05s of flow time with optimum 0.25s of flow time at given timestep.

3.5 Limiting factors of the direct approach

Described direct formulation noise analysis is solely a post processing approach relying on data generated on CFD analysis. In order to obtain reasonable results down the process, the analysis itself must be capable of delivering pressure fluctuations that can be considered as acoustic in source.

It is advised to use a turbulence model that is capable of resolving small scale turbulence on a mesh that will allow such resolution. Utilizing LES formulation or at least hybrid RANS/LES turbulence model such as DDES. Using an averaging formulation such as RANS will cut off all of the fluctuations and is not suitable for this approach.

The range of frequencies captured by this method depends on the mesh sizing and timestep sizing. Therefore, if the range of expected frequencies is known or at least estimated, the mesh sizing and timestep size can be adjusted for the given case. For analysis within audible range, 4000 timesteps are required for one 20Hz period. Considering the mesh sizing requirements, the mesh cell count will rise up to tens of millions for a single passage axial compressor blade. This makes the case files and storing data for each timestep relatively challenging and requires securing adequate storage beforehand.

A major limiting factor is the implementation of the direct noise formulation post-processing. For this thesis, the method was implemented in python v.3.5 high level programming language. Python code is written in C/C++ and provides a vast array of additional libraries for handling files, tabular data and performing mathematical operations. The code is presented in appendices to this dissertation. Although easy to implement, python code is known to be inefficient and slow while managing large amounts of data. Tools and algorithms used in implementing the averaging, obtaining sound pressure and particle velocity as well as DFT are built in tools from specific libraries. As convenient for the implementation, the post-processing code requires some amount of operational memory and disk space for generating the results.

The programming language used for the post-processing of data must be capable of generating 2D and 3D plots for visualization purposes. Ideally the processed and visualized data should resemble the mesh from which the initial data was gathered.

Chapter 4

Test case

4.1 NASA Rotor 67 transonic axial compressor

The test specimen for given analysis is a NASA Rotor 67 (R67) transonic axial compressor. Originating as a first stage of two stage fan for evaluation of design procedures, validation of experimental facilities as well as meshing and CFD tools. Both stages were used in a multitude of studies for aerodynamics, geometry optimisation, noise analyses and structural analyses. Full design procedure can be found in references [6] and [18]. The CFD analysis and further post processing of the pressure signals shall be performed on a single passage of a first stage rotor of the compressor. The setup for the calculations (apart from the single passage constraint) is relevant do case described in [17], which was the main source for geometry and flowfield data.

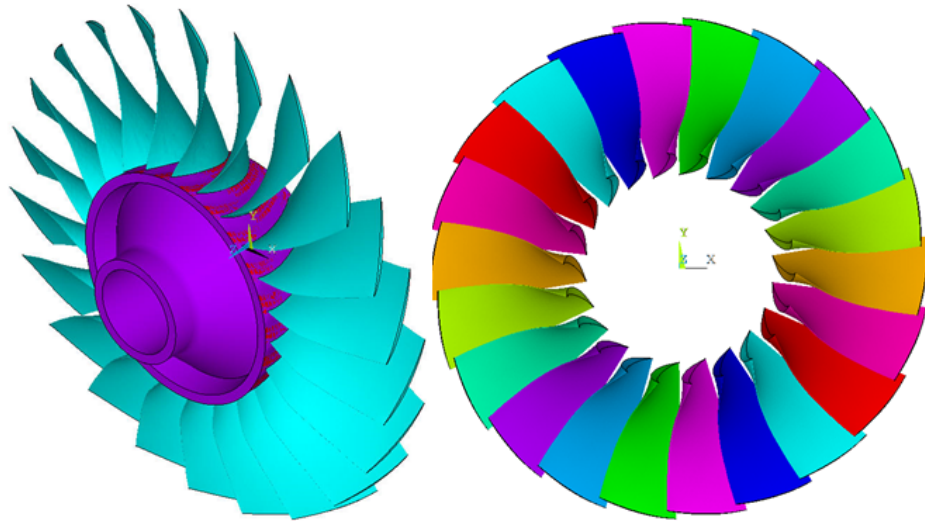


FIGURE 4.1: Geometry of NASA R67

Basic figures of the given rotor are, design pressure ratio of 1.63 at massflow of 33.25 kg/sec. The design rotational speed is 16 043 rpm, which yields a tip speed of 429 m/s and an inlet tip relative Mach number of 1.38. The rotor has 22 blades and an aspect ratio of 1.56 (based on average span/root axial chord). The inlet and exit tip diameters are 514 and 485 mm, respectively, and the inlet and exit hub/tip radius ratios are 0.375 and 0.478, respectively. A fillet radius of 1.78 mm is used at the airfoil-hub juncture. The square root of the mean square of the airfoil surface finish is 0.8 μm or better, the airfoil surface tolerance is ± 0.04 mm, and the running tip clearance is approximately 1.0 mm [17]. Surface roughness and some of the geometrical features are omitted during the preparation of the geometry and CFD mesh for reasons described in sections 4.2 and 4.3. General geometry of NASA R67 is presented on fig 4.1. Basic parameters of the test subject are presented in table 4.1

TABLE 4.1: Basic R67 parameters

Parameter	Value	Unit
Π	1.67	-
\dot{m}	33.25	kg/s
ω	16043	rpm
v_t	426	m/s
Mat	1.26	-
blade count	22	-

4.2 3D geometry preparation

Geometry was prepared in Ansys ICEM 14.5 meshing software. Creating the geometry directly in the meshing software reduces the risk of creating flaws in the geometry, due to file translations. Mesh is created in millimeters.

The R67 blade coordinates for rotor and stator on both stages is given in references [6] and [18] and provide the blade elements in a Multiple-Circular-Arc fashion. In such approach the design blade elements lie on conical surfaces which approximate the actual stream flow surfaces. A blade-element-layout method is developed which preserves the constant-angle change characteristic of the circular-arc profile. More specifically, the mean camber line and the suction and pressure surface lines of a blade element are lines with a constant rate of angle change with path distance on a specified conical surface [5]. Although relatively comfortable for design purposes, such approach requires implementing a macro or script to desired CAD tool for creating the blade elements or transforming the MCA blade to Cartesian or cylindrical coordinates. Reference [5] provides an extended definition of MCA blade description as well as Fortran code for generating blade cross-section and geometric properties of the blade. Source [17] provides a list of

coordinates for 14 profiles of the 1st stage rotor blade suction and pressure side, as well as coordinates for hub and casing in the meridional plane. These coordinates were used to create the geometry of the single passage of the subject blade. Coordinates are also available in Appendix H and project Github repository [12].

The coordinate system is a standard right-hand Cartesian CS. Rotation axis is set to Z-axis with flow in positive Z direction. The compressor rotation is set as in right-hand rule, the compressor rotates in clockwise direction when facing the blade leading edge. $Z = 0$ coordinate is defined by point number 1 on 1st blade design surface (see Appendix H for details).

Hub and casing flow path were created by importing formatted point data as a b-spline curve, followed by extrusion the curve to surface by rotating it by $\pm 60^\circ$. Blade surfaces cylindrical coordinates were transformed to Cartesian coordinates using simple trigonometric calculations and imported as set of splines. Suction and pressure surface of the blade were created by lofting the surface along the imported splines. Leading and trailing edge radii were created in a similar manner with use of edge radius and edge tangency points given in [17]. Tip gap of the blade was created by offsetting the casing surface by 1.016 mm in the normal direction towards the rotation axis and creating a section line between blade surfaces and the offset surface.

Due to the estimated mesh cell count, only one blade passage is created, therefore a set of periodic surfaces must be defined. ICEM software is capable of creating a midline as an average of coordinates of two given lines. A midline was created for every design profile and was manually extended beyond the blade leading and trailing edge. Midlines were lofted to create a midsurface which was later on copied with rotation by $\pm 0.5 \cdot \frac{360^\circ}{22}$ to create two identical periodic surfaces.

Aforementioned midlines were also rotated along Z-axis to create control surfaces for mesh stabilization and data acquisition down the process.

Reference [17] provides coordinates of hub and casing for the full experiment, however only a rotating part of the experimental rotor setup will be used. Two surfaces normal to Z direction at coordinates $Z = -13.74$ mm and $Z = 93.65$ mm are placed as inlet and outlet boundary conditions. Geometry was finished by necessary extrusions, trimming and other finishing operations to ensure high quality surface for meshing. Usually, the geometry must be watertight to ensure proper meshing process, however ICEM as patch-independent meshing software does not require that.

Physical experiment test compressor has a 1.78 mm fillet at airfoil-hub juncture. This feature was omitted as it would unnecessarily complicate the meshing process and increase the cell count.

Such approach allowed for creating a geometry for single blade passage with centered blade of 1st stage rotor of the test compressor (Fig 4.2).

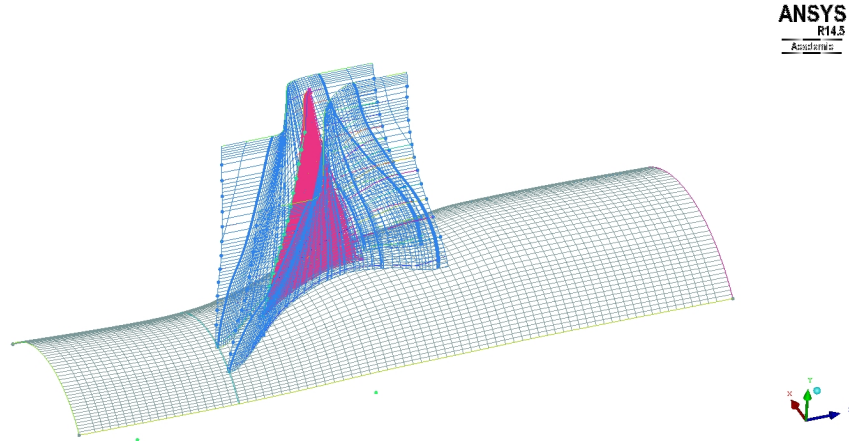


FIGURE 4.2: Final single passage geometry. Some features hidden for clarity

4.3 Meshing approach

Following requisites are posed to the mesh for the discussed case:

- Possibly low number of elements fulfilling the mesh sizing requirements stated in chapter 3.1,
- Mesh should be a fully structural mesh including the tip gap,
- The periodic boundary mesh must be identical/conforming for both boundaries,
- The mesh must have high quality metrics in terms of cell orthogonality and skew as defined by equations 4.1 & 4.2 respectively.

$$\text{Orthogonality} = \frac{\vec{A}_i \cdot \vec{f}_i}{|\vec{A}_i| \cdot |\vec{f}_i|} \quad (4.1)$$

$$\text{Skewness} = \frac{\text{Optimal Cell Size} - \text{Cell Size}}{\text{Optimal Cell Size}} \quad (4.2)$$

One of the initial mesh concepts was an unstructured mesh with triangular surface mesh extruded to prism boundary layer and mostly isotropic tetrahedra in the volume. This approach was quickly rejected for bad quality elements near the airfoil/hub junction and tip gap, as well as element count in range of 4.5 million cells for sizing relevant for RANS analysis. This approach was quickly dropped.

A non-trivial topology with fully conforming periodic boundaries was introduced (fig 4.3). This topology fulfills all the prerequisites stated apart from possibility to mesh a structural tip gap. Such approach makes it impossible from topological standpoint to place a structural mesh in this area. A RANS sufficient mesh without tip gap area (blade was extended to the casing surface) was created. The cell count for this mesh is below 0.5 million cells with better skewness and orthogonal quality. This mesh was utilized for numerical setup and data acquisition testing as it was faster to converge.

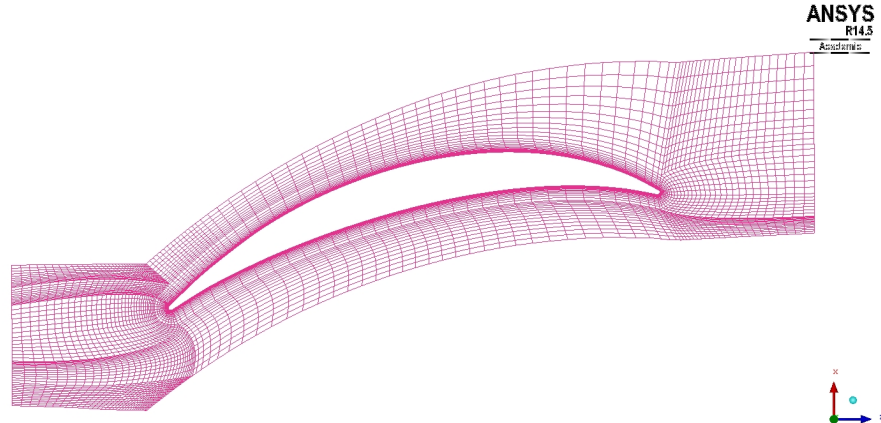


FIGURE 4.3: Mesh topology with conforming periodic boundaries

Final topology was a standard h-grid topology for airfoil 4.4. Although it is impossible to create a conforming periodic interface with such mesh topology, a fully structural tip gap was implemented. Omitting the blade-hub juncture fillet simplified the mesh. Such topology eradicates the necessity of placing 5-way topology points.

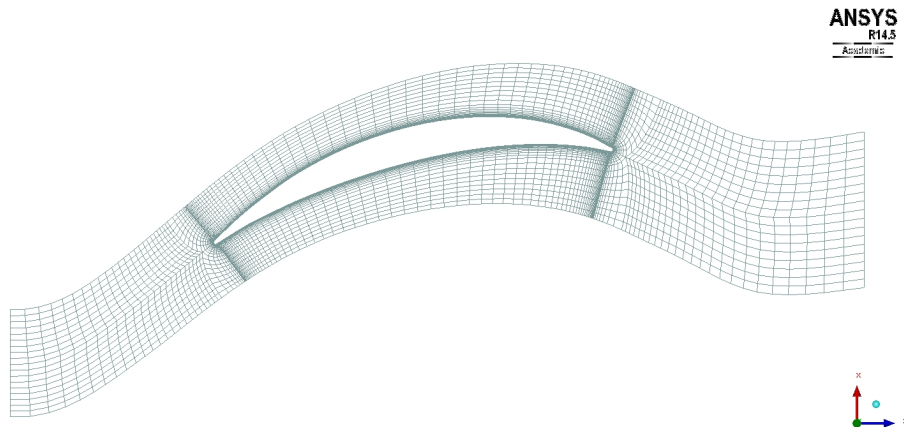


FIGURE 4.4: Mesh h-topology

Mesh was created in Ansys ICEM software using structural blocking method. The topology was sliced and associated to internal surfaces mentioned in the above section. This enforces mesh layering along design streamlines and provides high quality mesh

on internal surfaces for flow field data acquisition further in the process. Blade wall boundary condition is distributed among five separate parts: blade pressure side, blade suction side, leading and trailing edges and tip surface.

Element sizing in volume and in tangent direction to the blade is limited to 3 mm, with 5 mm at inlet and outlet boundary conditions. The mesh sizing requirements are described in chapter 3. Blade boundary layer is produced by creating an o-grid around blade geometry. Hub and casing boundary layers are created by changing the sizing on the blocks adjacent to the geometry. Sizing of the first element is estimated with y^+ parameter as described in equation: 4.3. First element thickness in on the blade surfaces ranges from is $2\mu m$ on tip airfoil and $10\mu m$ on hub airfoil. This corresponds to $y^+ \approx 2$ calculated by streamline velocity values given in [17].

$$\Delta s = \frac{y^+ \mu}{U_{fric} \rho} \quad (4.3)$$

Where:

$$U_{fric} = \sqrt{\frac{\tau_{wall}}{\rho}} \quad (4.4)$$

Where:

$$\tau_{wall} = \frac{C_f \rho U_\infty^2}{2} \quad (4.5)$$

Where:

$$C_f = \frac{0.026}{Re_x^{1/7}} \quad (4.6)$$

Internal volume of the mesh was stabilized by attaching the mesh blocks to the internal design surfaces. This ensures that mesh layers are mostly coincident with the primary compressor flow. The internal surface mesh is also used as an internal boundary marker for data acquisition purposes. The markers are named hub, int-01 thru int-12 and int-tip corresponding to following locations of the design surfaces.

TABLE 4.2: Location of compressor desing surfaces

Boundary marker	Location
hub	0% span
int-01 -- int-12	7.7% -- 92.3% every 7.7% span
int-tip	100% span

Figure 4.5, provides overview of mesh quality defined by figure 4.1. Created mesh is of high quality and is sufficient for both RANS and DDES analyses (chapter 5). Final mesh reached roughly 11.5 million cell count. Final mesh is presented in figure 4.6

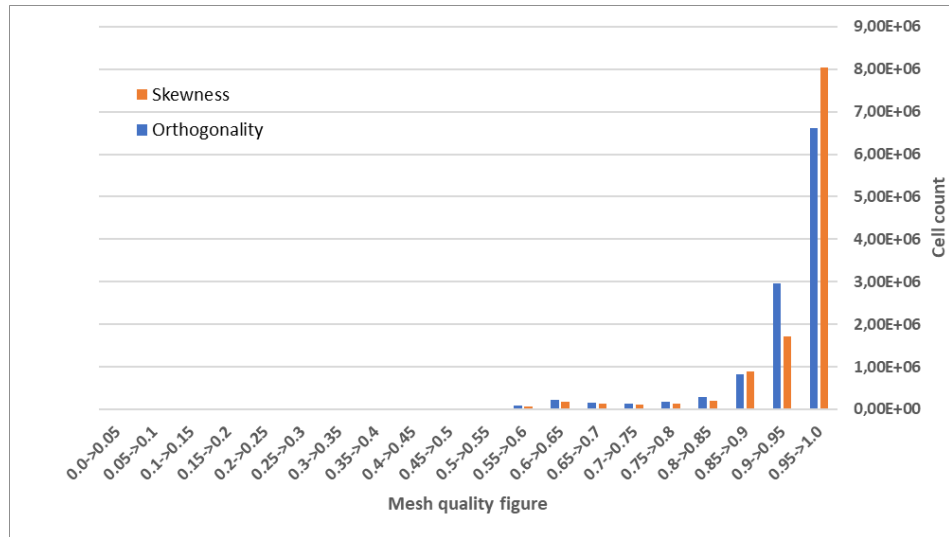


FIGURE 4.5: Mesh non-orthogonality histogram

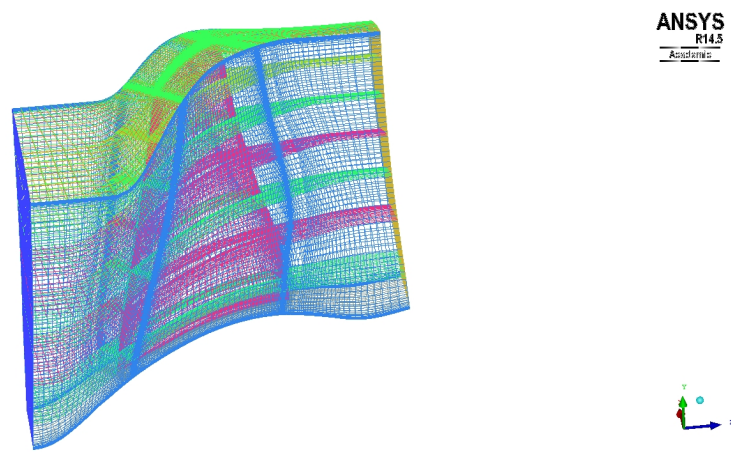


FIGURE 4.6: Completed Mesh

Chapter 5

CFD Analysis

5.1 Case preprocessing

CFD analyses for generating raw pressure field data are performed in ANSYS Fluent 17.2 software on Prometheus HPC cluster located in Kraków. Access for this infrastructure was granted by PLGrid infrastructure. Calculations were run on 5 nodes of 24CPU cores and 128GB RAM each [2], which resulted in decomposition to 120 cores, resulting in allocating around 110 thousand cells to a single HPC core.

Following, is the numerical setup applicable to all performed analyses. The setup corresponds to "peak efficiency conditions" given by the experimental study.

Material used in the analysis resembles standard air modeled as ideal gas as in equation with following properties described in table 5.1

TABLE 5.1: Standard air properties

C_p	1006.43	$\frac{J}{kg \cdot K}$
λ	0.0242	$\frac{W}{m \cdot K}$
μ	1.7894e-05	$\frac{kg}{m \cdot s}$
M	28.966	$\frac{kg}{kmol}$

$$pV = nRT \quad (5.1)$$

Analysis operating pressure is set to 0 Pascal, which is a standard practice in compressible flow CFD.

Internal mesh zone is set as "frozen rotor" - stationary reference frame. Although no mesh motion is implied, the effect of Coriolis accelerations and centrifugal acceleration will be taken into account by adding respective acceleration components to momentum equations as described in chapter 3. The rotational velocity is set to 1680 rad/s.

Following boundary conditions were applied to the mesh boundaries. Following setup is typical for compressible flow CFD.

TABLE 5.2: Test case boundary conditions

Boundary marker	Boundary type
Inlet	Pressure Inlet 101350 Pa
Outlet	Pressure Outlet 102000 Pa
Hub	Moving wall 1680 rad/s
Blade	Moving wall 1680 rad/s
Casing	Stationary wall
Internal profiles	Internal
Periodic boundaries	Interface

Moving wall boundaries represent the rotational velocity of the compressor blade and are necessary for stationary reference frame formulation. Boundary condition setup is no different to usual setups of analyses of such kind.

5.2 Flowfield initialization & RANS

RANS analysis is not suitable for generating acoustic nearfield data as the method averages the fluctuations over time (chapter 3). Yet, this approach is used to solve the initial flowfield at a relatively low computational cost. Furthermore the RANS analysis provides initial validation results for the test case and solver settings.

The solver is set up to steady-state, density based, coupled-implicit solver with $k - \omega SST$ turbulence model. Such setup is a go-to setup for nearly all compressible aerodynamics CFD done in the author's institute.

The density-based solver in ANSYS Fluent solves the governing equations of continuity, momentum, and (where appropriate) energy and species transport simultaneously as a set, or vector, of equations. Governing equations for additional scalars will be solved sequentially (that is, segregated from one another and from the coupled set). Two algorithms are available for solving the coupled set of equations, the coupled-explicit formulation and the coupled-implicit formulation [1].

The system of governing equations for a single-component fluid, written to describe the mean flow properties, is cast in integral Cartesian form for an arbitrary control volume V with differential surface area dA as follows:

$$\frac{\partial}{\partial t} \int_V W dV + \oint_V [F - G] \cdot dA = \int_V H dV \quad (5.2)$$

where:

$$W = \begin{bmatrix} \rho \\ \rho u \\ \rho v \\ \rho w \\ \rho E \end{bmatrix} \quad F = \begin{bmatrix} \rho v \\ \rho uv + pi \\ \rho vv + pj \\ \rho ww + pk \\ \rho vE + pv \end{bmatrix} \quad G = \begin{bmatrix} 0 \\ \tau_{xi} \\ \tau_{yi} \\ \tau_{zi} \\ \tau_{ij}v_j + q \end{bmatrix} \quad (5.3)$$

and where the vector H is the body forces and energy source vector.

The ρ, v, E, p are respectively the density, velocity, total energy per unit mass and pressure of the fluid. τ is the viscous stress tensor and q is the heat flux.

Total energy E and total enthalpy H are related by the formulas:

$$E = H - \frac{p}{\rho} \quad (5.4)$$

$$H = h + \frac{|v|^2}{2} \quad (5.5)$$

Equation 5.2 is than preconditioned, convective fluxes are splitted with Roe Flux-Difference Scheme and the preconditioned equation is discretized with Euler Implicit discretization and combined with Newton type linearization of fluxes. Obtained equation system is solved by the Incomplete Lower Upper (ILU) factorization in conjunction with the Algebraic-Multi-Grid. Details on the solver theory are available in source [1]

Flowfield is initialized at first with constant values populated from the "inlet" boundary condition patch. Next a Full-Multi-Grid initialization is performed to generate coarsened flowfield. The analysis is then processed by first, second and third order discretization schemes for all of the conservation values, up to a given residual value. It must be noted, that for second and third order scheme analyses, convergence criteria may not be reached. Should this case occur, the analysis is stopped once the residual plots reach a plateau and the resulting flowfield is considered acceptable. Once the third order scheme analysis is completed, data is acquired from inlet and outlet boundary conditions, and the constant pitch vs. span streamlines.

The analysis is set to a moderately strict residual convergence criteria of 10^{-6} , however is monitored during runtime. Once the convergence plot reaches plateau and the internal surfaces flow field is not changing throughout iterations the analysis is stopped and switched to a higher discretization scheme or stopped and saved.

5.3 DDES analysis

Once the RANS analysis is converged to a satisfactory level the setup is switched to DDES turbulence modeling.

The setup is changed to a transient, pressure-based, PISO scheme solver with DDES turbulence model and $k - \omega SST$ RANS formulation for shielded regions and subgrid scale. Rationale for the DDES analysis is provided in chapter 3. Pressure based solver is required by the DDES implementation in the used software. Utilization of the pressure based solvers for compressible flows is known to be unstable during the calculations, especially for the adverse pressure gradient cases. However, once the initial flow field resembles the final flowfield, the pressure based calculations are rather stable even at high velocity adverse pressure gradients.

Pressure based solver solves the discretized continuity equation with obtaining the velocity field from the momentum equations. The pressure field is obtained by solving and manipulating the continuity and momentum equations within a pressure velocity coupling scheme.

Transformed and discretized equations are solved by a linear solver and the intermittent solutions are coupled using a pressure velocity coupling algorithm. For this specific case PISO scheme is chosen for the computation. The algorithm is suitable for calculating problems with larger (in comparison to density-based acoustical timescale) pseudo-timestep and with decreased computational expense. Figure 5.1 presents the flow of the PISO algorithm.

The DDES Analysis is set up for two runs. As the flowfield resulting from the DDES Analysis is averaged and has no distinguishable features of a turbulent flow the first run is set to create a flowfield with random flow features. This is also used for testing the convergence and data acquisition process.

Although not required by the "frozen-rotor" configuration, the timestepping is based on the rotor Blade-Pass-Frequency number. The BPF parameter is obtained by formula 5.6

$$BPF = \frac{n \cdot t}{60} \quad (5.6)$$

where t is the number of blades and n is the rotational speed in rpm.

For NASA R67 the base Blade Passing Frequency is equal to 5882.36Hz . By multiplying the BPF by four a frequency of 23529.44Hz is obtained. This figure is above the human audible range and will be used to compute the timestep. As stated in chapter 3, in order to capture a given frequency, the timestep must be at least 4 times smaller than

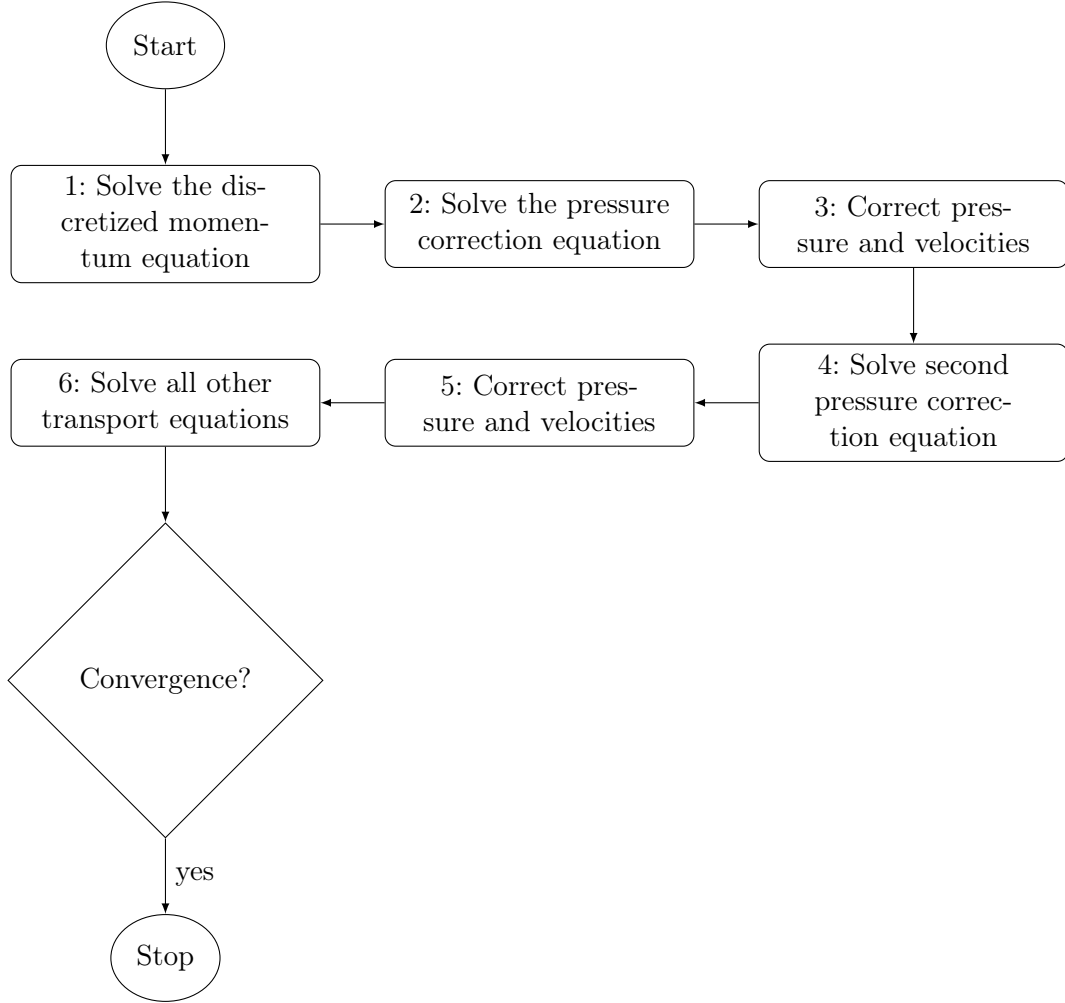


FIGURE 5.1: Flowchart of the PISO algorithm

the period of the oscillations (equation 3.66). By this approach the maximum timestep of the DDES calculation is $1.06 \cdot 10^{-5}s$. The timestep is compared with the requirements of the Courant-Friedrichs-Levy condition defined by equation 5.7

$$Co = \frac{u \cdot \Delta t}{\Delta x} \quad (5.7)$$

Considering that $u_{max} = 426.72m/s$ and $\Delta x = 0.25 \cdot \lambda = 0.003695m$ for desired frequency of $23529.44Hz$ and timestep of $1.06 \cdot 10^{-5}s$ the Courant number obtained is equal to 1.22. By rearranging the equation to solve for Δt an equation 5.8 is obtained and a calculation timestep fulfilling requirements of the CFD analysis and the direct noise formulation is computed and is equal to $8.659 \cdot 10^{-6}$.

$$\Delta t = \frac{Co \cdot \frac{\lambda}{4}}{u_{max}} \quad (5.8)$$

Initial timestep for the DDES analysis is set up to $5.0 \cdot 10^{-6}s$ with data acquisition

every 5 timesteps. First run was conducted for roughly 30 thousand timesteps, during which following factors were tested: calculation efficiency dependent on the CPU core count used, data output and data format, estimated storage requirements and the output from the embedded FW-H aeroacoustical models. First run concluded, that the assumed timestep does not meet the required convergence and produced inaccurate or even not physical results.

The timestep was gradually decreased to a value of $1.0 \cdot 10^{-6} s$, the CPU core count was set to 120 CPU cores distributed over 5 HPC nodes and the FW-H analysis output was disabled as the obtained results significantly distinguished from the expected physical values and delivered SPLdB was in range of 380dB.

Once the first run produced a fully developed flowfield with turbulent features characteristic to the LES analysis, the case was saved and set up for a final run with full data acquisition.

It was desired to capture at least 0.05 seconds of the flow but with some relation to geometric and operational features of the rotor. Based on the blade count and rotational speed of the rotor a time of a single periodic passage is calculated to $1.70 \cdot 10^{-4} s$. Next the required computational time is divided by the passage time to obtain the number of blade passages. 294.118 passages will occur during the 0.05s, so the number is rounded up to 295 passages and multiplied again by the passage time. Total calculation time of 0.05015 seconds is obtained. Therefore 50150 timesteps is required for full calculation runtime, with one passage being calculated in 170 steps.

5.4 Validation of the results

Reference [17] provides a very extensive set of validation data for whole passage. The quoted study presents results of LDA measurements of the NASA R67 compressor for relative mach number and relative flow angle at constant pitch and constant chord lines intersecting with blade span lines at 10% intervals. Constant pitch line is derived from the blade's suction surface: 0% percent pitch is the suction surface of one blade, 100% pitch is the suction surface of the adjacent blade. Constant chord lines are used to plot blade-to-blade distributions of given parameters at intersection of span and constant z-coordinate surface (5.2).

Full study consist of a very large number of plots, that are unnecessary for this particular thesis. To validate the CFD analysis, the constant pitch surfaces for 20%, 50% and 80% pitch are combined with 10%, 50% and 90% span locations, as measured from the blade tip, thus producing 9 lines to for relative Mach number and relative flow angle

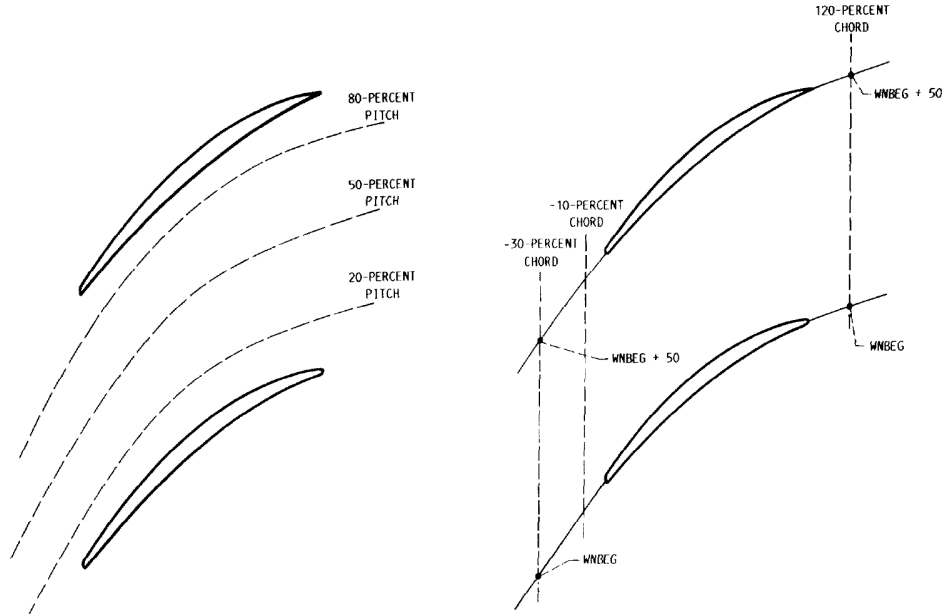


FIGURE 5.2: Schematic representation of constant pitch (left) and constant chord (right) to plot data [17]

data. For clarity, relative mach number plots and constant pitch plots are presented in appendix C.

The most simple method for validating the results is comparing the total and static pressure values on inlet and outlet boundary conditions of the domain with experimental data. Plots for static and total pressure at inlets and outlets of the domain are presented in figures 5.3 and 5.4.

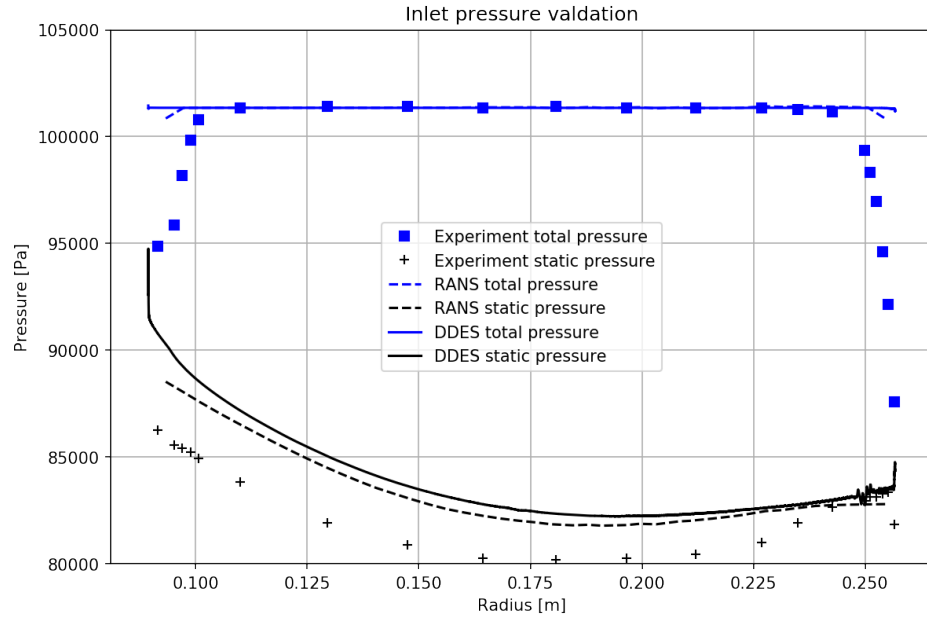


FIGURE 5.3: Inlet pressure validation

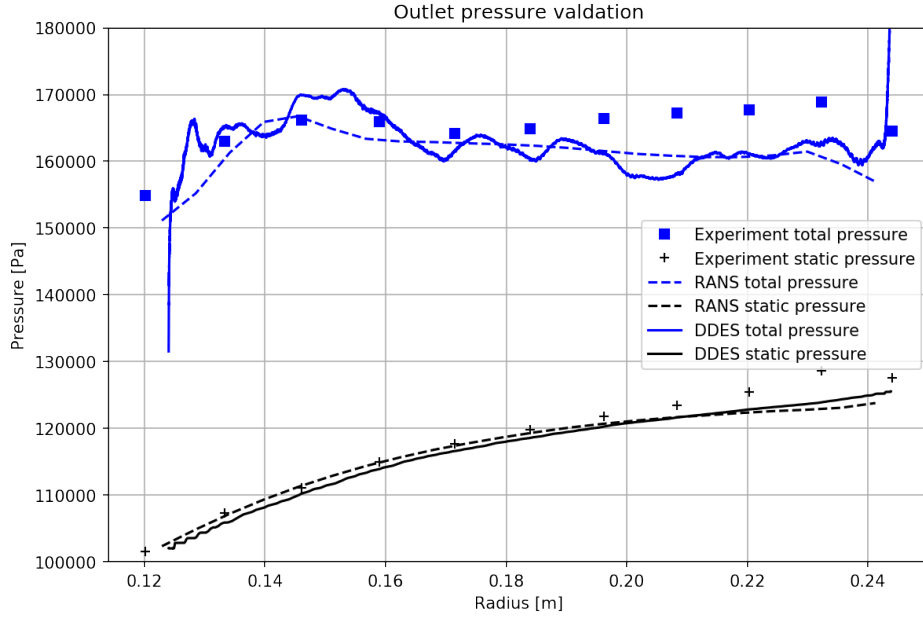


FIGURE 5.4: Outlet pressure validation

Both RANS and DDES analyses produce results that are confirmed by the experimental data. Static inlet pressure plot show the discrepancy between experimental and CFD data resulting from a minor shift between the data acquisition planes. The inlet boundary condition is moved closer towards the leading edge of the rotor, than the experimental pressure measurements array, therefore the static pressure is increased. The Mach number contour plots on the corresponding internal surfaces show the same character of the flow. Discrepancies between the 10% and 90% span plot and the int-01 and int-12 surfaces respectively, come from a slight offset between the surfaces as the mesh internal surfaces are located at 7.5% and 92.5% span respectively.

Chapter 6

Results of flow field noise analysis

6.1 Transition from flow-field to sound signal data

The performed DDES analysis delivered a set of files for further postprocessing. Values of static pressure, velocity magnitude, vorticity magnitude, static density and static temperature were gathered from designated boundaries and internal surfaces representing the design streamline cones. The dataset consists of 50150 files for each of the 13 internal surfaces and 5 blade boundaries, resulting in over 5.5 TB of data.

This set was postprocessed to obtain the sound pressure, sound intensity and their respective decibel values for each time step. The mathematical formulas for obtaining these values are provided in chapter 3 and the Python 3.5x implementation of which is presented in appendix D. The postprocessing of flow field data to sound data was performed on the same HPC infrastructure as the DDES analysis, due to the file accessibility. Postprocessed dataset was saved in a folder structure resembling the source files. The dataset consists of 902 700 files and another 5.5TB of data in form of comma separated values.

6.2 RMS results

6.2.1 Results postprocessing

The time specific sound pressure values were further processed to obtain the Root Mean Square values of sound pressure and sound intensity from internal markers and blade surfaces. Due to large number of figures, the scatter plots of the aforementioned values are provided in the Appendix A in figures A.1 thru A.54. Providing data for both pressure and intensity values and their decibel levels is redundant, yet both plots are shown for clarity and direct comparison of given values.

Internal boundary plots provide information on maximum and minimum values of SPL and SPLdB presented on the plot. As the minimum sound intensity (SIL) is equal 0 and the SILdB values for corresponding points approach negative infinity. Such values were overridden to show 0 SILdB on the plot. For this reason minimum value coordinates are omitted in the plot description

Blade surface plot is composed by plotting five datasets on one canvas and manipulating the sign of the canvas x-axis to mimic various view projections. Tool used to generate the scatter plots for blade surface overlaps the datapoints that share the same canvas x and canvas y coordinates, therefore the plotting order is always "back-to-front", so that the surface closest to the viewer is plotted atop the canvas.

Sound pressure and intensity plots are scaled with a normalized logarithmic colorbar with common scale across all of the internal surface and blade surface plots. For sound pressure, the maximum obtained value is $13917.395[\text{Pa}]$, so the maximum value of the colorbar is liberally rounded up to $15000[\text{Pa}]$. Minimum value for SPL is in range of $10[\text{Pa}]$, so the lower bar limit is set to zero. As for the Decibel values the lowest obtained value is around 116dB , largest - around 177dB . The colorbar scale is therefore set to $100 - 180 \text{ dB}$ range with linear scale. The same approach was used for maximum values of sound intensity. For sound intensity itself, the colorbar was limited from 0W/m^2 to $1.2 \cdot 10^6[\text{W/m}^2]$ and normalized to logarithmic scale. For SILdB plot, the bar range is limited to 0dB to 180dB range with linear scale.

Plots are created by projecting points from 3D surface onto a 2D plane of the plot, therefore some shape aberrations may occur. Color of the point is normalized as described above. The axes names correspond to the global coordinate system axes. Length unit for all plots is meter.

6.2.2 Qualitative analysis

Averaged sound pressure and sound intensity plots provide some information on the character of the acoustic phenomena modelled in a stationary reference frame for given test compressor.

The sound pressure fluctuations that translate to high SPLdB values occur in regions where flow is turbulent. For internal controll surfaces, where flow is globally subsonic (int-01, int-02, int-03 – figures A.5 thru A.14), the sources of the aerodynamically induced noise correspond to the regions on flow separation on the suction (upper on the plots). This is especially visible in the wake of the blade. Figures A.1 and A.2 provide the view of the blade's suction surface. A separation of the flow at leading-edge-to-hub transition leading to a very characteristic secondary flow and corner stall separation (separated flow on the suction surface near the trailing-edge-to-hub transition). The largest pressure

fluctuations were noted on the trailing edge and trailing-edge-to-tip transition, which is visible on both blade surface plots and internal surfaces plots.

Internal surface contour plots show, that the source of sound pressure is the supersonic-to-subsonic transition occurring on the shockwave. The effect of shock induced flow separation is becoming visible on internal surface plots for surfaces int-04 and int-05 (figures A.15 thru A.22), with full visibility of described phenomena on surfaces int-06 thru int-12 (figures A.23 thru A.50). Plot for surface adjacent to the blade tip (surface int-tip, figures A.51 thru A.54) show the effect of "tip-leakage" phenomena when high pressure flow at the pressure side of the compressor creeps to the low pressure suction side thru the tip gap (Fig. 6.1).

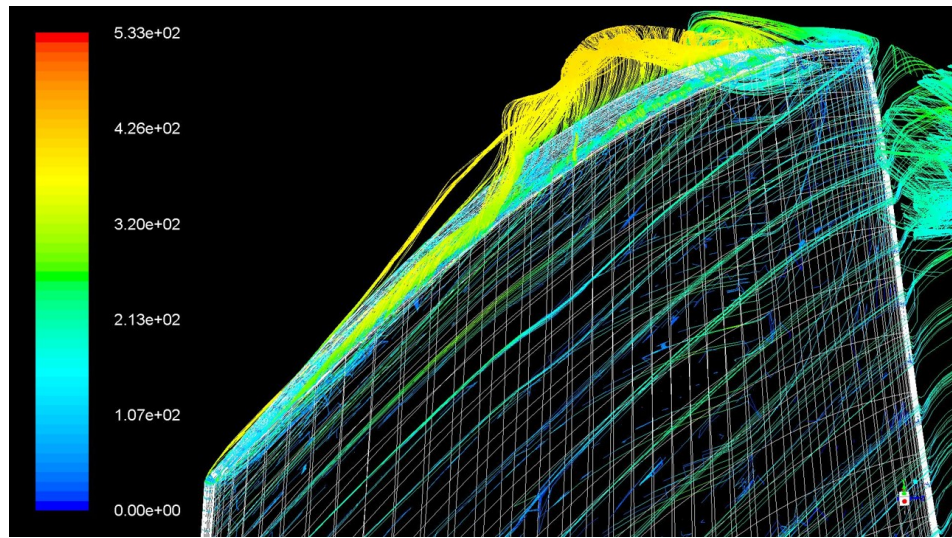


FIGURE 6.1: Tip gap streamlines. Velocity in [m/s]

Presented contour plots show a rather significant noise level in the supersonic (relative to the blade) region along with patterns resembling sound waves. SPLdB noise level in lower range of 120 decibels corresponds to pressure fluctuations in range of 20 Pa in medium where average static pressure is in range of 10^5 Pa, which may result from typical for transient calculations pressure fluctuations.

Sound wave like patterns on blade suction surface in the supersonic region require further investigation. Wave like pattern presented on the RMS plot is likely to show a sort of standing wave pattern evolving towards the leading edge of the blade. Region of flow for containing this phenomena is supersonic relatively to the blade, however both axial and radial components of the flow are subsonic. Moreover, the boundary layer flow for this case is subsonic even in the relative supersonic region, therefore sound propagation is possible near the blade surface.

6.3 FFT results

6.3.1 Results postprocessing

The time specific sound pressure values were further processed by a Python script presented in Appendix G. As described in chapter 5, the timestep for the analysis was order of magnitude smaller than required by the direct method. The presented algorithm samples every 10th timestep to an intermittent tabular data frame and performs a Discrete Fourier Transform as per formula 3.7. This outputs a complex vector 3.12 of 5015 Fourier coefficients, for every data point on an analyzed surface. Due to large number of figures, the scatter plots of the aforementioned values are provided in the Appendix B in figures B.1, B.2 and B.3.

Obtaining amplitudes and phase shift of ordinary frequencies is rather straightforward. Formulas 3.14 & 3.15 are used element-wise on a complex vector of Fourier coefficients for each node of given control surface. Results are saved to separate csv files with $\text{Amp}_k(f_{bin})$ and $\theta_k(f_{bin})$ data respectively.

A rather challenging is to graphically present the results of the analysis. At this stage, all nodes on a 3D control surface, having (x, y, z) coordinates are now linked to a 2D spectrum plot, therefore a dataset is now five dimensional. Considering that 3D surface can be projected to a 2d scatter plot, reduces the problem to 4 dimensions. For first assessment of spectrum plots a "spectrum heatmap" is proposed. A heatmap kind plot with x-axis being the frequency bins, y-axis – the node number, and cell color is the magnitude of given frequency bin of given node. Exemplary heatmap is presented in fig. 6.2. Such approach provides some basic qualitative insight to the frequency distribution.

Spectrum plot amplitude range as well as maximum FFT amplitude range are normalized and presented on a logarithmic scale as per formula 6.1.

$$\text{Amp}_{kn} = 20 \cdot \log_{10} \left(\frac{\text{Amp}_k}{\text{Amp}_{max}} \right) \quad (6.1)$$

where Amp_{max} is the global maximum amplitude of all datasets.

This operation has been performed separately on spectrum plots and peak amplitude plots. For spectrum plots the lower [dB] range is calculated by applying the formula 6.1 to global minimum and global maximum amplitudes, resulting in lower end of the scale of -226.41 dB, rounded down to -230dB. For surface plots, where only peak amplitudes are taken into account, the lower end of the plotting range is set as follows: obtain list of maximum amplitudes from all control surfaces, next take the minimum value from the obtained list and apply the aforementioned formula. The lower limit of the surface amplitude plots is calculated to -62.94 dB, rounded down to -65dB. This ensures

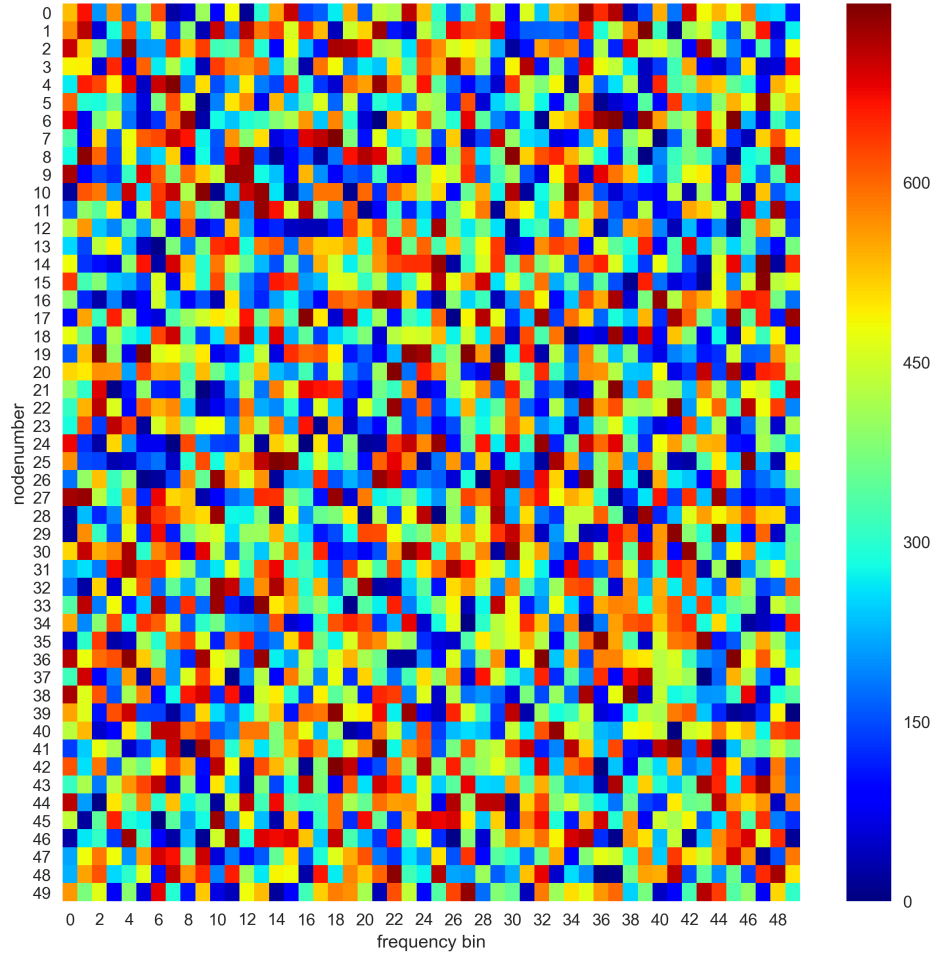


FIGURE 6.2: Exemplary FFT heatmap of magnitude. Random data.

that color range on is consistent throughout the spectrum plots and surface plots, with maximum value of 0 on every amplitude plot, corresponding to the maximum amplitude value.

Frequency of maximum amplitude for each node is obtained from the dataset. Moreover an amplitude weighted average frequency is calculated (eq. 6.2) to show the dominating frequency range on the given control surfaces. Frequency range presented on these plots is limited slightly above the maximum frequency possible to resolve by the presented approach and the limits are 0Hz and 25000Hz.

$$\bar{f} = \frac{\sum_{k=1}^N f_{bin_k} \cdot \text{Amp}_k}{\sum_{k=1}^N \text{Amp}_k} \quad (6.2)$$

6.3.2 Qualitative analysis

Analysis of the spectrum plots of the internal surfaces shows the following phenomena. At lower node numbers – towards the inlet of the domain, the lower frequencies are

dominant in the spectrum, with little or no high frequency constituents. With increasing node numbers – moving towards the domain outlet, the amplitude of the low frequencies is increasing, whilst the high frequency constituents are also increasing their magnitudes. This pattern is repeated throughout the internal surfaces plots, including the tip internal surface. Moreover, the general observation is, that the magnitudes of given frequency bins, for corresponding node numbers, is increasing along with the distance from the hub. Therefore, the "quietest" region of the flowfield is upstream of the blade and near the hub and the "volume" of the sound increases towards the trailing-edge-to-tip-juncture. One of the most important conclusions appearing from the spectrum plots is, that the flow nearfield sound, although having source in seemingly random flow fluctuations, is not random nor has a characteristic of white noise. The spectrum plots are lacking the information on the node locations, therefore spatial analysis of the plots poses some difficulties. Further analysis is done on internal surface and blade surface plots.

Amplitude weighted average frequency plots reduces the high dimensional FFT dataset to a plot feasible to show in a printed form. Frequency spectrum is averaged and constituents of high amplitude are highlighted on the plot. The averaged frequency is in higher range of c.a. 10kHz on the int-01 surface (Fig. B.5) and up to 15-16kHz on the int-tip surface (Fig. B.53). These frequencies are represented by a high pitched noise, characteristic to operating jet engines and being one of two main sources of noise of the engine. The plot is consistent with RMS sound pressure and sound intensity plots, suggesting, that the main contributor to the averaged RMS sound pressure is the high frequency noise.

Surface plots of frequencies of maximum FFT amplitude show, that the highest frequency oscillations occur in highly separated regions of the flow: in the wake behind the trailing edge of the blade and in the leading edge-hub juncture induced secondary flow. Surprisingly, the highest frequency fluctuations were captured in tip-to-trailing-edge juncture, which is the region where the largest RMS sound pressure values were noted.

Chapter 7

Conclusions & Further work

7.1 Results discussion

Initially, this thesis intended to investigate the following phenomena on a fan blade of a commercial large by-pass-ratio turbofan engine blade, yet no information on airfoil coordinates and efficiency figures of such devices are available for research purposes. It is assumed, that the phenomena that occur on such blade are similar in character to the ones obtained on the provided test case. Although the practical utilization of presented results is limited at this stage, some conclusion can be drawn out. The approach used on a NASA R67 transonic axial compressor provide some insight to noise generation phenomena in a "frozen-rotor" reference frame. It must be noted, that noise perceived by human or received by a microphone will be different from the ones presented. However, the noise perceived has it's source in the phenomena discussed in this thesis.

The main contributors to the blade's noise generation are the boundary layer separations induced by backflow in the boundary layer or by the shockwave boundary layer interaction. The existence of a shockwave in a device of that kind is also the main contributor of the so-called "buzzsaw noise", which may be recognized by simulating a rotor with a moving mesh and with a stationary receiver or data probe. Largest, in terms of amplitude and frequency, sound pressure fluctuations are found at the trailing edge of the blade and at trailing edge-tip junction. Sound pressure in decibel scale as well as average frequency per node of control surface are in expected range for this kind of device.

Following assumptions can be made. In order to reduce the noise generated by the transonic axial compressor blade one must eradicate the sources of separated flow and, if possible, provide a supersonic to subsonic transition of flow without inducing a shockwave. At time of preparation of this thesis, methods for inverse design of boundary shapes based on pressure and/or other design criteria exist in open source domain. Such software allows for generating airfoils for fixed wing aircraft and rotating machinery. Furthermore,

modification of shape of the blade trailing edge by implementing a shape that reduces the vortex shedding or at least the turbulence intensity in wake. At this stage, there are no suggestions for manipulating the frequency of the fluctuations.

Results of direct noise analysis on hub and casing surfaces are not presented due to a simple mistake – these surfaces were accidentally removed from the CFD solution export of the DDES analysis. Only one low frequency cycle is captured due to another mistake. As described in chapter 5, the timestep of the analysis was decreased by the order of magnitude in order to improve the analysis convergence. However, the solution export was still set up to deliver a dataset per timestep which resulted in a dataset 10 times larger than necessary, with no available walltime to continue the calculation.

The main downside of the presented study is lack of validation data for acoustical nearfield of the given case. It is assumed, that the approach is valid when two following factors coincide: if the CFD analysis that generate flow-field data is validated by experimental data and if FFT and RMS scripts return the expected results while the input is a sum of sine waves of known frequency, amplitudes and phase shifts. The CFD analysis results were validated with the experimental data provided in reference [17] as described in chapter 5, therefore it is assumed that the DDES flowfield data is valid. The RMS script return the expected average amplitude value while processing a set of sine wave signals, whereas the FFT script returned proper frequency spectrum and phase shift of the given signal. By this indirect validation, it is assumed that presented results are valid.

7.2 Improvements to the method

Current approach may be compared to attempts of resolving a turbulent boundary layer with one finite volume element at the boundary wall. Although mathematically possible (and used in wall modeled turbulence models) it is valid under fulfilling some assumptions. For presented direct approach, it is assumed that sinusoidal fluctuation of wavelength enclosed by four finite volumes and resolved by four timesteps.

Resolving a sinusoidal fluctuation with four finite volumes and four timesteps fulfills the continuity and momentum equations, any change in temperature, resulting in changing velocity of sound will disrupt the assumptions presented in chapter 3. FFT amplitude plots for ordinary frequencies, analyzed at random mesh points show, that the amplitudes of frequencies above the assumed by mesh and timestep range are dropped nearly to zero. A solution for this is using a finer mesh, capable of resolving shorter wavelength fluctuations, along with smaller timestepping to compensate for transition of sound wave in the finer mesh, especially in the boundary layer region and in the wake.

Considering that the mesh resolution is increased, a proper method for resolving turbulence flow is required. Although justified from the computational expense standpoint, the hybrid methods with shielding functions may result in filtering the source fluctuations at the boundary due to switching to the RANS part of given model. Using LES methods for further work will be considered.

Another aspect to be considered for improvement is the walltime management and data management. Presented analyses was performed on a Prometheus HPC and was distributed to 120 nodes. Normalized walltime for the analysis was above 1M CPU hours for both transition DDES and final DDES analyses and around 11TB of data was generated during the process. Using LES methods requires meshes of much greater density and therefore meshes of at least order of magnitude larger than used in this case. Assuming that walltime requirement is scaled linearly with the mesh size, assumed LES analysis of the presented test case, would have had required more than 10M CPU hours and around 1000CPU nodes.

Realtime processing of data to obtain sound information in the flowfield is impractical if even possible for full meshes, due to the amount of data generated. An efficient and high capacity storage storage is therefore required for performing direct approach analyses of sound on full flowfield.

Post-processing of data obtained in this study was performed with use of Matplotlib Pyplot library available for Python scripting language and hence the information about mesh was dropped during the process. This is visible especially in the internal surface scatter plots where lack of interpolation between points is visible. Using a post-processing tool with custom filters such as Paraview, or implementing a mesh file reader into Python (or any other implementation) scripts will solve problem with interpolation of data and allow visualization of full flowfield datasets.

7.3 Further work

As stated above, lack of validation case that directly checks the acoustical nearfield results is somewhat of a challenge. Therefore developing an experimental and numerical case of known acoustic nearfield properties is required.

The implementation of mesh reading or mapping to mesh functionality will be developed in further versions of the post-processing scripts. This will allow for more efficient qualitative an quantitative analysis of the obtained data.

Presented work describes a single passage of the compressor in stationary reference frame ("Frozen rotor") configuration and gives insight to basic aerodynamic phenomena contributing to noise. In order to asses the noise generation in compressor, or fan, flows

the analysis ought to be performed with use of rotating mesh with sliding interfaces and include effects of rotor-to-stator interaction, as well as interaction with compressor hub and casing. Furthermore, performing data acquisition and processing on full flow-field of the given case will give a better opportunity to post-process the obtained data. By extending the analysis time to more than 1 cycle of low frequency sound (0.05s), and preferably to more than five of such cycles, it may be possible to obtain information on acoustical wave modes within the flowfield of the case subject to study.

Considering that the geometry of given case is periodic, assuming the periodicity of flow in the DDES and LES analysis is prone to over constraining the resulting flowfield. Hence the analyses should be conducted on full rotor-stator stage, or at least a large portion of a stage, to eradicate or minimize the effect of periodic boundary conditions. This, combined with proposed LES simulation, enforces using a mesh with cell count in 10^8 order of magnitude, which leads to further challenges with data management and required computational resources.

7.4 Closing remarks

The study presented in this thesis can be interpreted two-wise. One as a case study on direct formulation of noise analysis and providing the minimum requirements towards the analysis. Second aspect is the study of generating sound by the transonic axial compressor rotor blade. Both aspects of the study are, at least partially, fulfilled.

The provided minimum requirements of the analysis proved to work at relatively high computational expense. Yet, using the acoustical analogies implemented into used CFD code with transonic flows with shockwaves is unjustified by the mathematical formulation of the FW-H analogy. The resolution of the obtained acoustical nearfield can be improved at a cost of higher computational power requirements.

The presented results of the compressors acoustical nearfield are rather expected and are relateable to relative mach number fields and time averaged static pressure fields. Results identify the sources of aerodynamic noise that are consistent with ones described in literature, turbulent regions of the flow are the source of pressure fluctuations of high amplitude and high frequency. Propagation of sound waves was captured for lower end of the frequency spectrum, while the effect of high pitch noise is captured as an increase in RMS sound pressure and decibel figures. These results can be used to design a compressor blade that generates lower aerodynamically induced noise.

The method will be improved in terms of efficiency and data storage and attempted to be used in other technical entities where noise generation and acoustical wave mode assessment is required.

Appendix A

RMS values plots

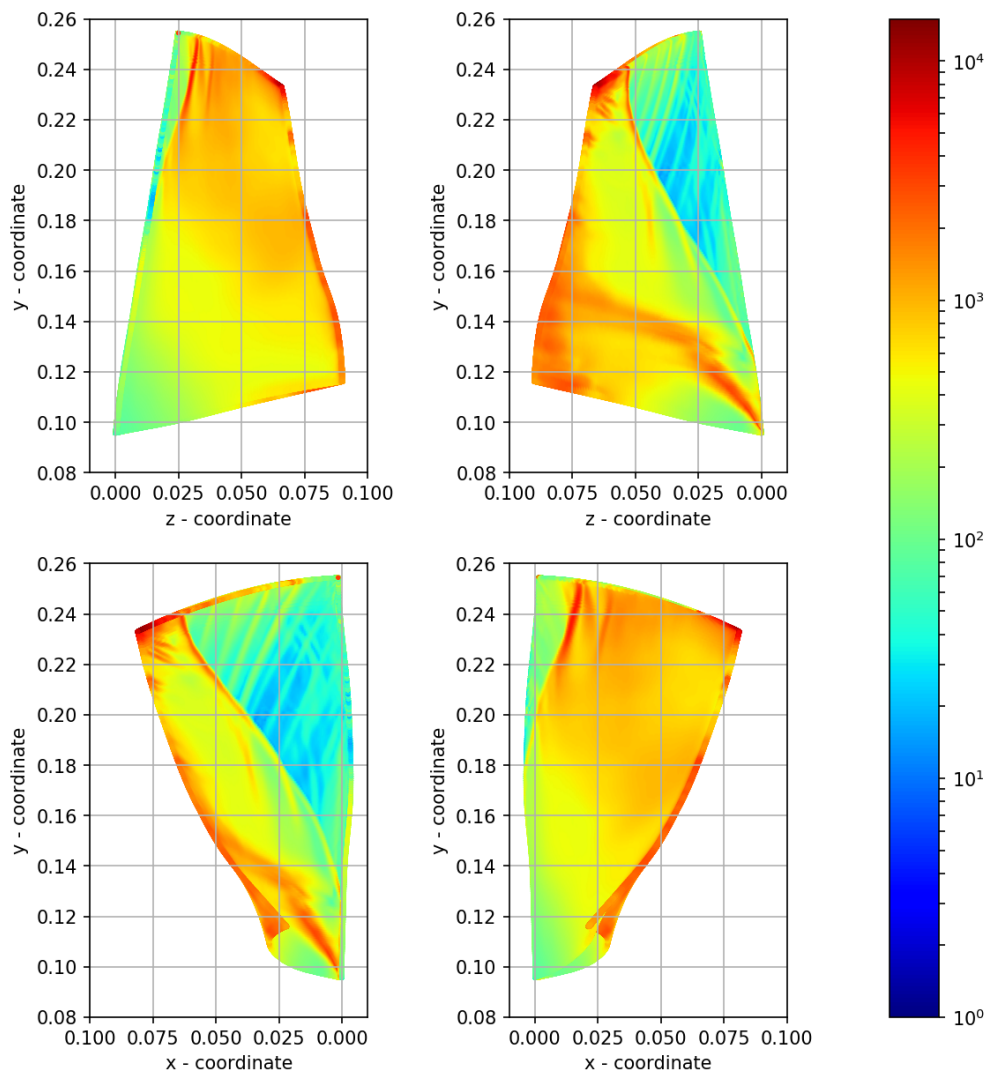


FIGURE A.1: Blade surface RMS Sound pressure [Pa]

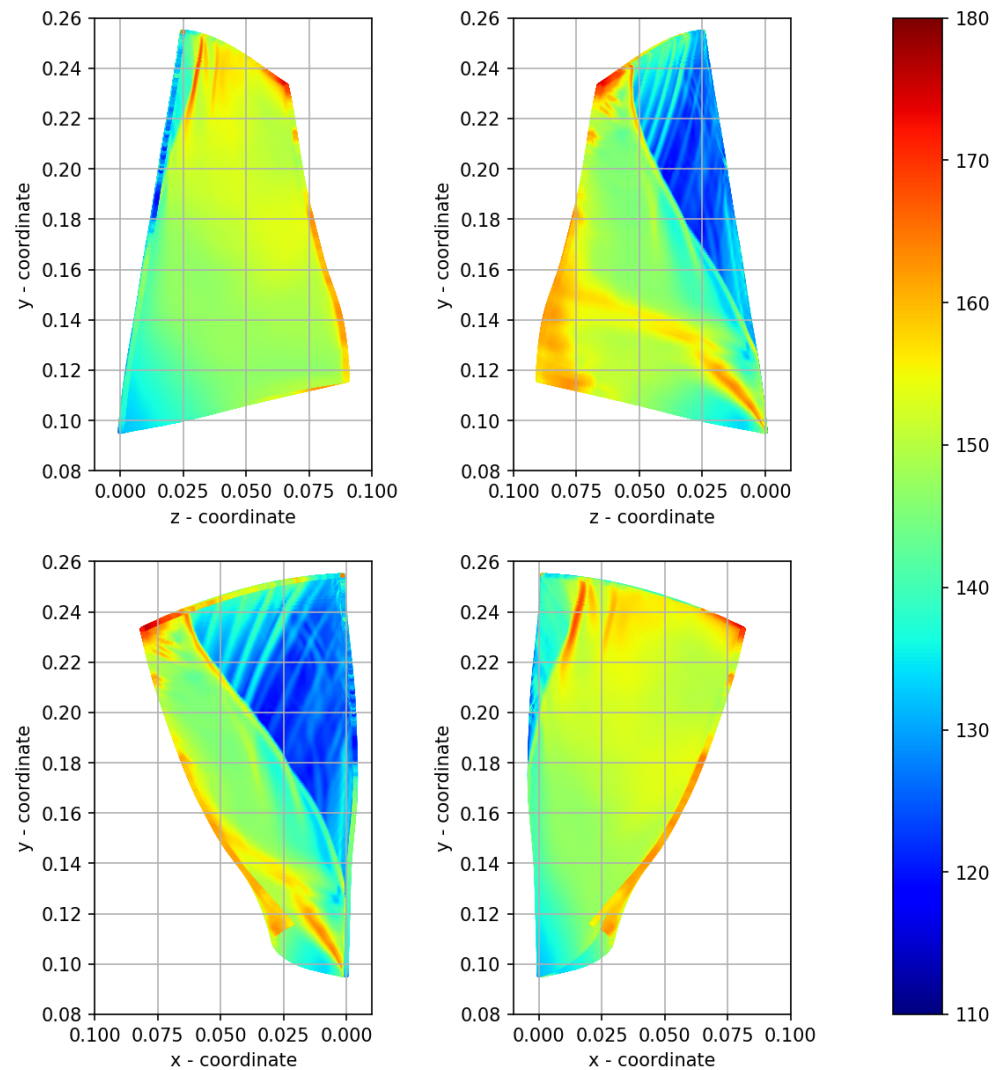


FIGURE A.2: Blade surface RMS SPLdB [dB]

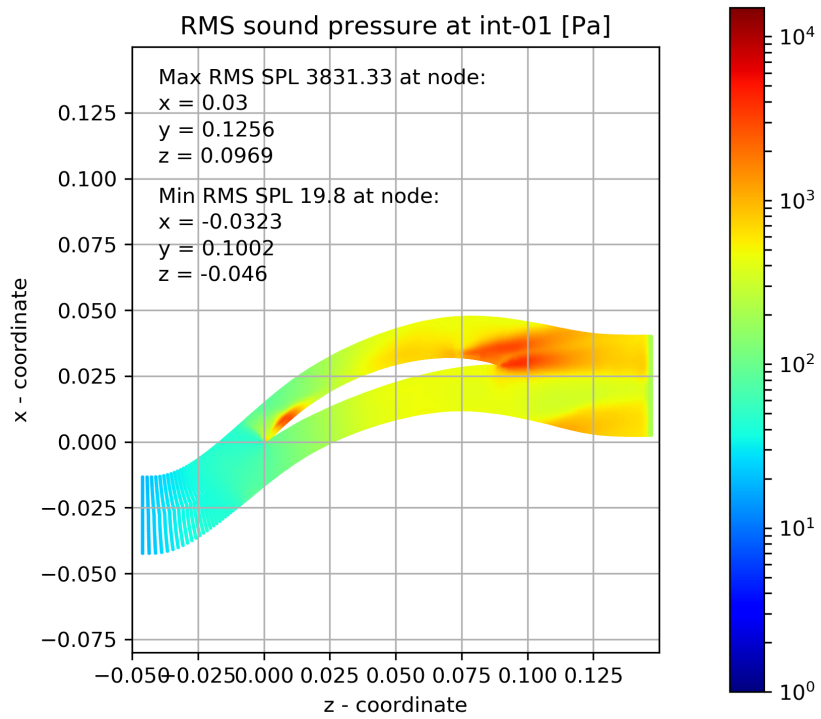


FIGURE A.3: RMS Sound pressure at int-01 mark

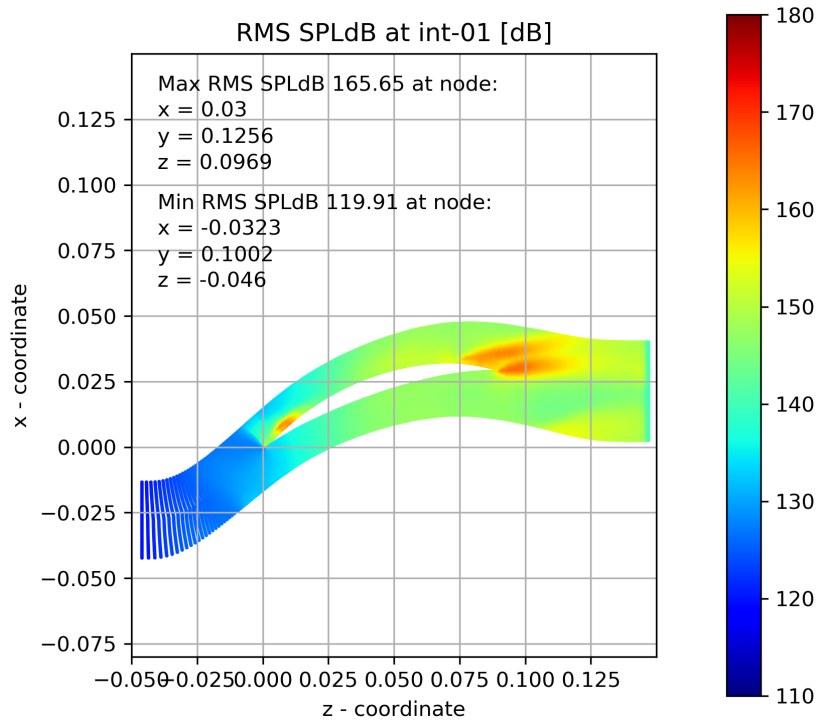


FIGURE A.4: RMS Sound pressure decibel level at int-01 mark

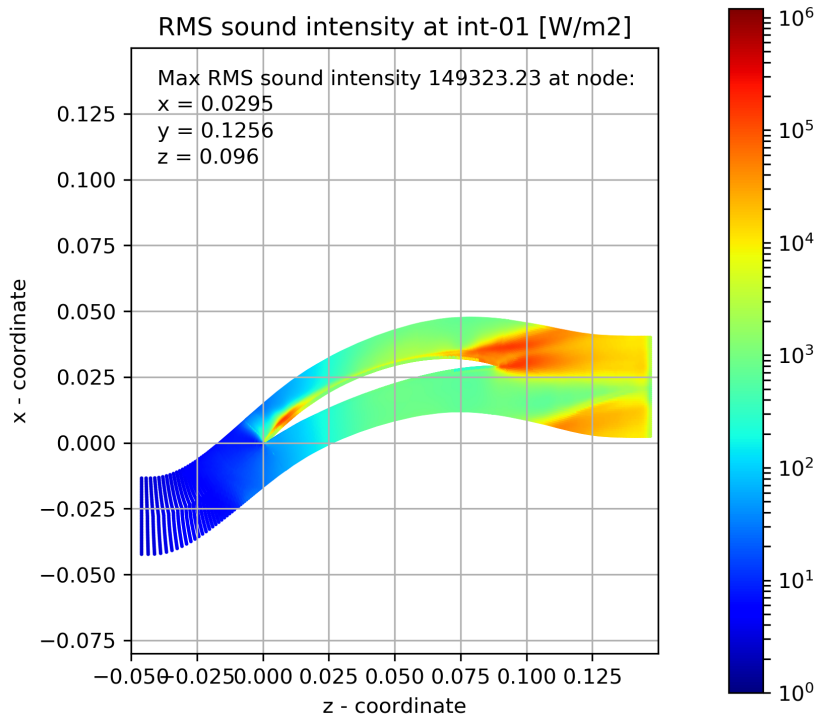


FIGURE A.5: RMS Sound intensity at int-01 mark

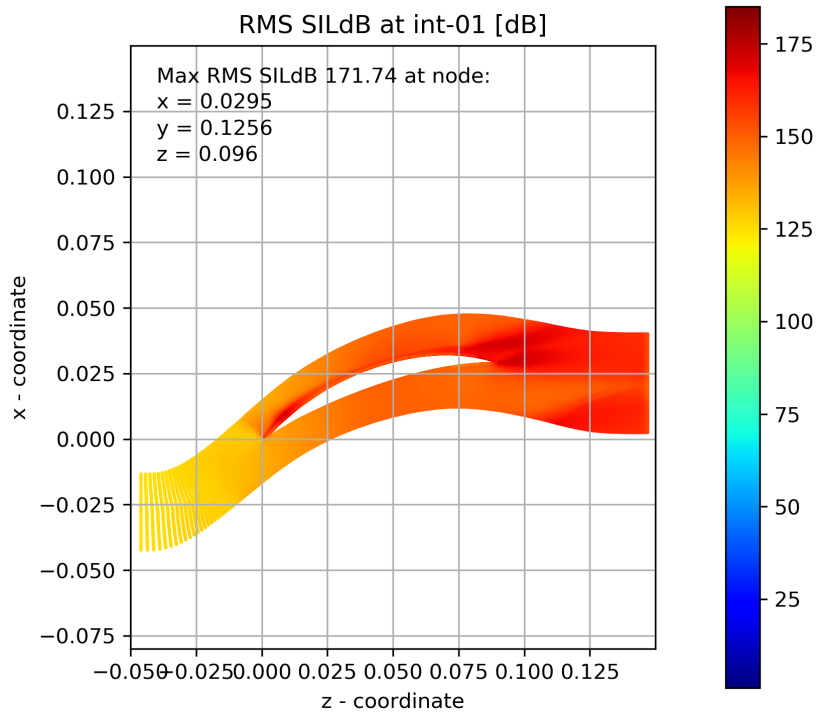


FIGURE A.6: RMS Sound intensity decibel level at int-01 mark

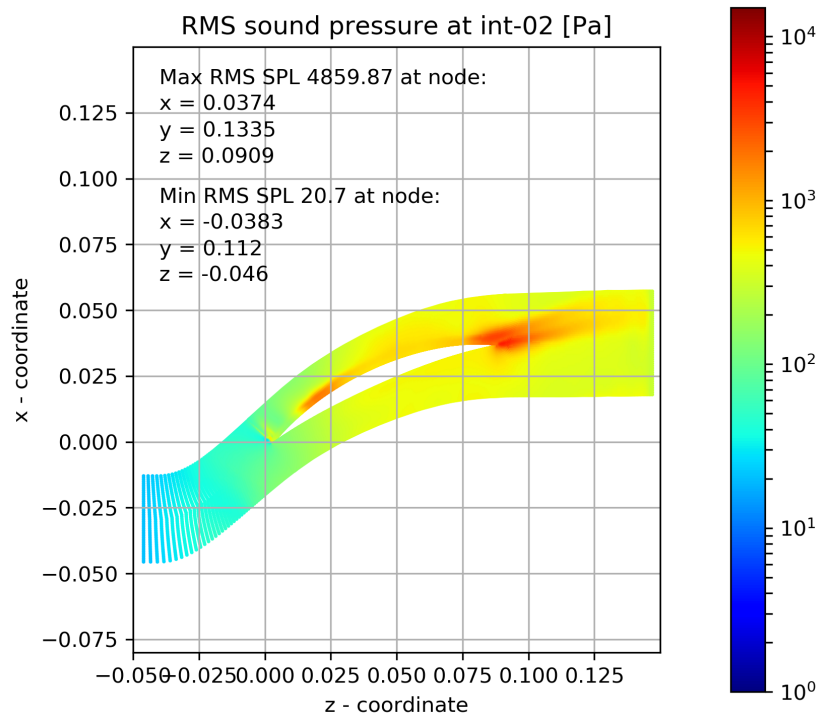


FIGURE A.7: RMS Sound pressure at int-02 mark

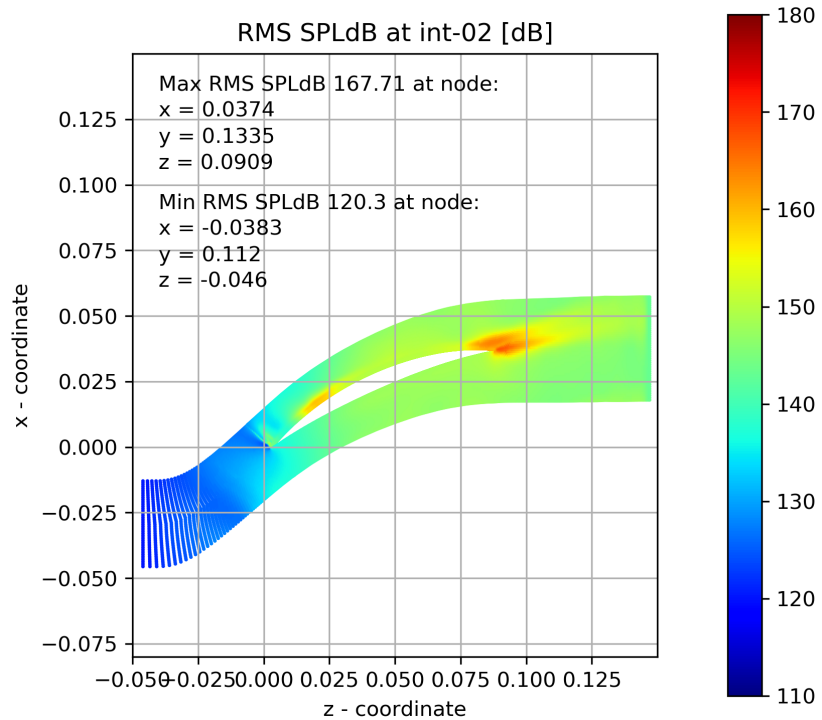


FIGURE A.8: RMS Sound pressure decibel level at int-02 mark

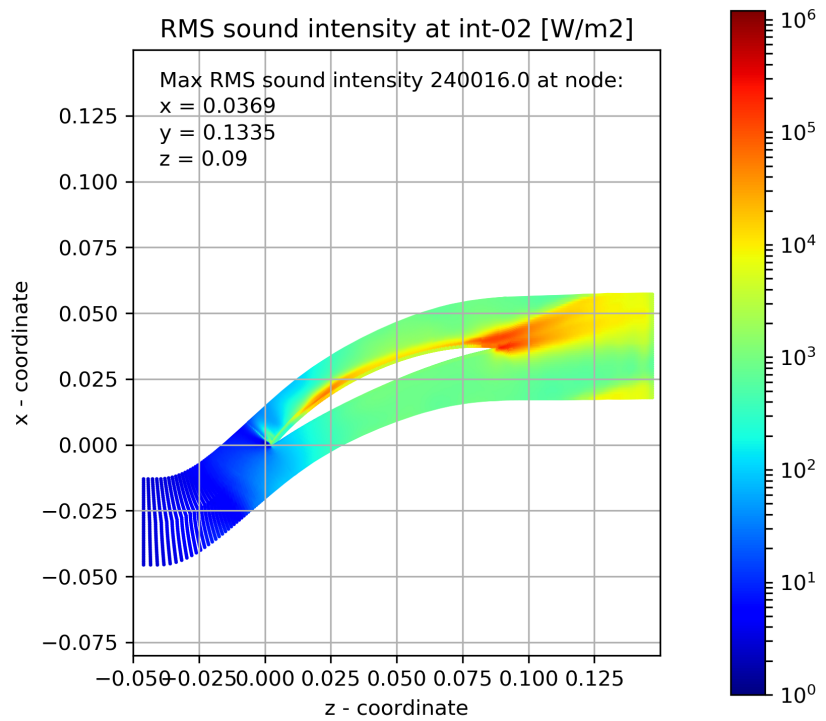


FIGURE A.9: RMS Sound intensity at int-02 mark

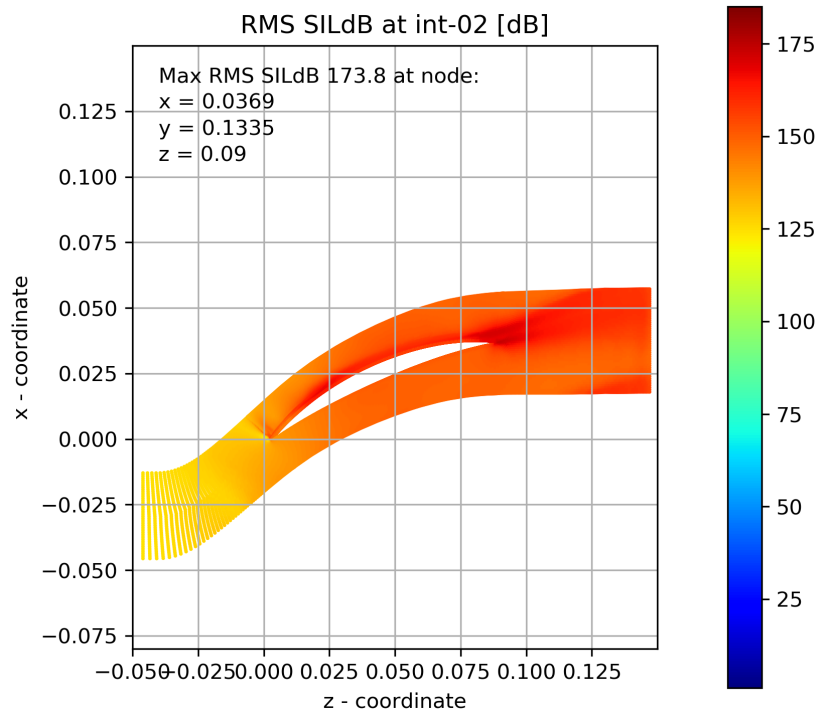


FIGURE A.10: RMS Sound intensity decibel level at int-02 mark

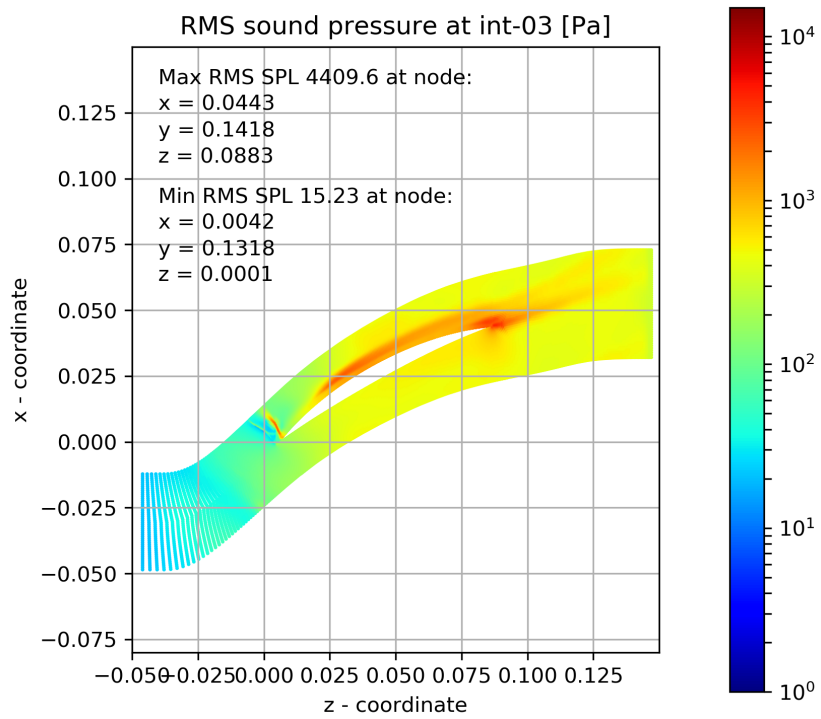


FIGURE A.11: RMS Sound pressure at int-03 mark

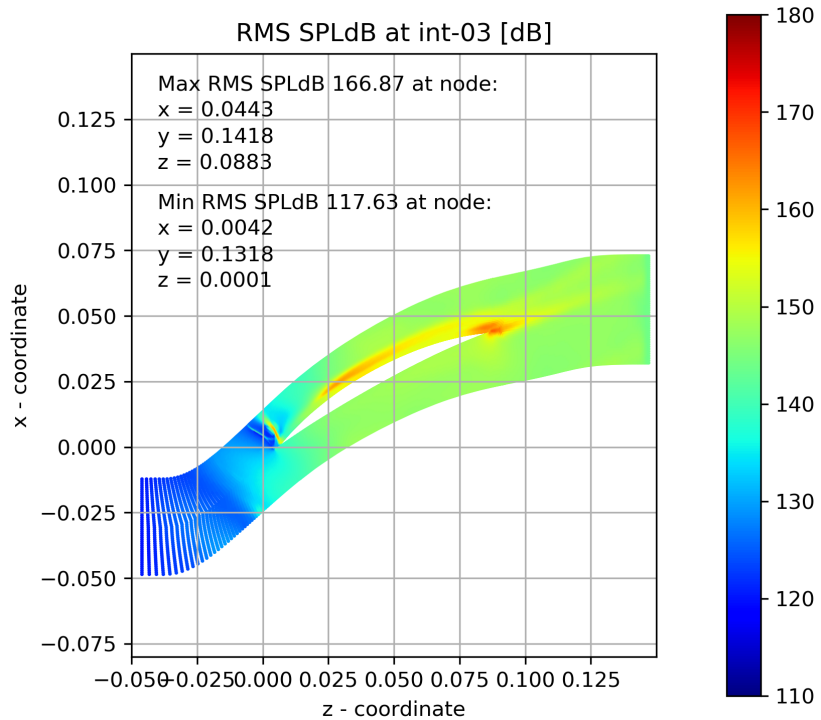


FIGURE A.12: RMS Sound pressure decibel level at int-03 mark

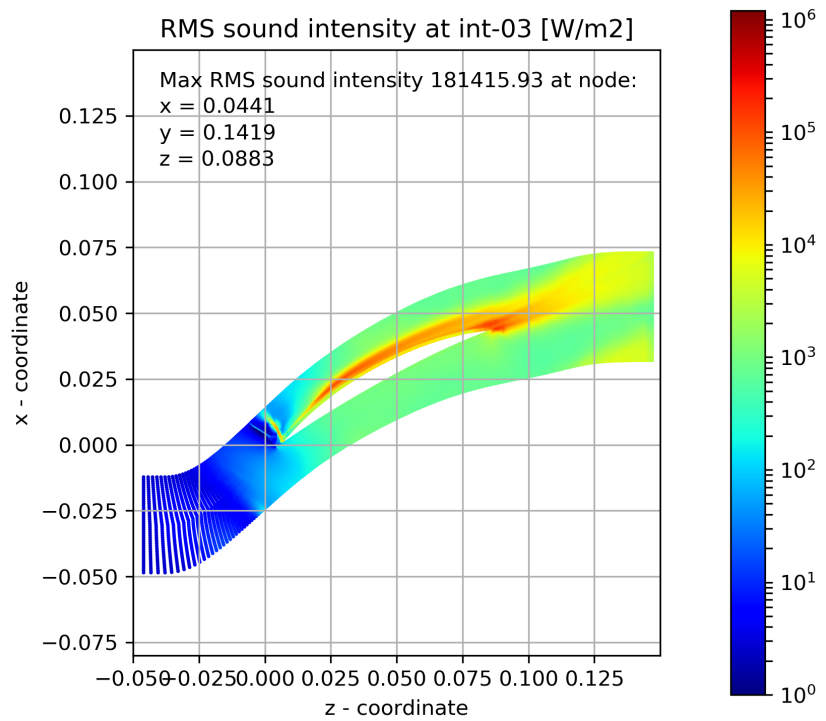


FIGURE A.13: RMS Sound intensity at int-03 mark

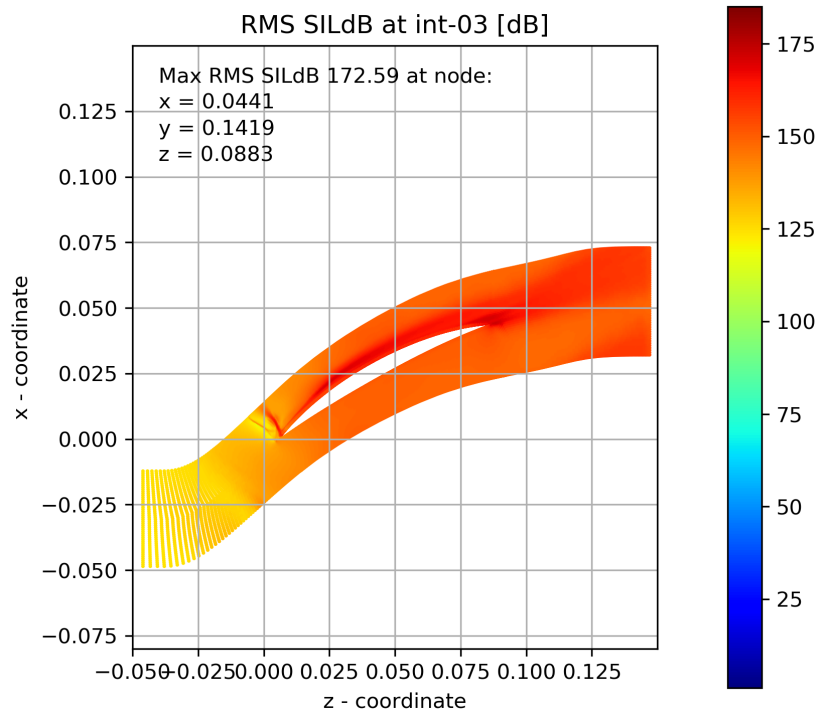


FIGURE A.14: RMS Sound intensity decibel level at int-03 mark

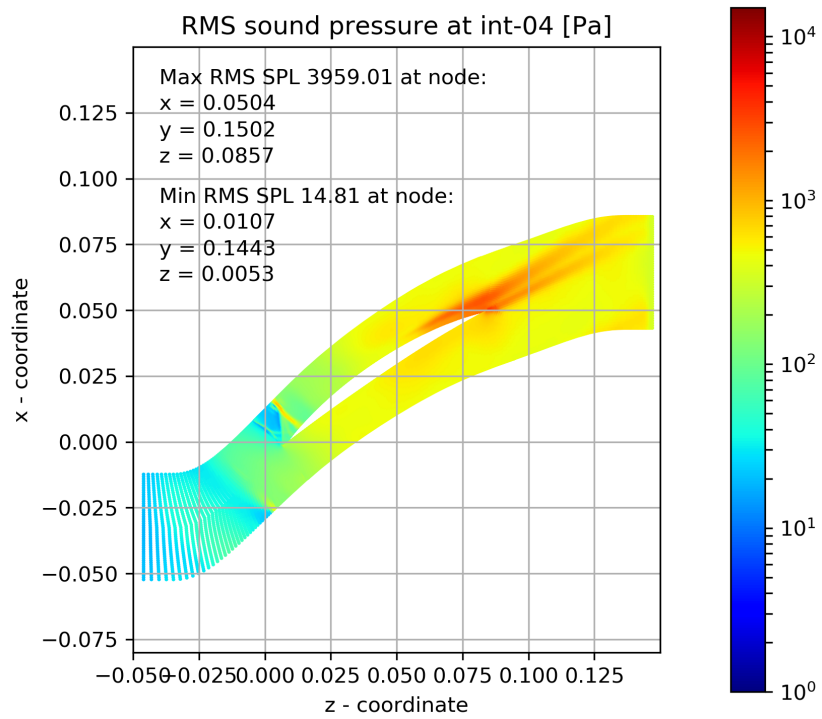


FIGURE A.15: RMS Sound pressure at int-04 mark

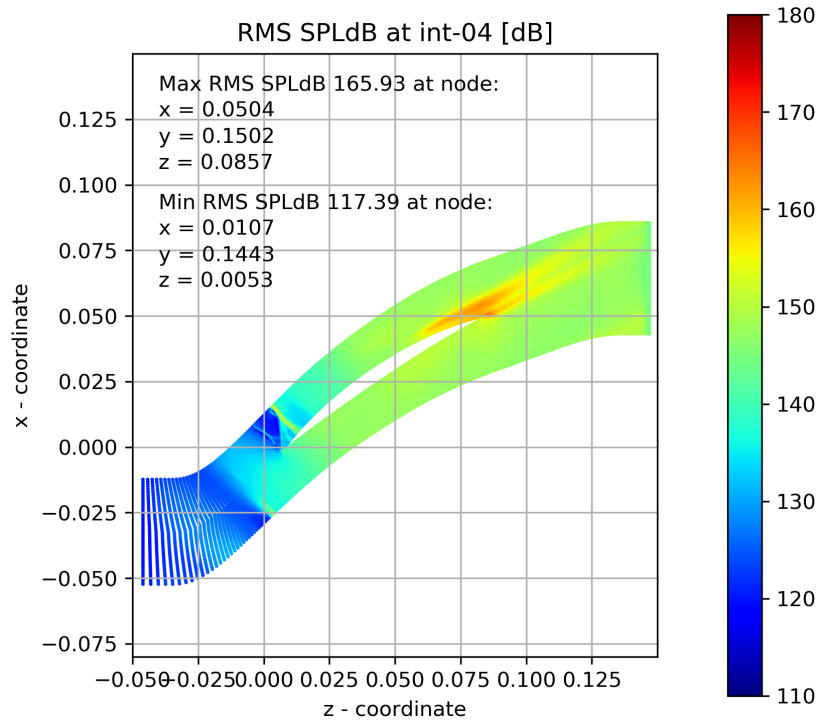


FIGURE A.16: RMS Sound pressure decibel level at int-04 mark

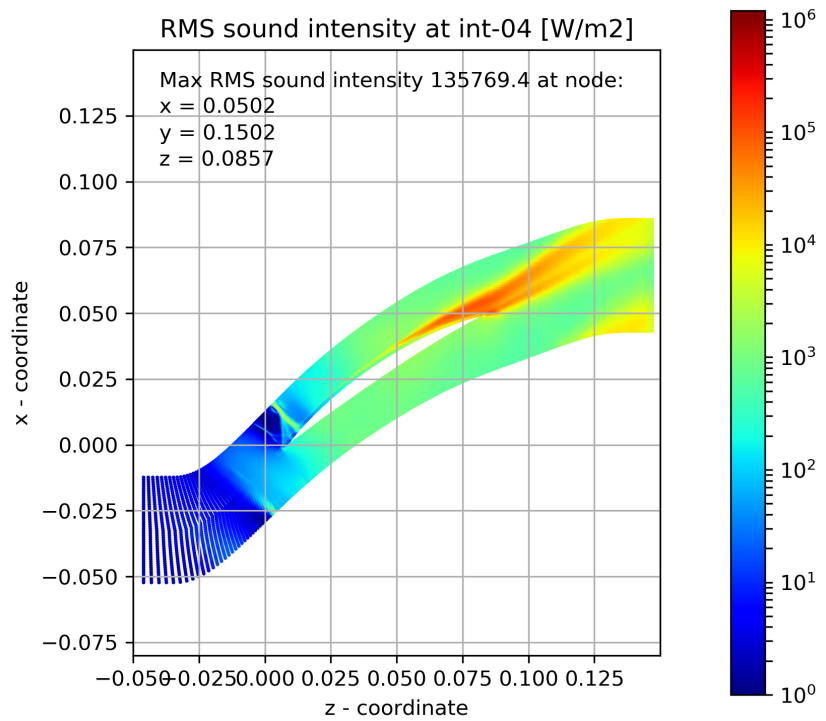


FIGURE A.17: RMS Sound intensity at int-04 mark

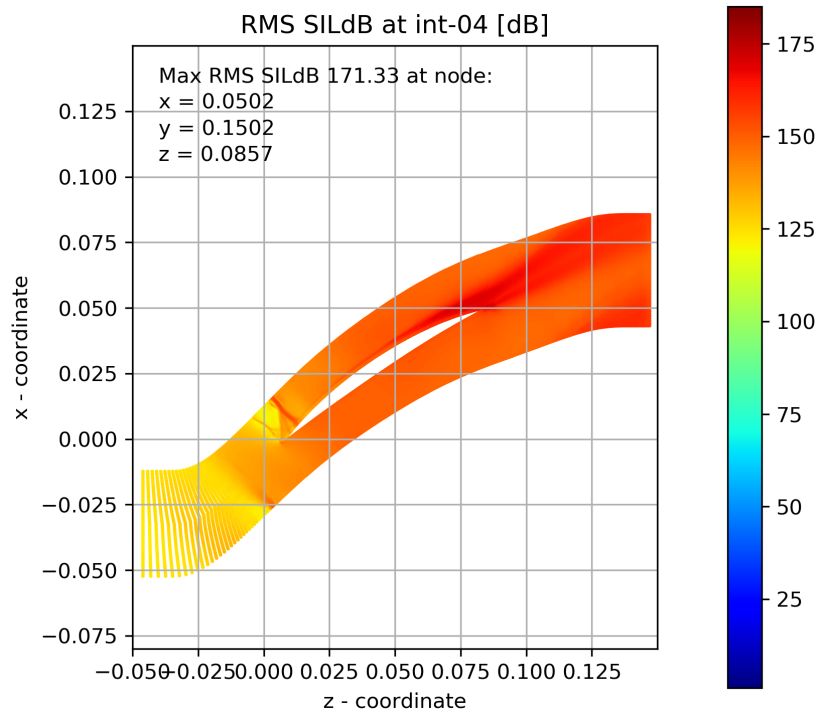


FIGURE A.18: RMS Sound intensity decibel level at int-04 mark

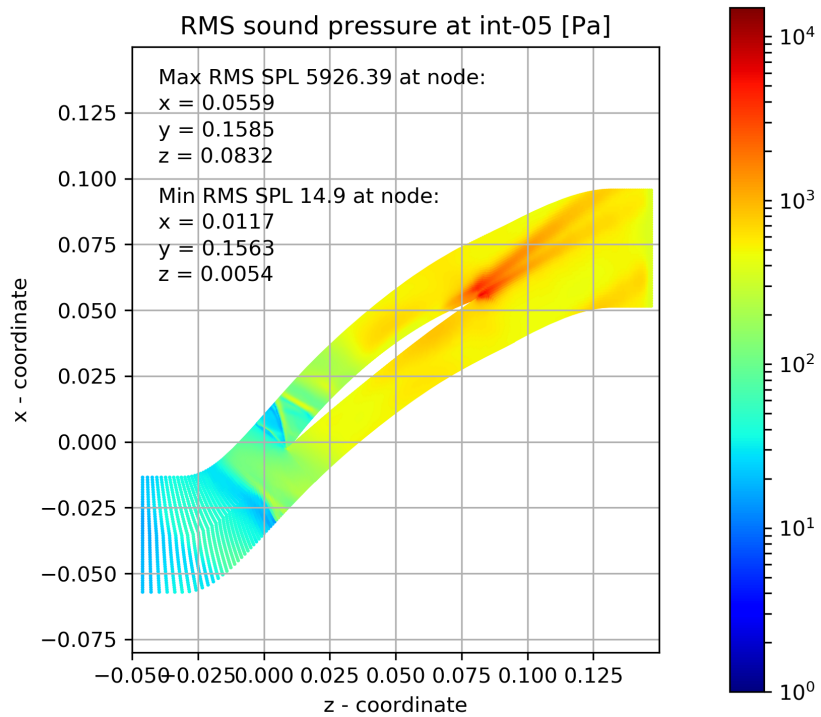


FIGURE A.19: RMS Sound pressure at int-05 mark

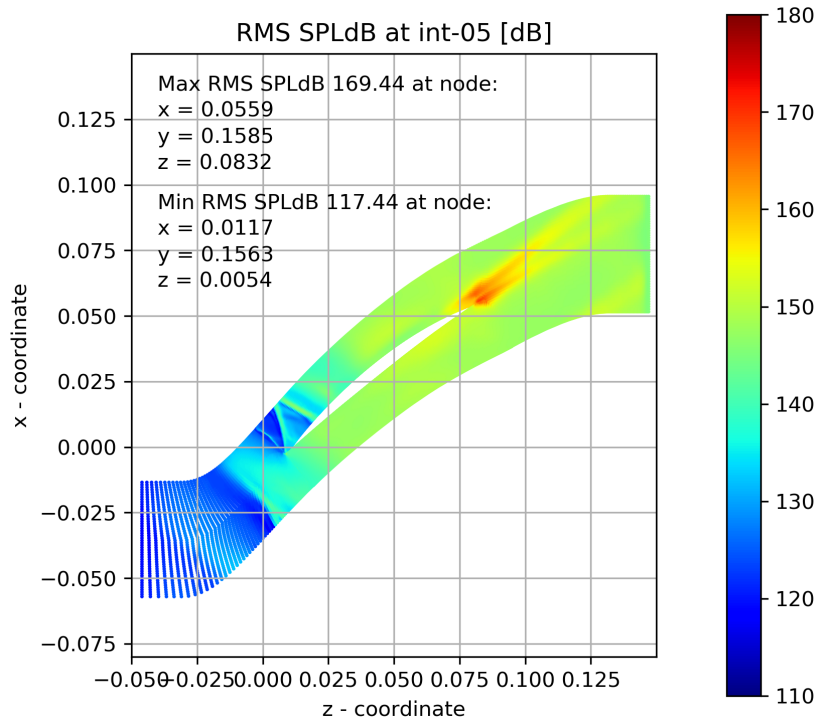


FIGURE A.20: RMS Sound pressure decibel level at int-05 mark

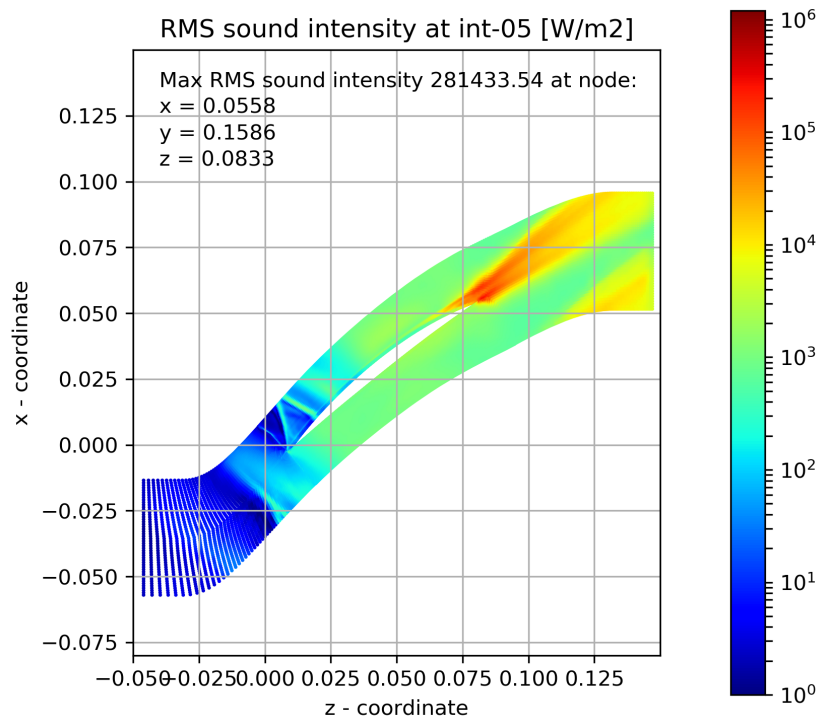


FIGURE A.21: RMS Sound intensity at int-05 mark

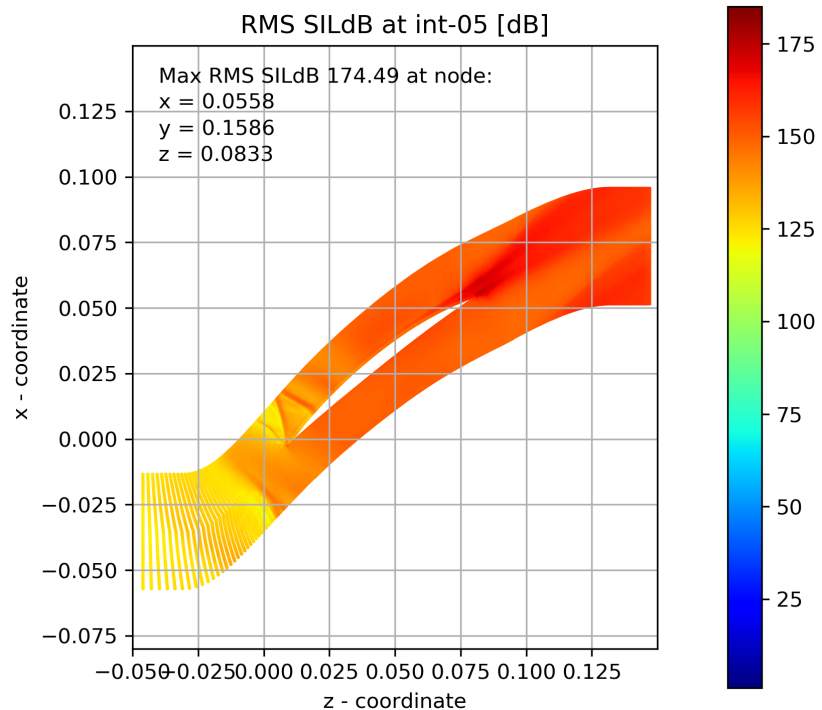


FIGURE A.22: RMS Sound intensity decibel level at int-05 mark

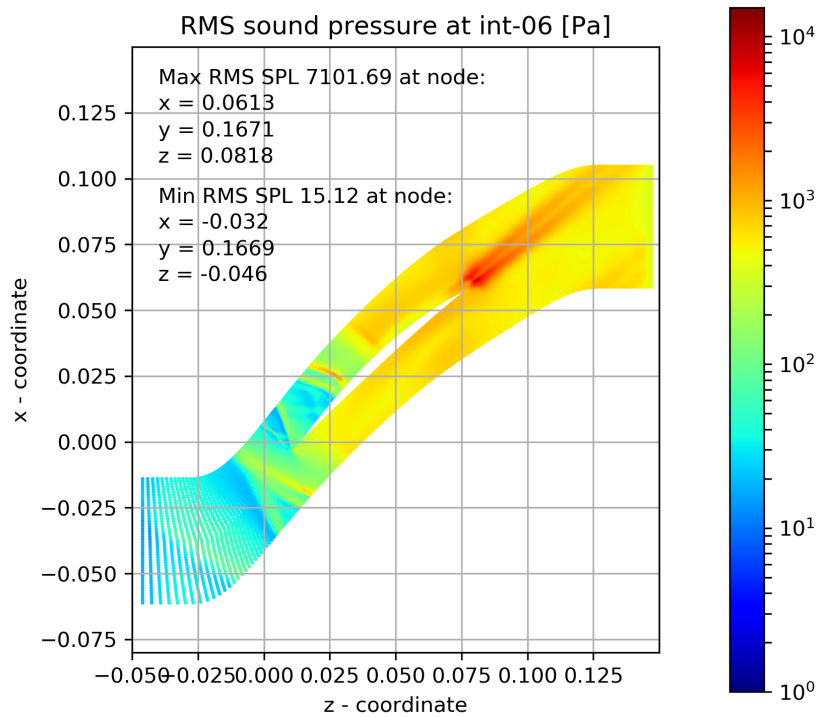


FIGURE A.23: RMS Sound pressure at int-06 mark

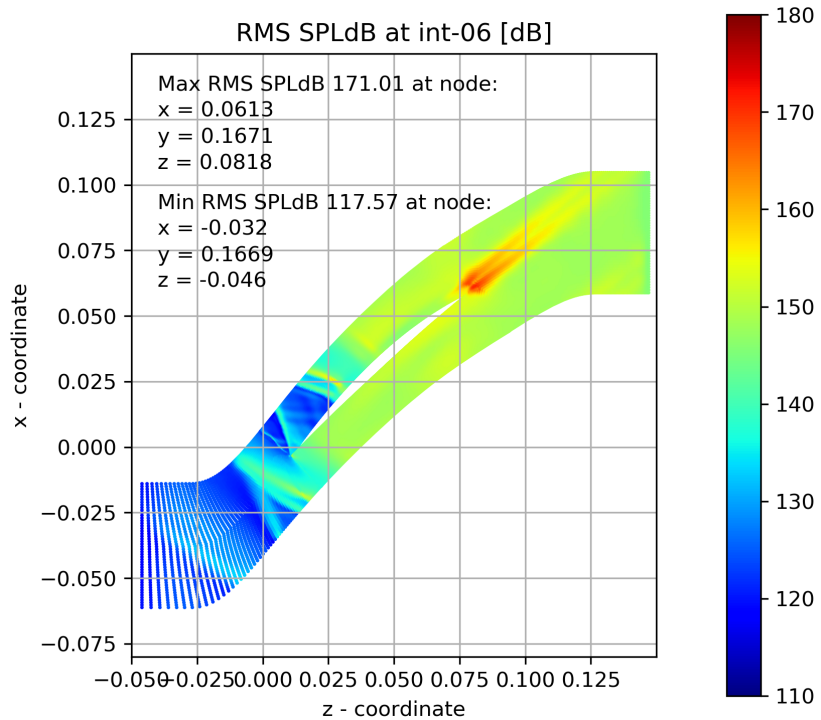


FIGURE A.24: RMS Sound pressure decibel level at int-06 mark

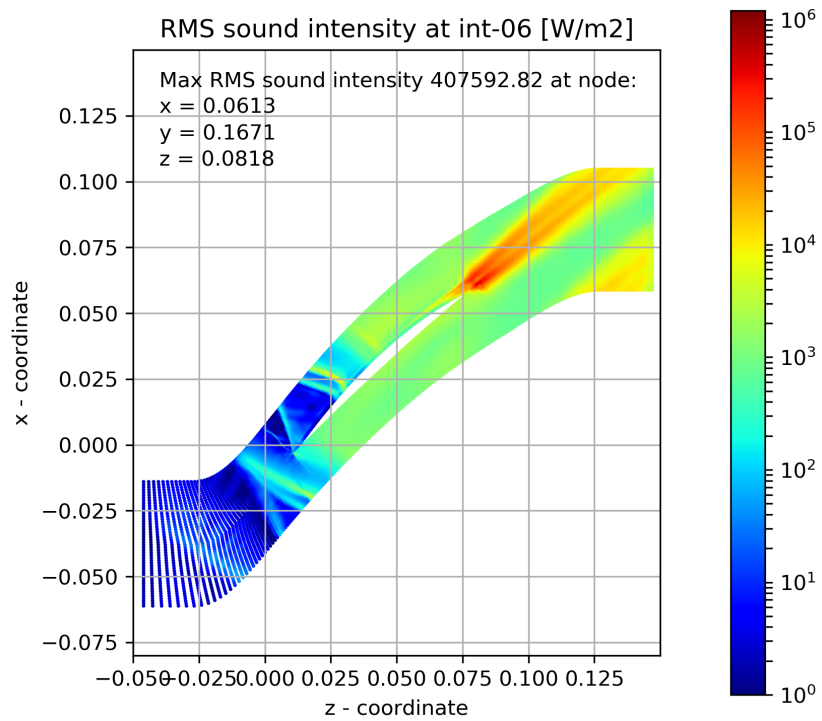


FIGURE A.25: RMS Sound intensity at int-06 mark

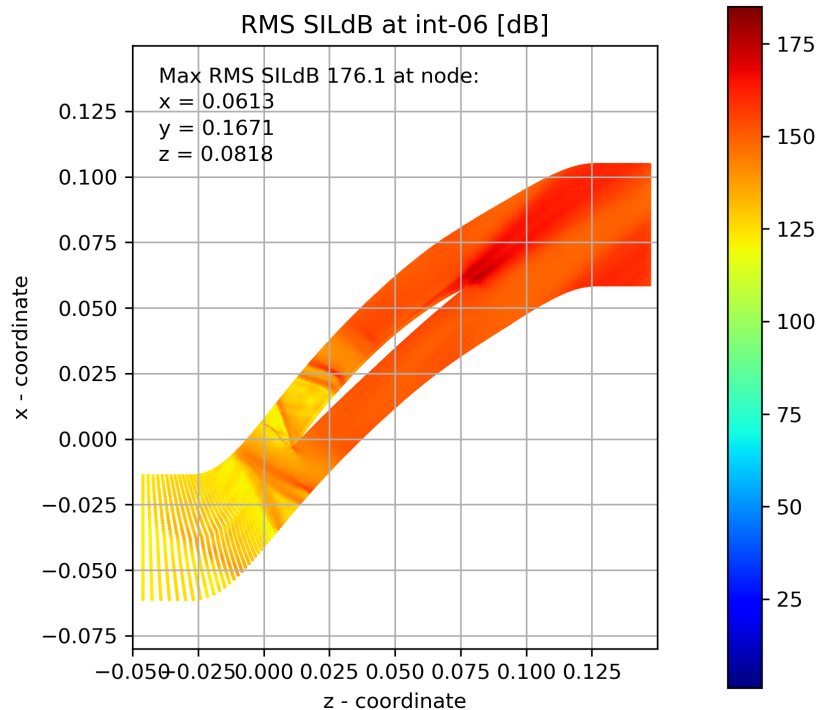


FIGURE A.26: RMS Sound intensity decibel level at int-06 mark

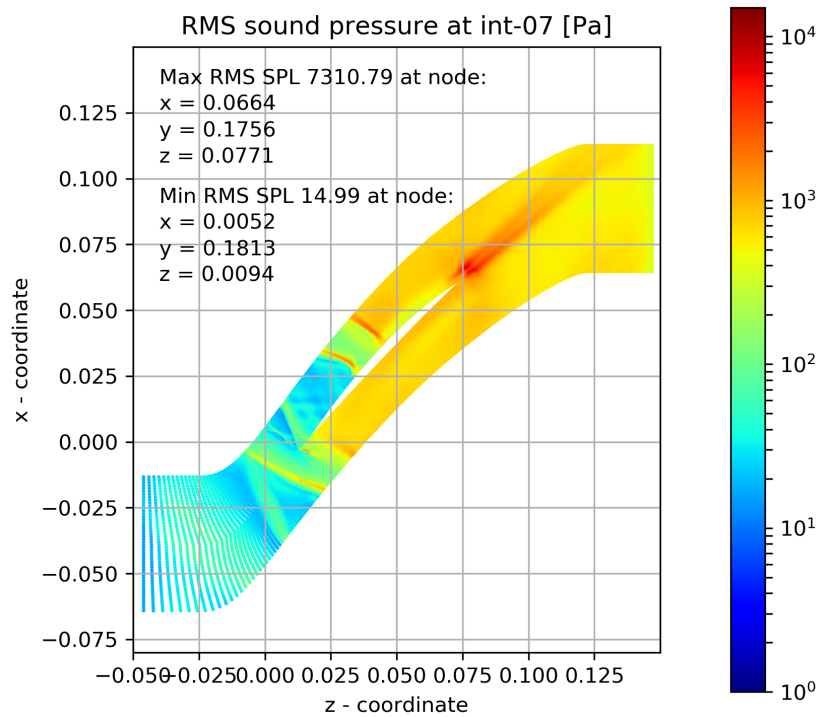


FIGURE A.27: RMS Sound pressure at int-07 mark

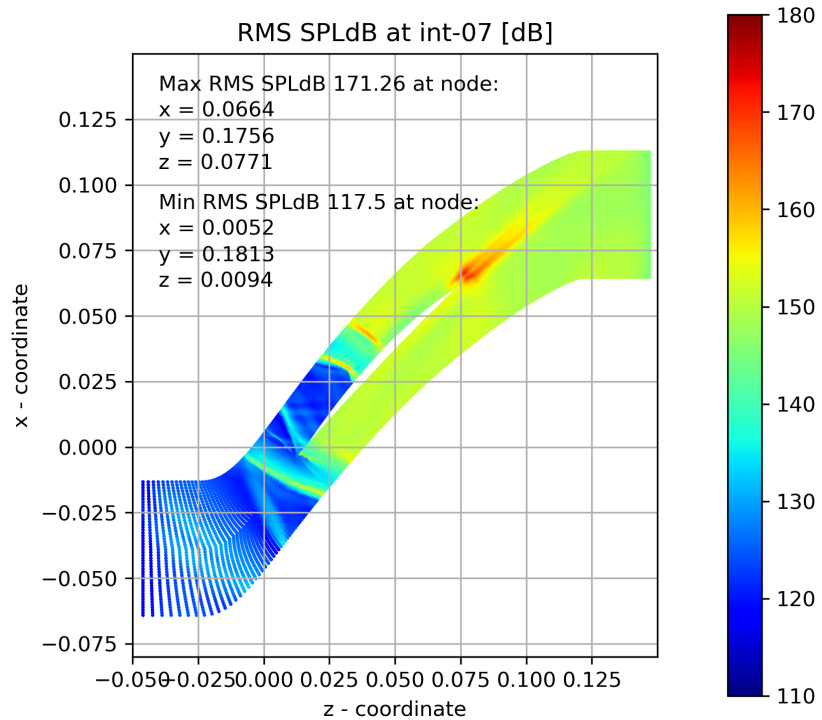


FIGURE A.28: RMS Sound pressure decibel level at int-07 mark

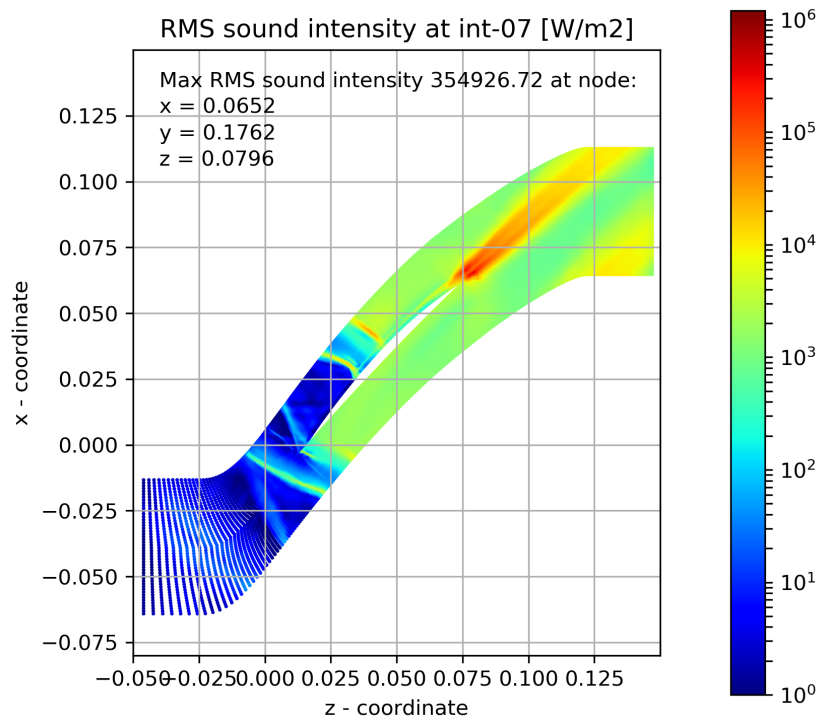


FIGURE A.29: RMS Sound intensity at int-07 mark

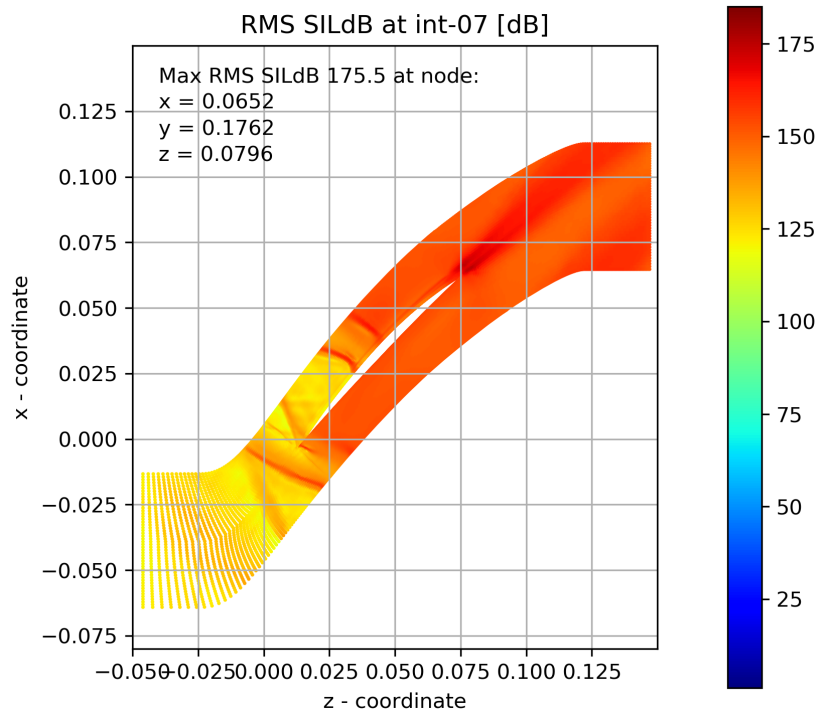


FIGURE A.30: RMS Sound intensity decibel level at int-07 mark

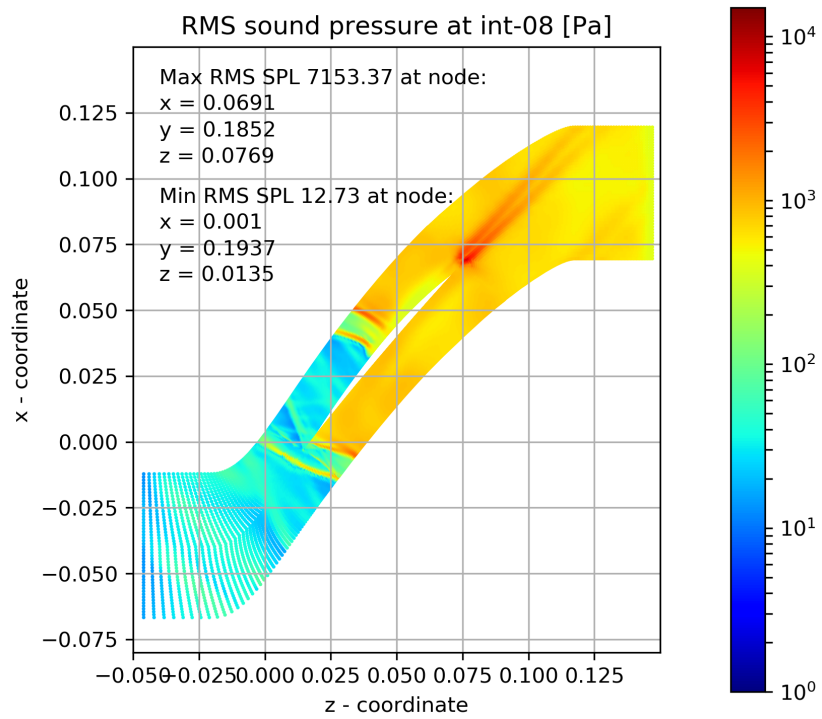


FIGURE A.31: RMS Sound pressure at int-08 mark

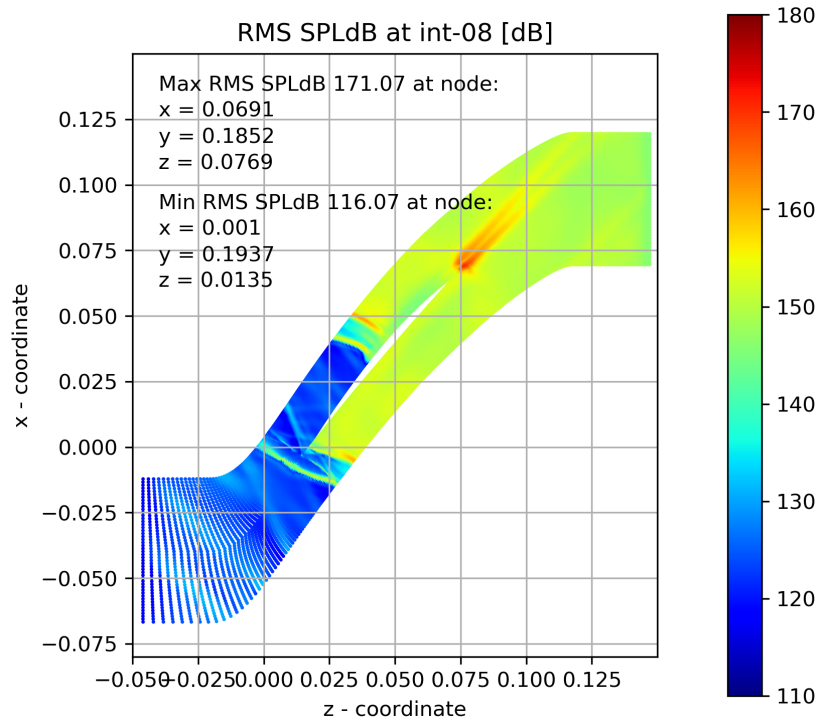


FIGURE A.32: RMS Sound pressure decibel level at int-08 mark

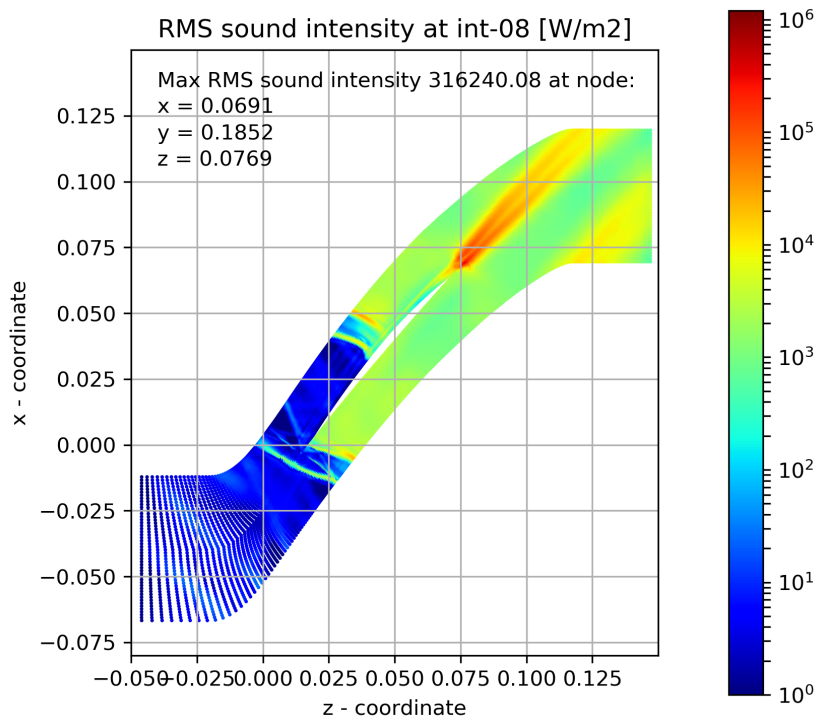


FIGURE A.33: RMS Sound intensity at int-08 mark

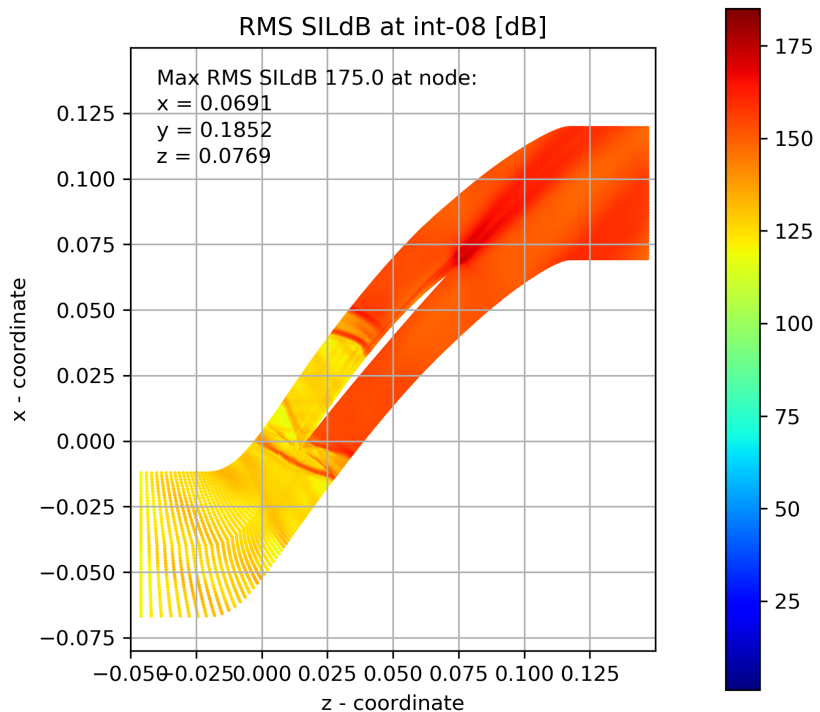


FIGURE A.34: RMS Sound intensity decibel level at int-08 mark

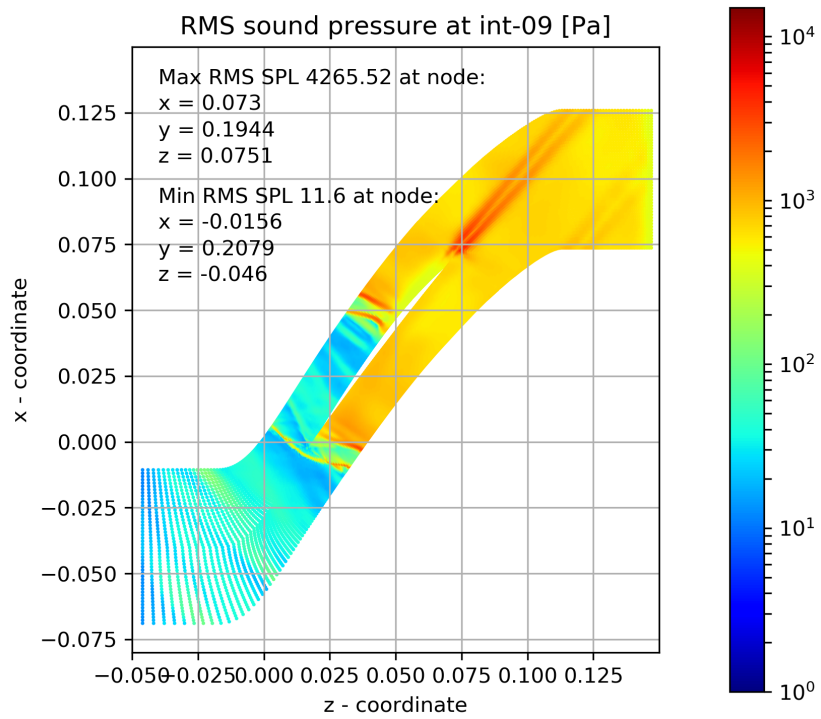


FIGURE A.35: RMS Sound pressure at int-09 mark

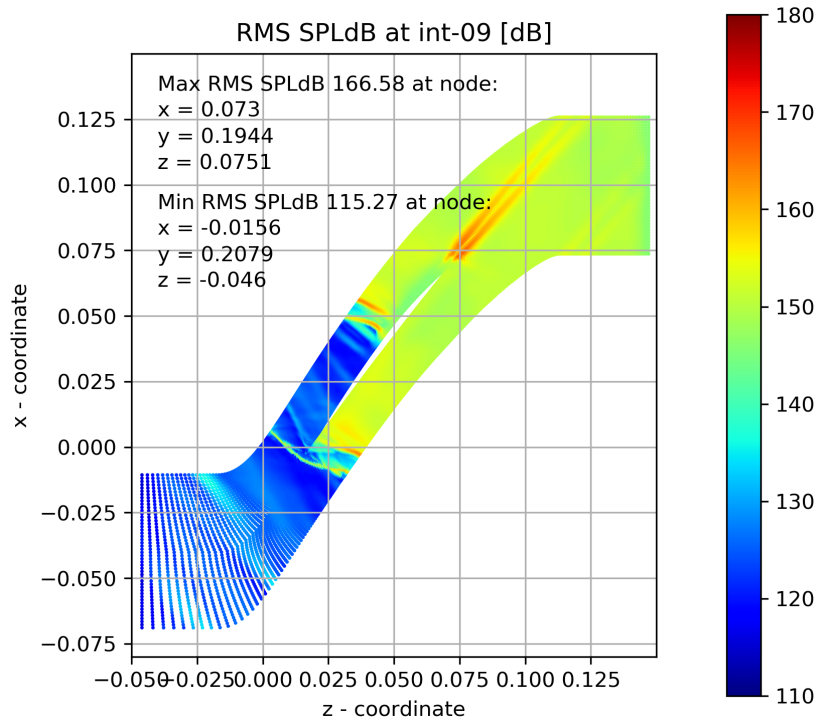


FIGURE A.36: RMS Sound pressure decibel level at int-09 mark

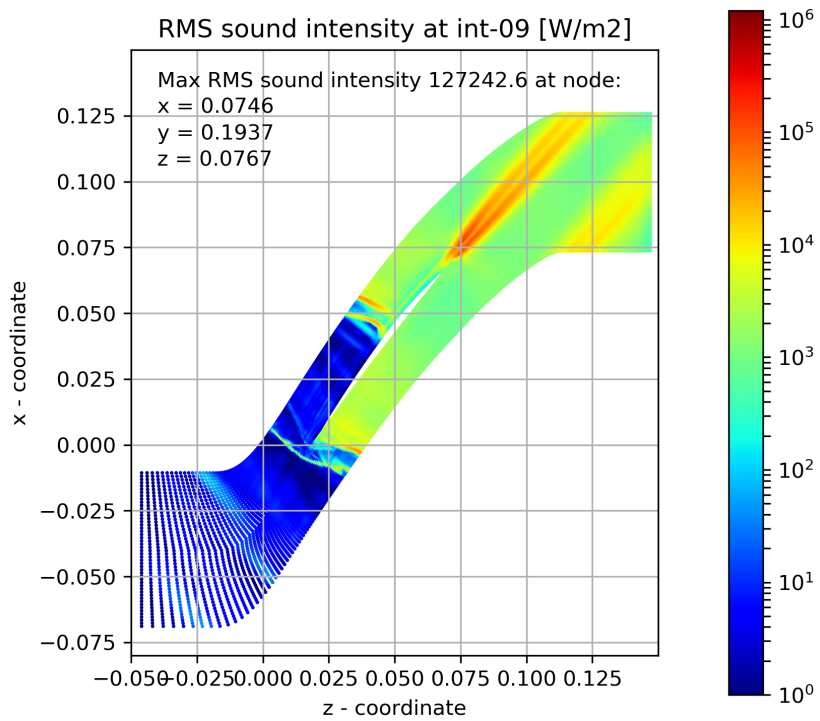


FIGURE A.37: RMS Sound intensity at int-09 mark

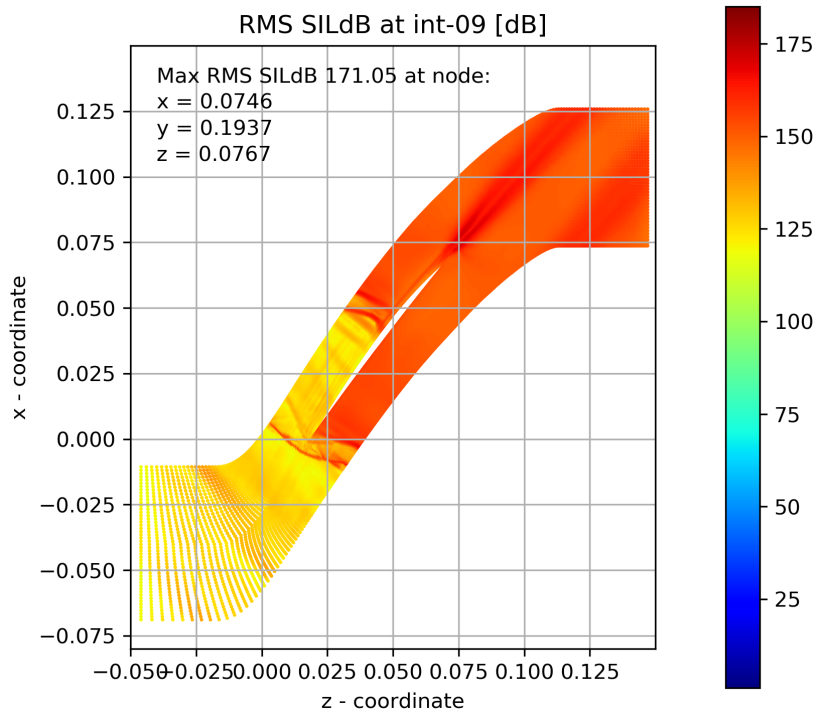


FIGURE A.38: RMS Sound intensity decibel level at int-09 mark

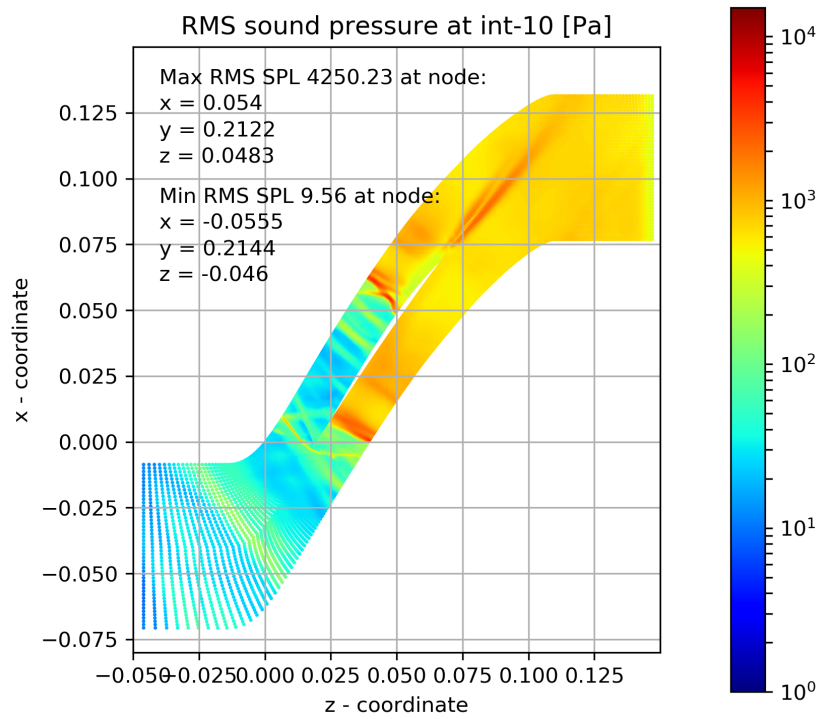


FIGURE A.39: RMS Sound pressure at int-10 mark

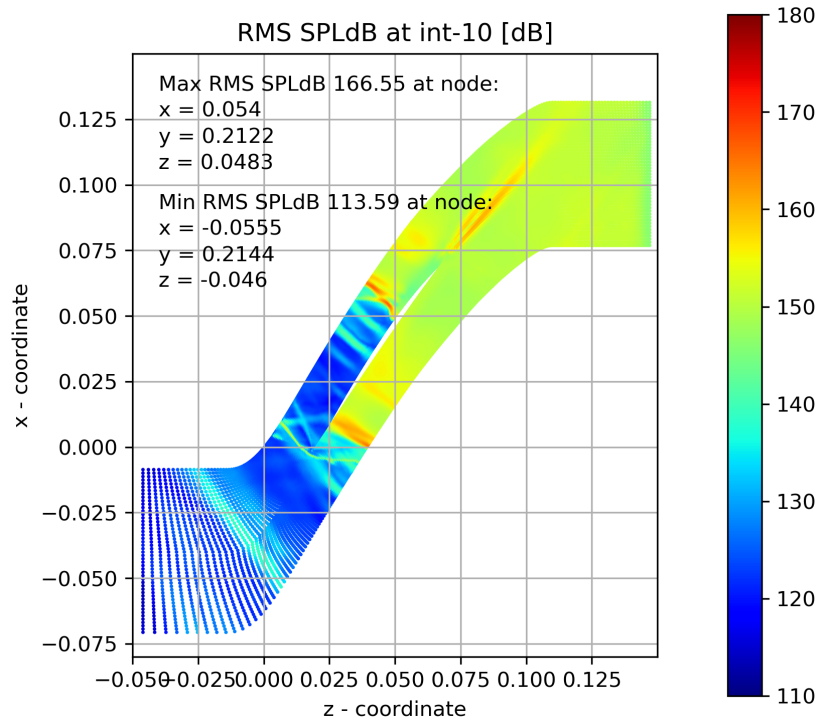


FIGURE A.40: RMS Sound pressure decibel level at int-10 mark

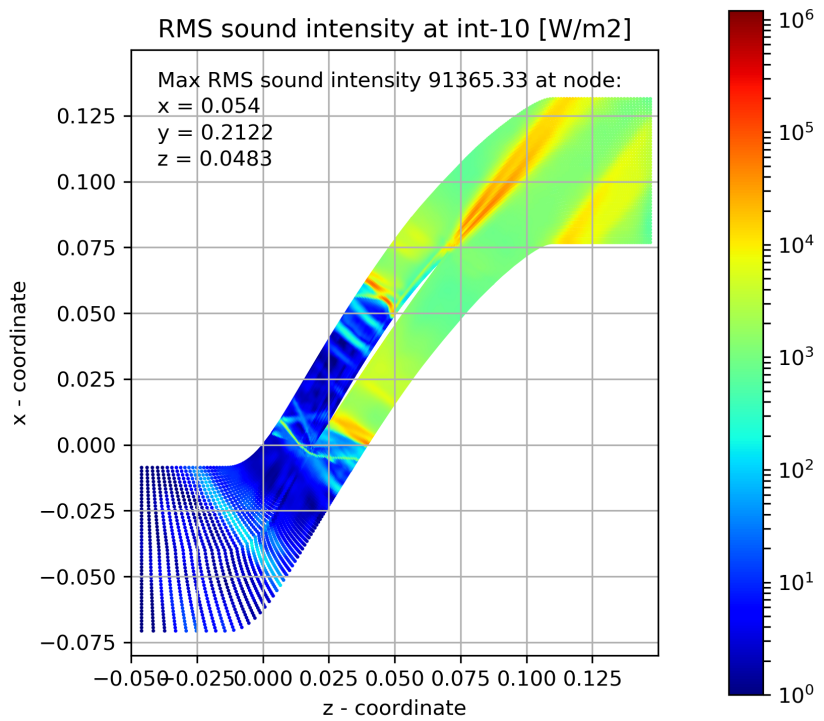


FIGURE A.41: RMS Sound intensity at int-10 mark

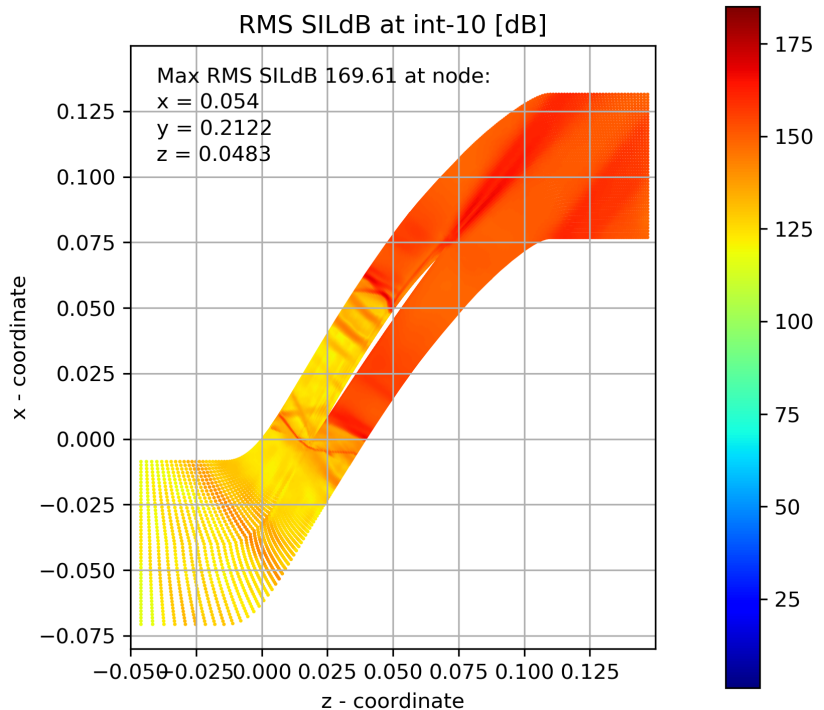


FIGURE A.42: RMS Sound intensity decibel level at int-10 mark

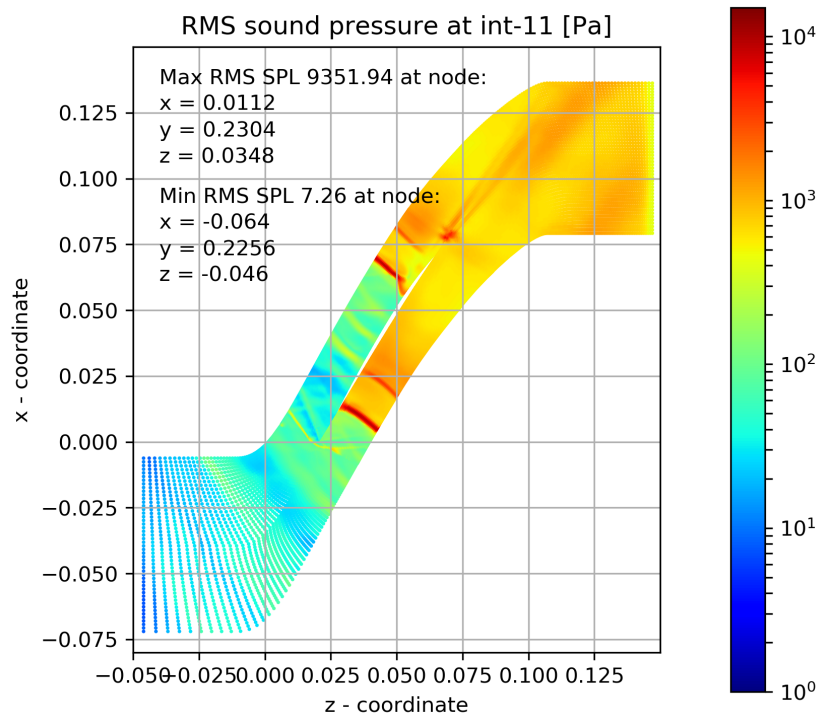


FIGURE A.43: RMS Sound pressure at int-11 mark

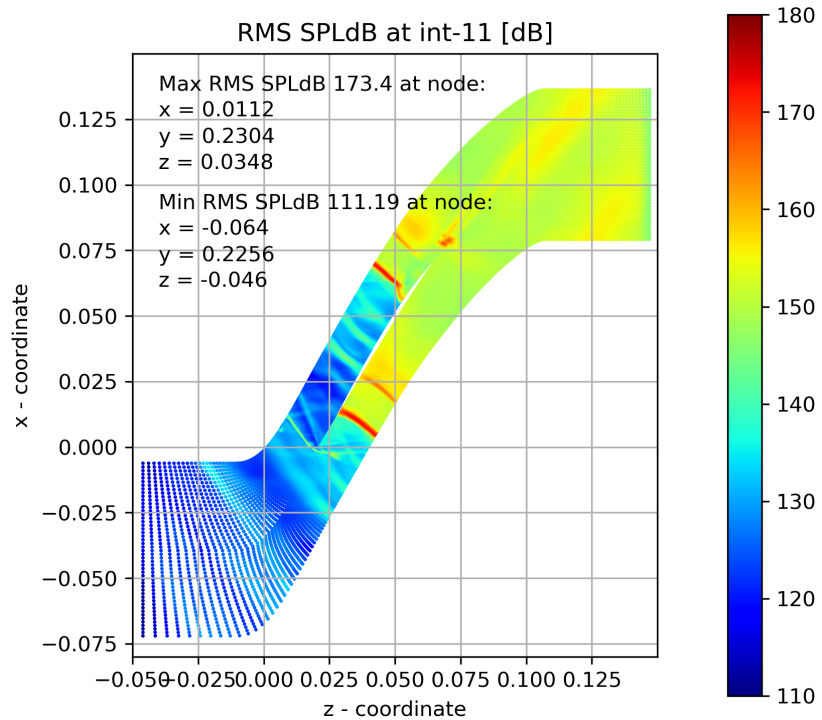


FIGURE A.44: RMS Sound pressure decibel level at int-11 mark

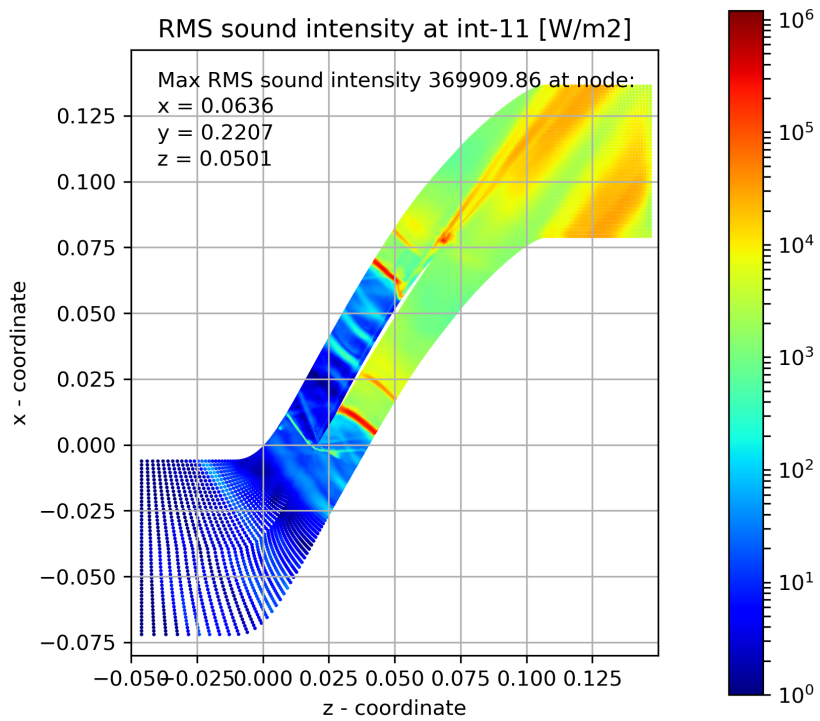


FIGURE A.45: RMS Sound intensity at int-11 mark

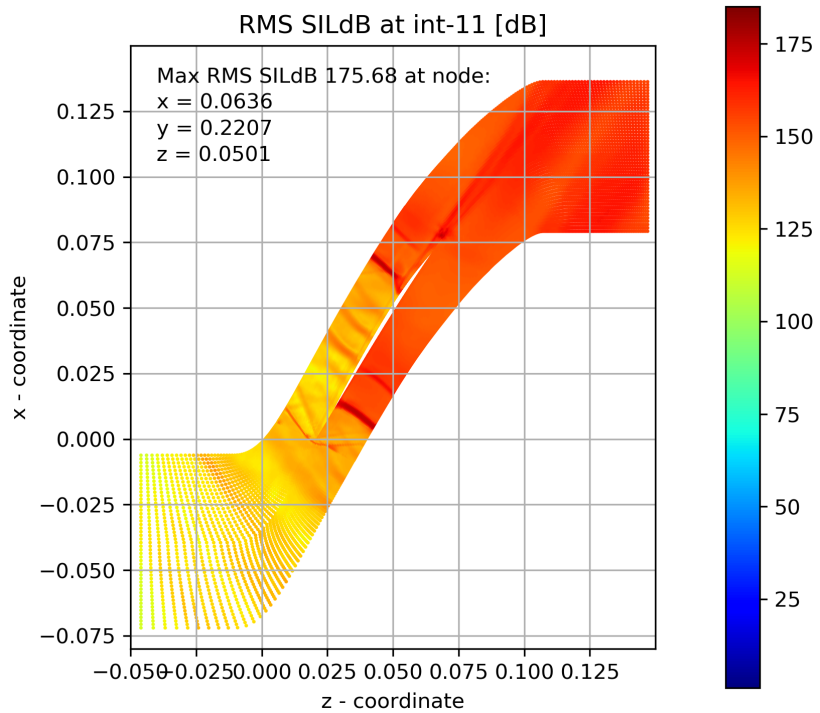


FIGURE A.46: RMS Sound intensity decibel level at int-11 mark

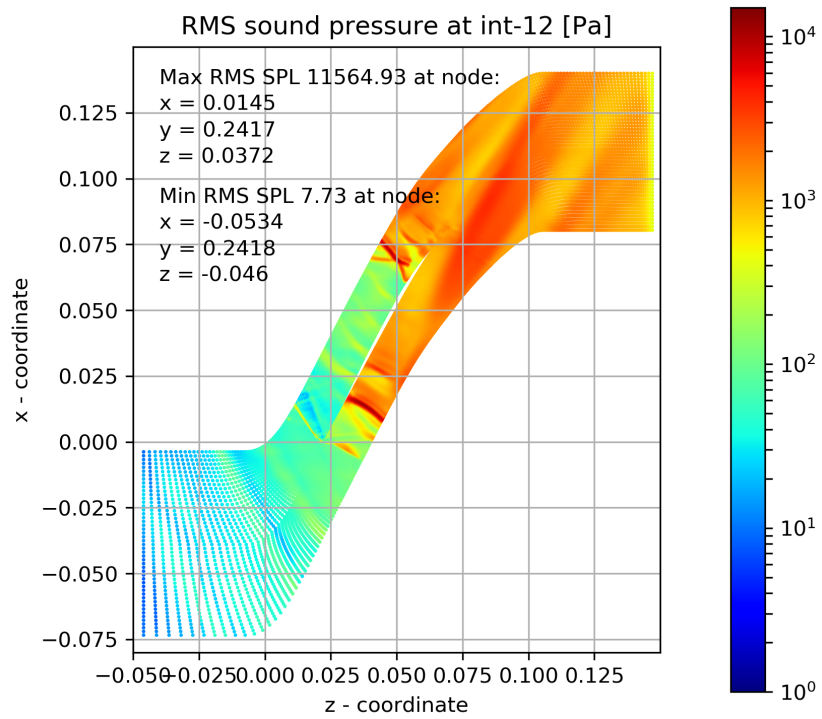


FIGURE A.47: RMS Sound pressure at int-12 mark

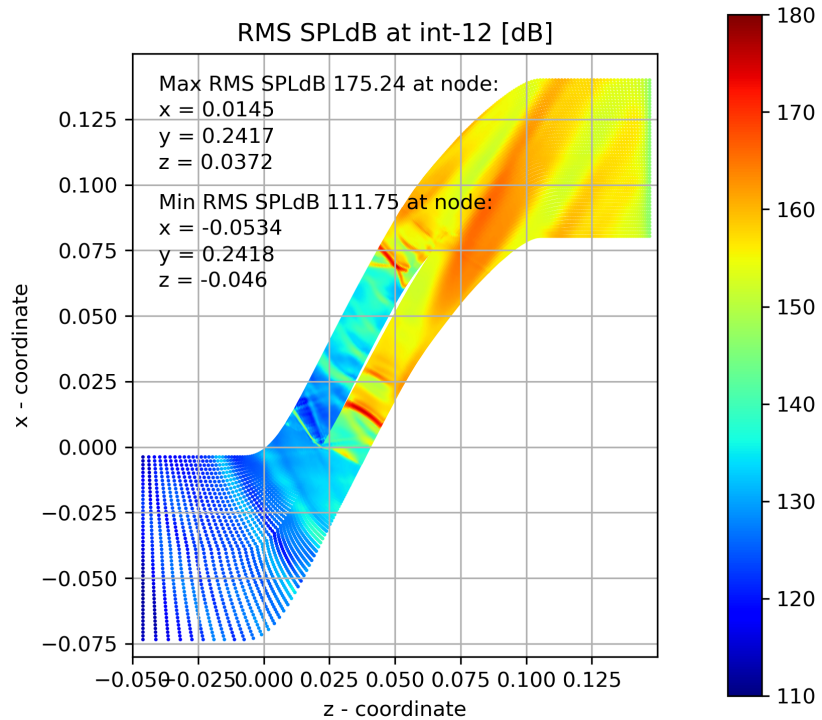


FIGURE A.48: RMS Sound pressure decibel level at int-12 mark

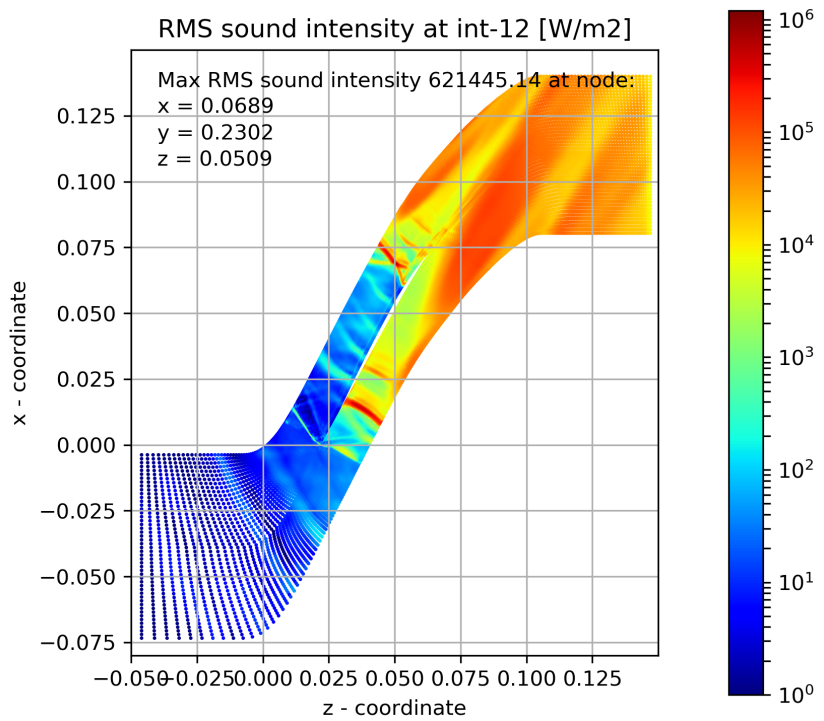


FIGURE A.49: RMS Sound intensity at int-12 mark

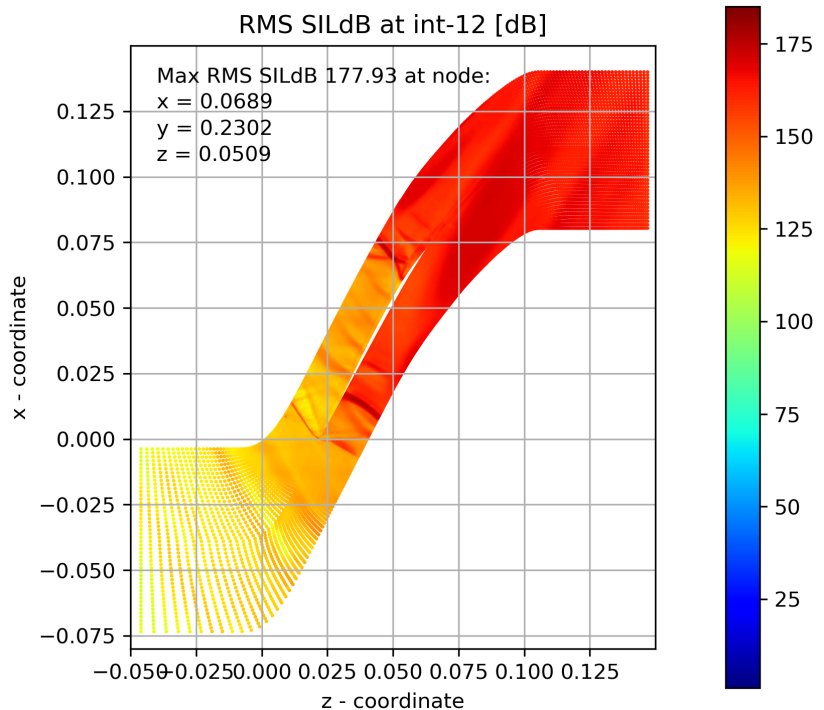


FIGURE A.50: RMS Sound intensity decibel level at int-12 mark

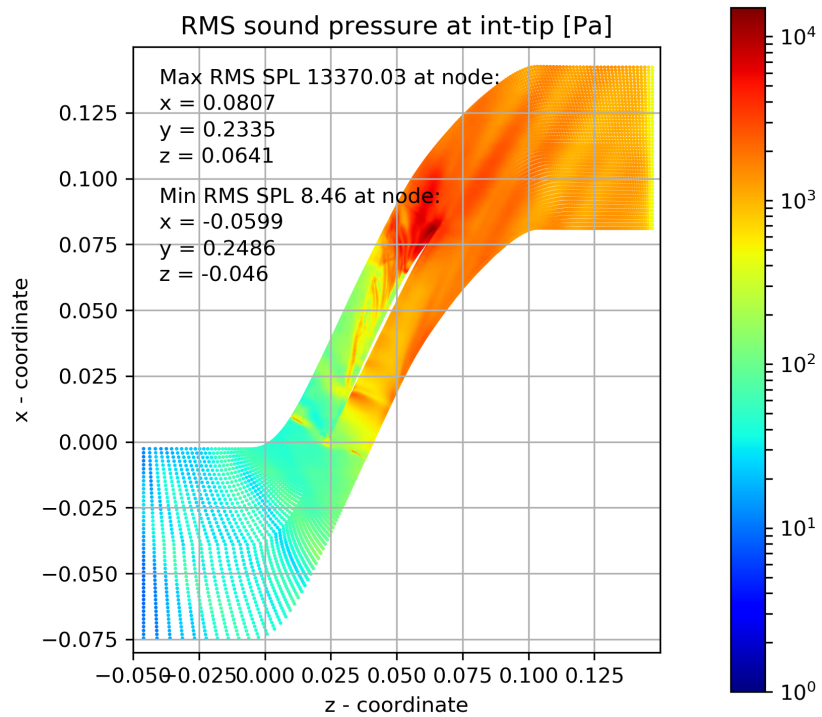


FIGURE A.51: RMS Sound pressure at int-tip mark

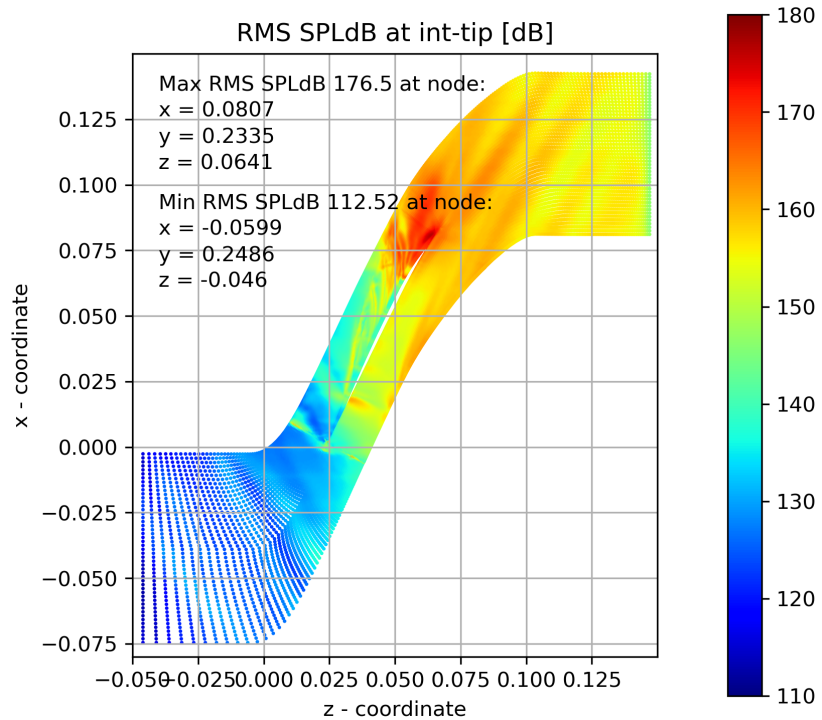


FIGURE A.52: RMS Sound pressure decibel level at int-tip mark

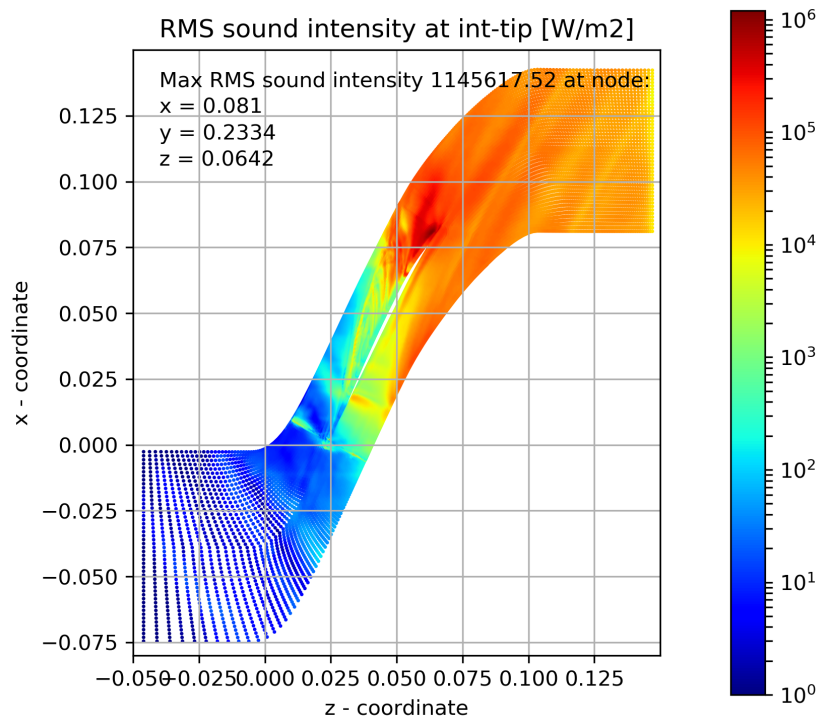


FIGURE A.53: RMS Sound intensity at int-tip mark

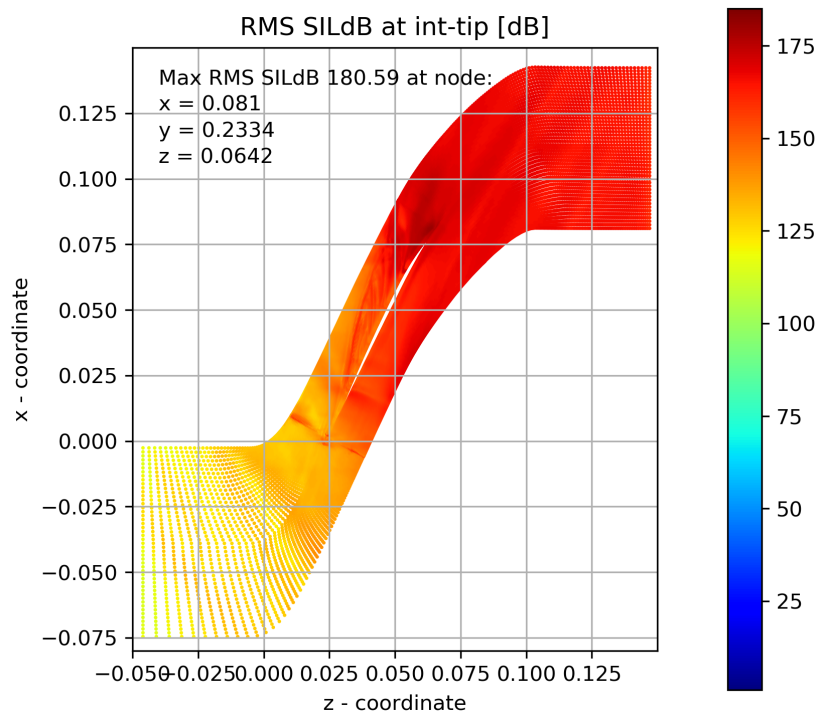


FIGURE A.54: RMS Sound intensity decibel level at int-tip mark

Appendix B

FFT plots

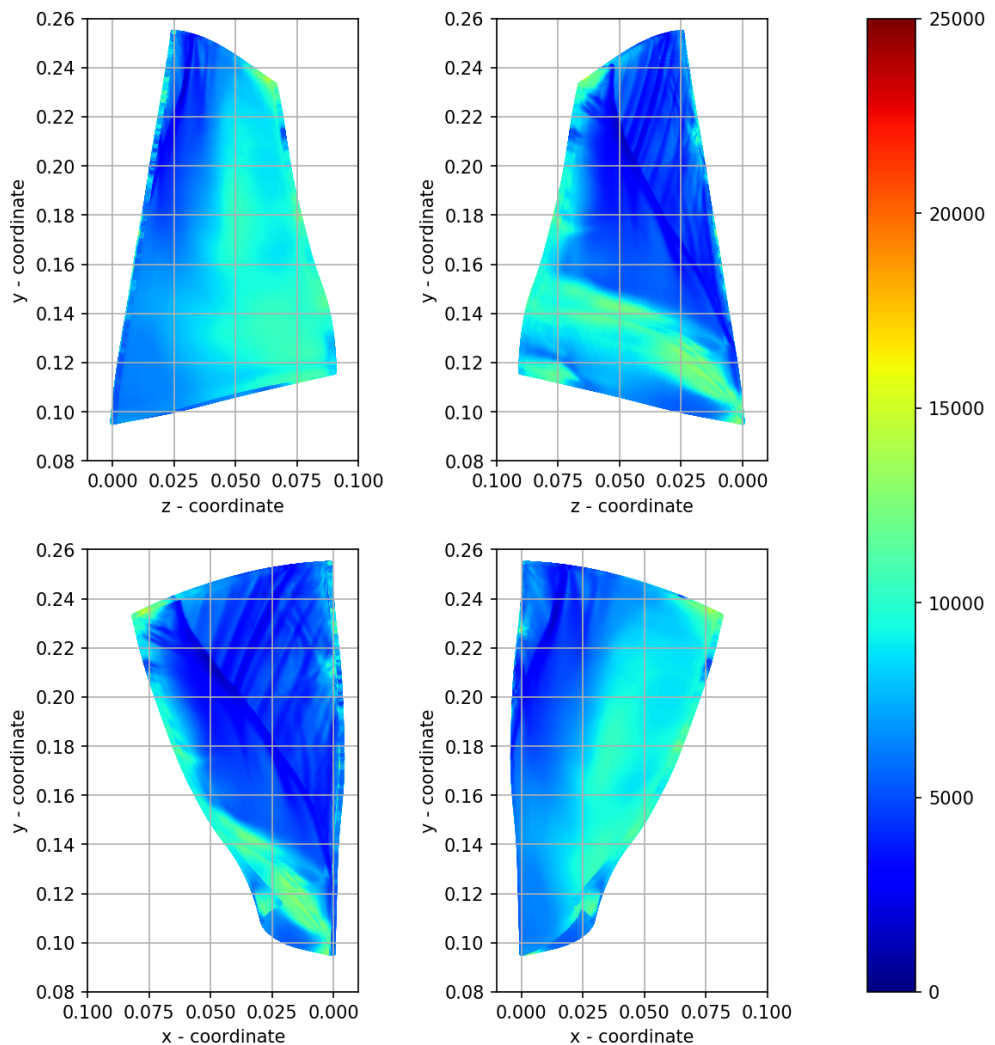


FIGURE B.1: Blade surface amplitude weighted average frequency [dB]

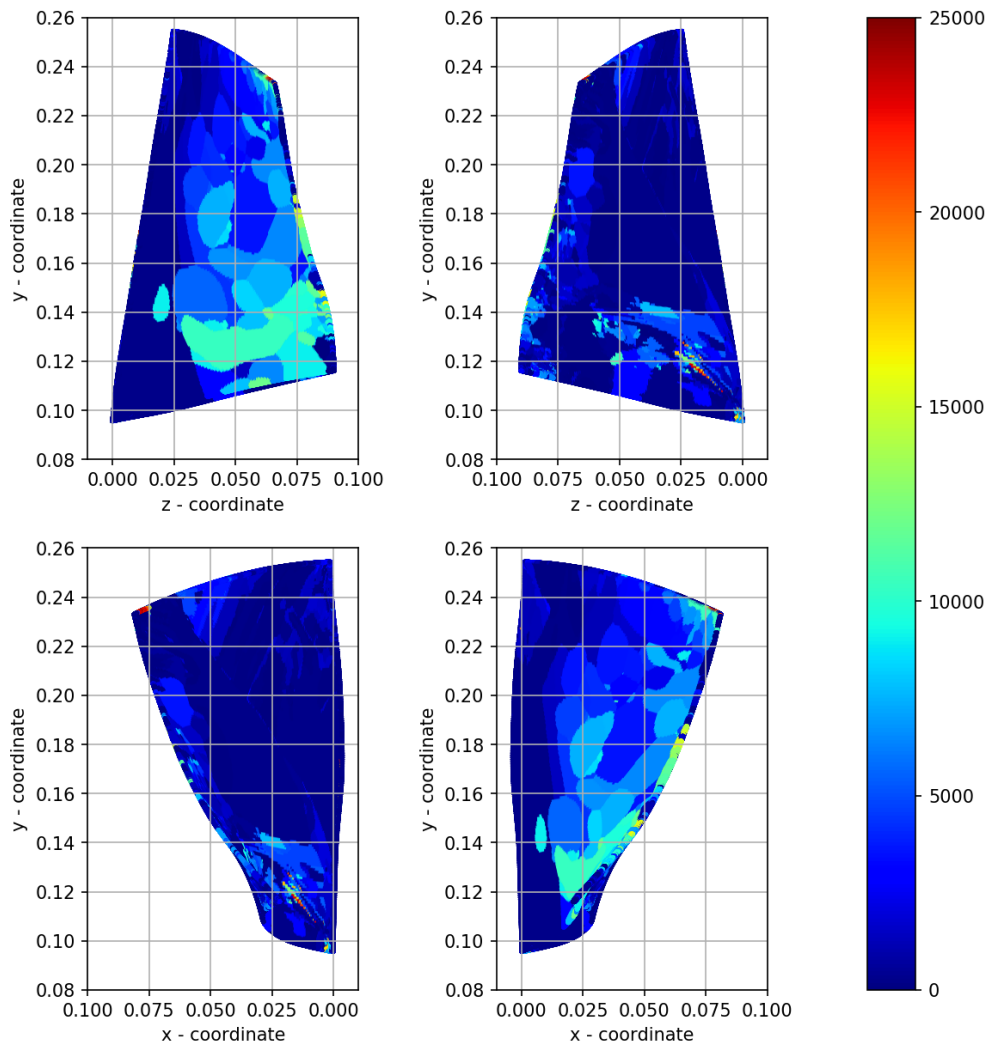


FIGURE B.2: Blade surface frequency of peak amplitude[Hz]

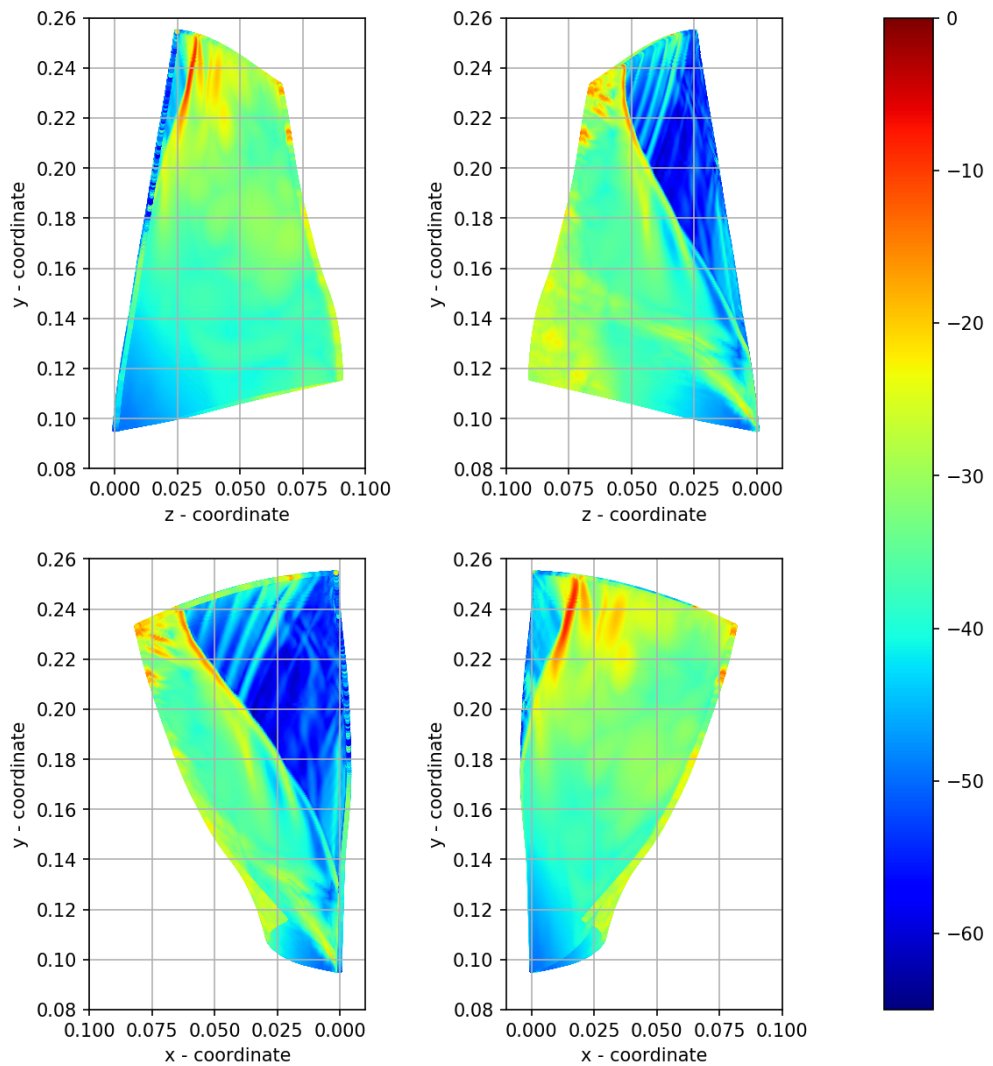


FIGURE B.3: Blade surface peak amplitude [dB]

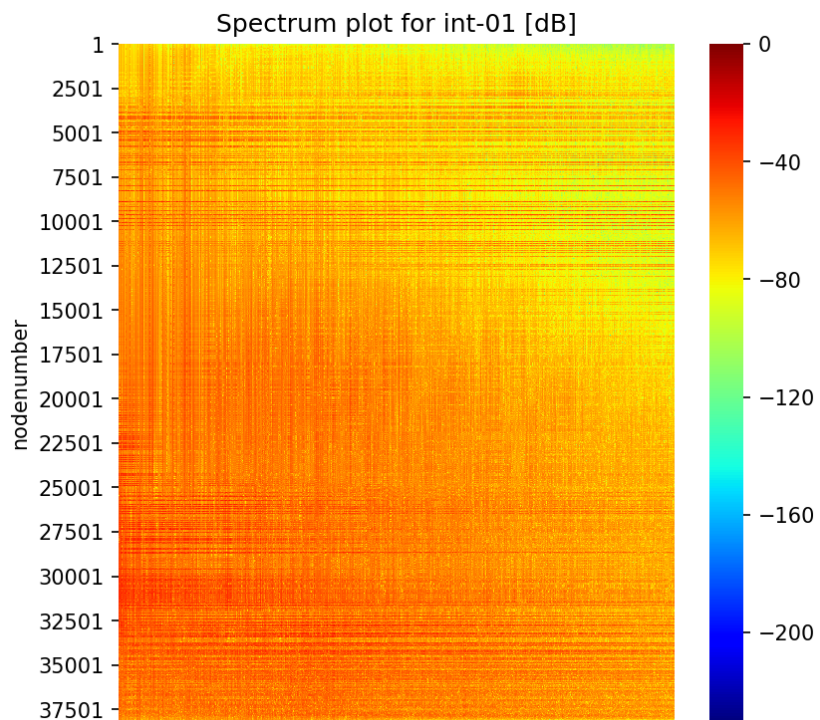


FIGURE B.4: Spectrum plot at int-01 mark

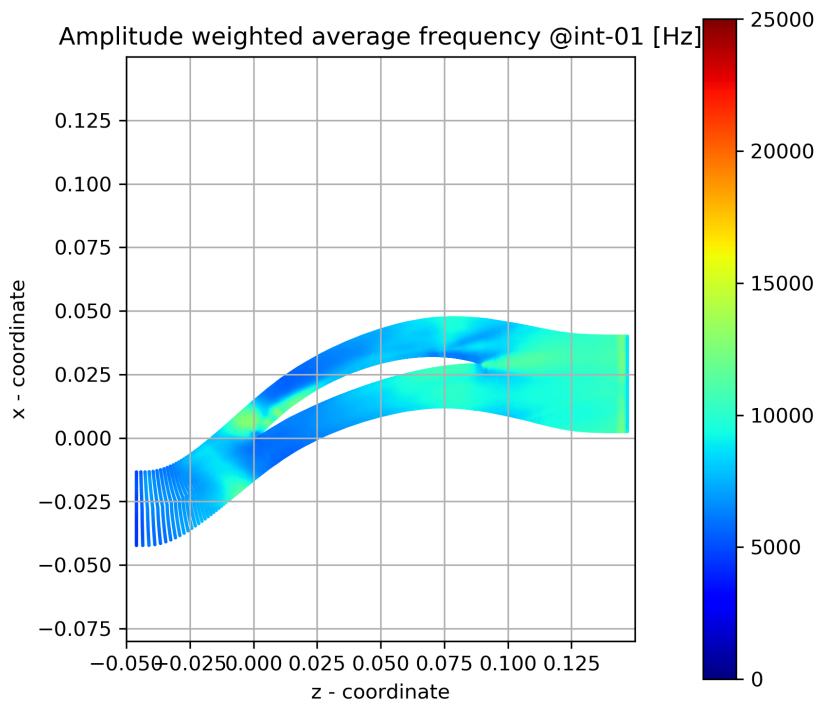


FIGURE B.5: Amplitude weighted average frequency at int-01 mark

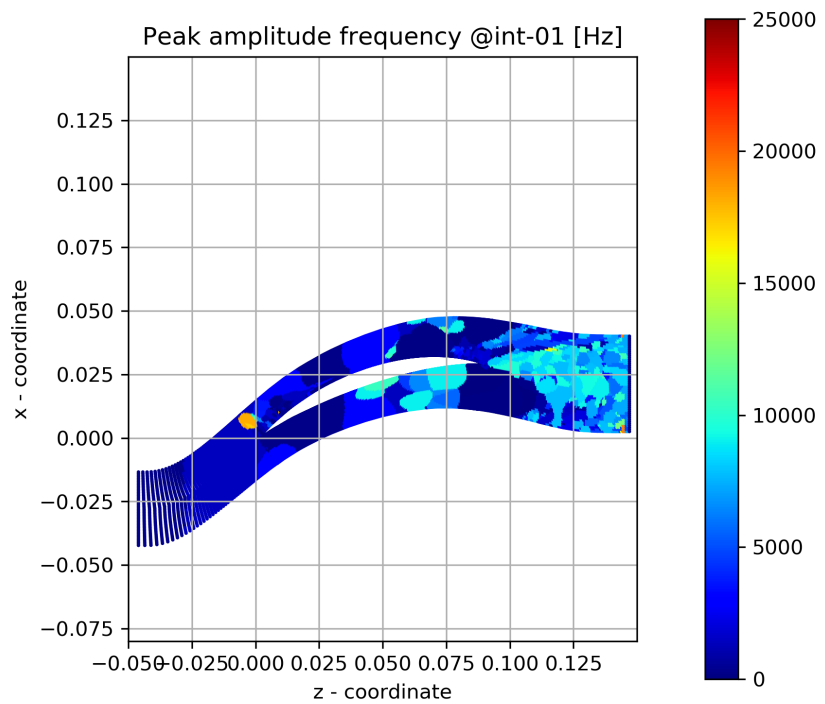


FIGURE B.6: Peak amplitude frequency int-01 mark

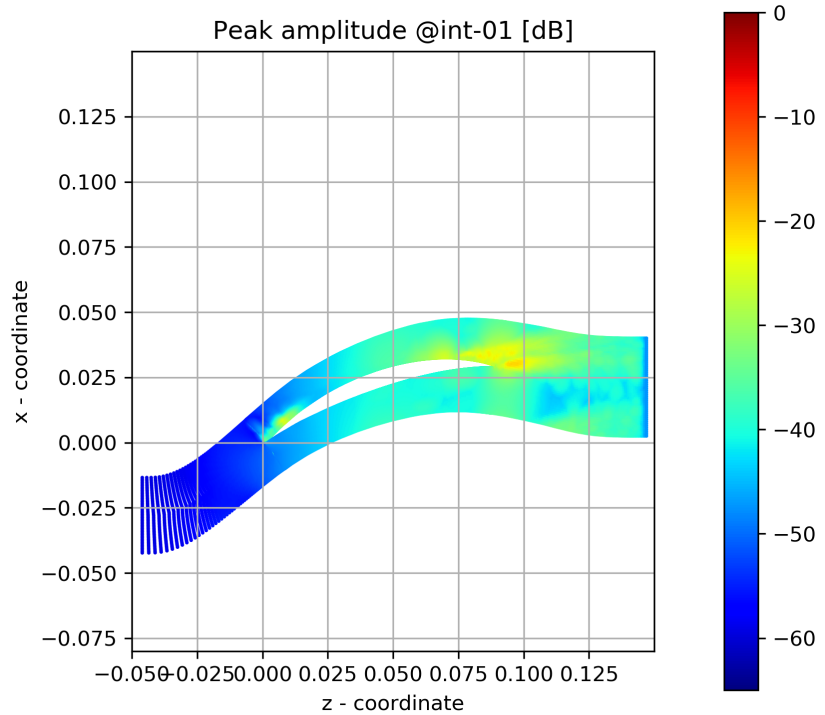


FIGURE B.7: Peak magnitude at int-01 mark

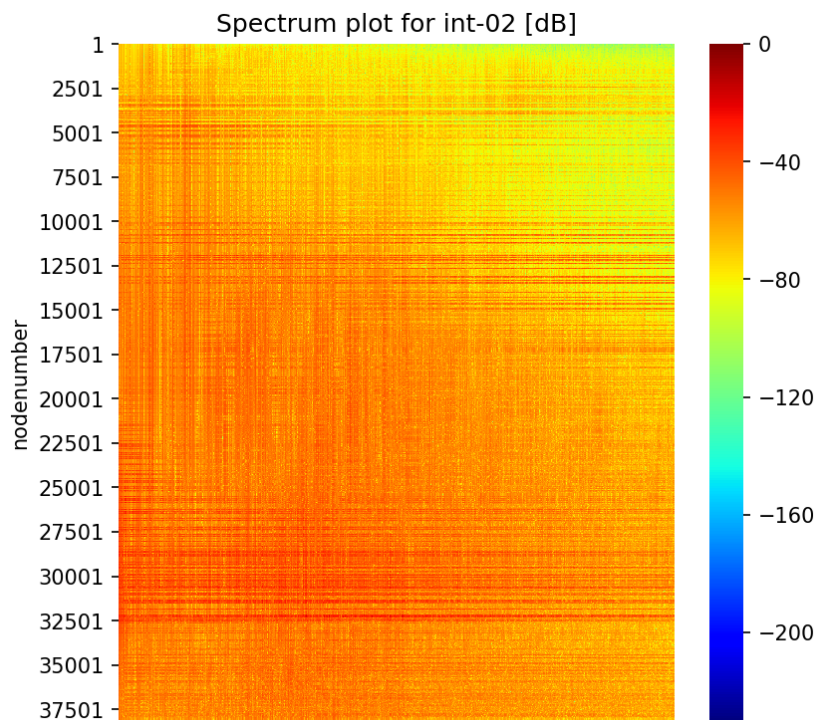


FIGURE B.8: Spectrum plot at int-02 mark

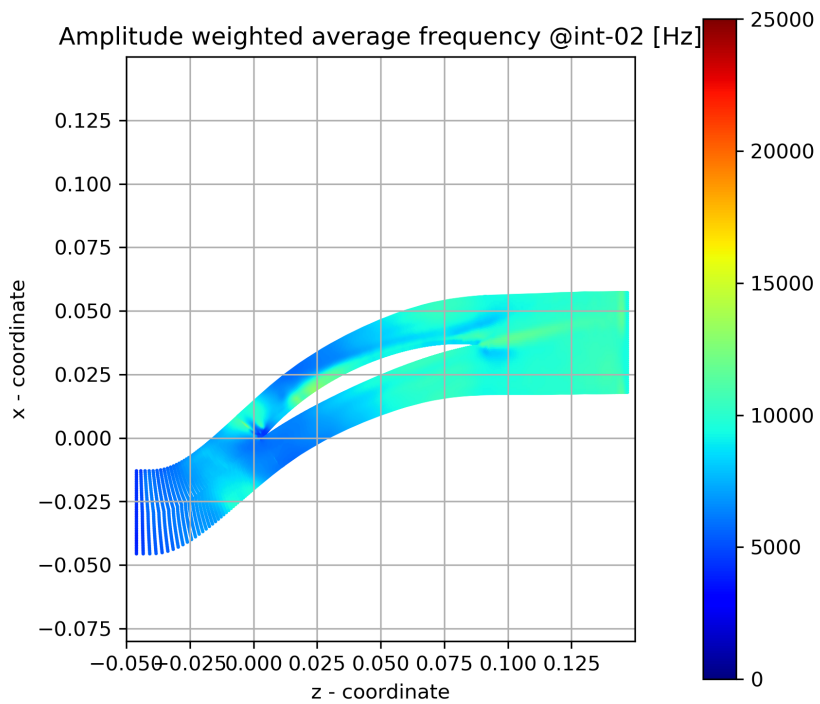


FIGURE B.9: Amplitude weighted average frequency at int-02 mark

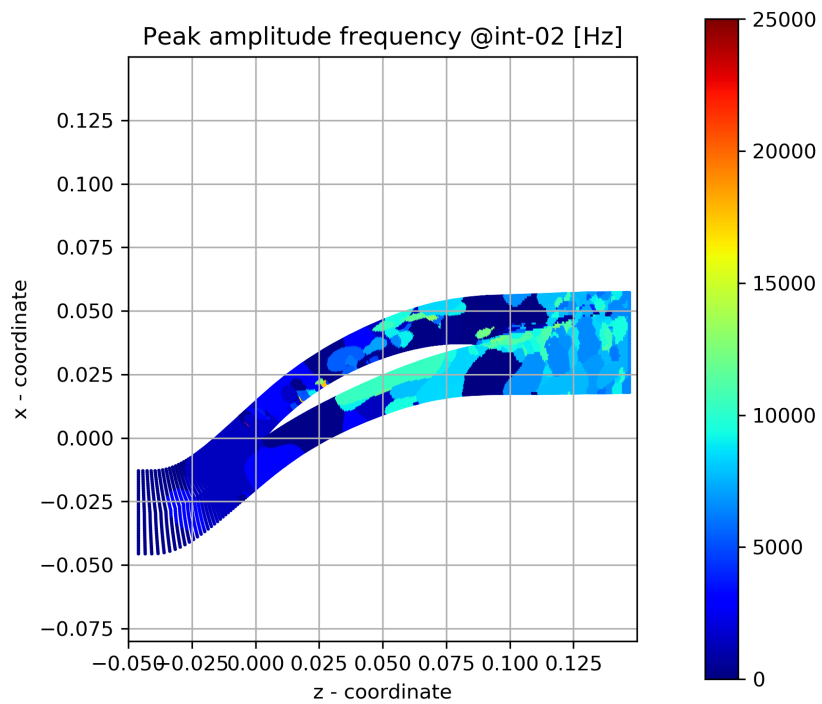


FIGURE B.10: Peak amplitude frequency int-02 mark

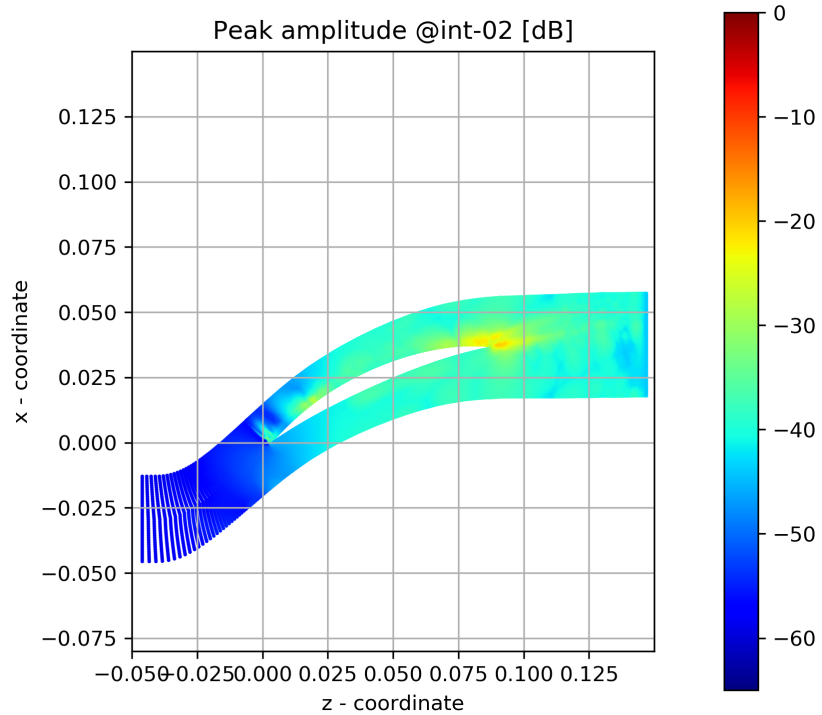


FIGURE B.11: Peak magnitude at int-02 mark

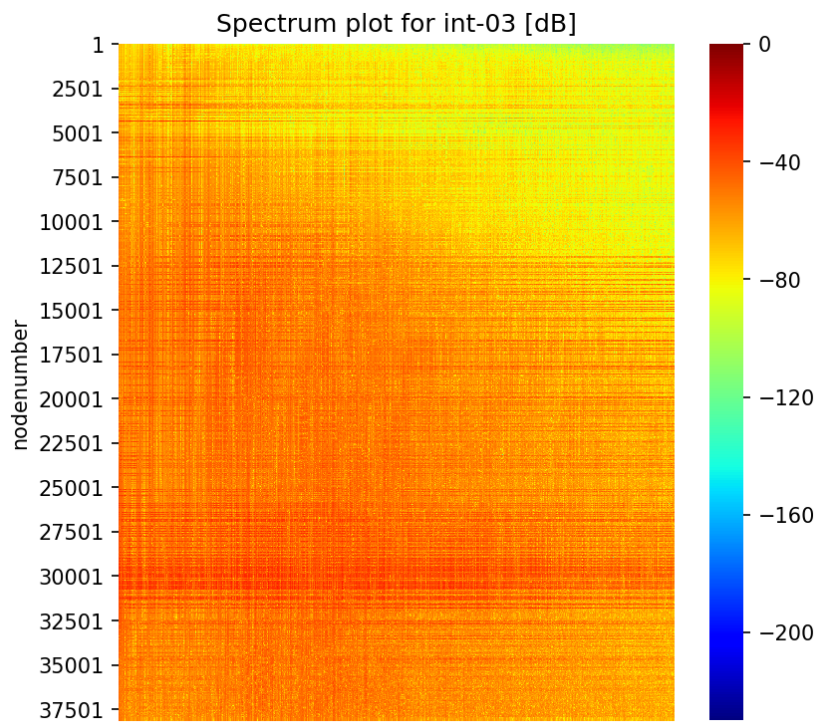


FIGURE B.12: Spectrum plot at int-03 mark

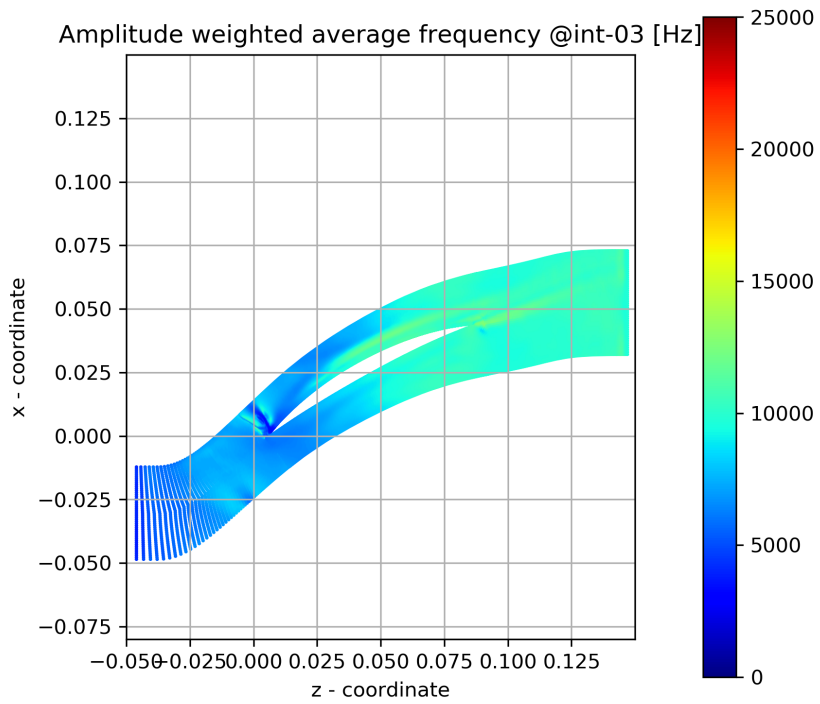


FIGURE B.13: Amplitude weighted average frequency at int-03 mark

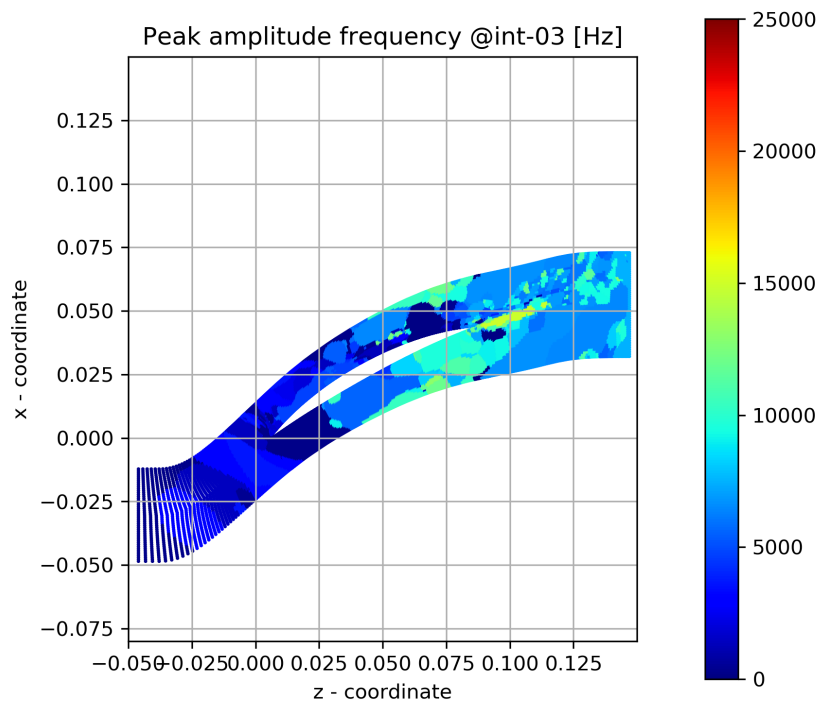


FIGURE B.14: Peak amplitude frequency int-03 mark

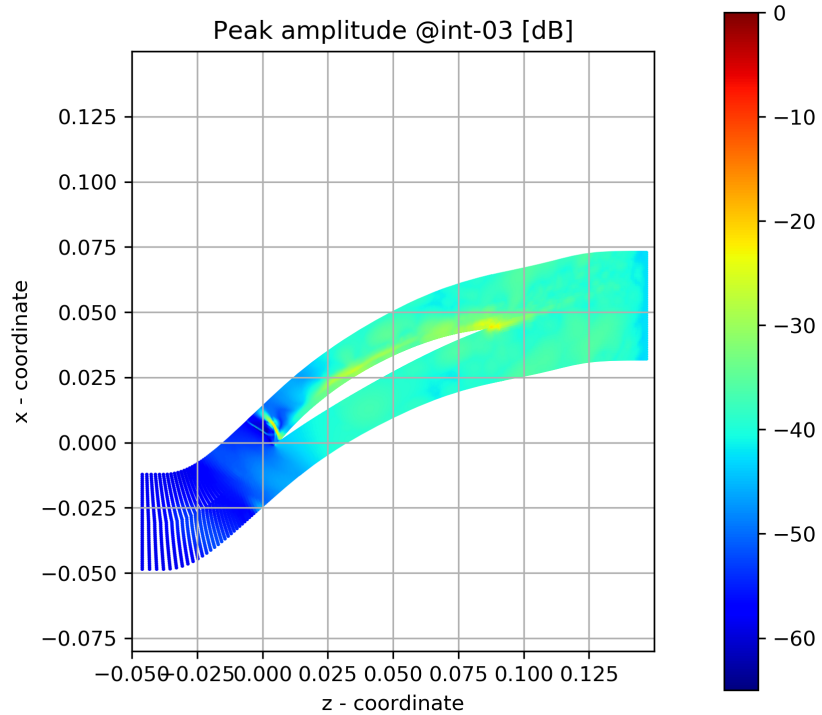


FIGURE B.15: Peak magnitude at int-03 mark

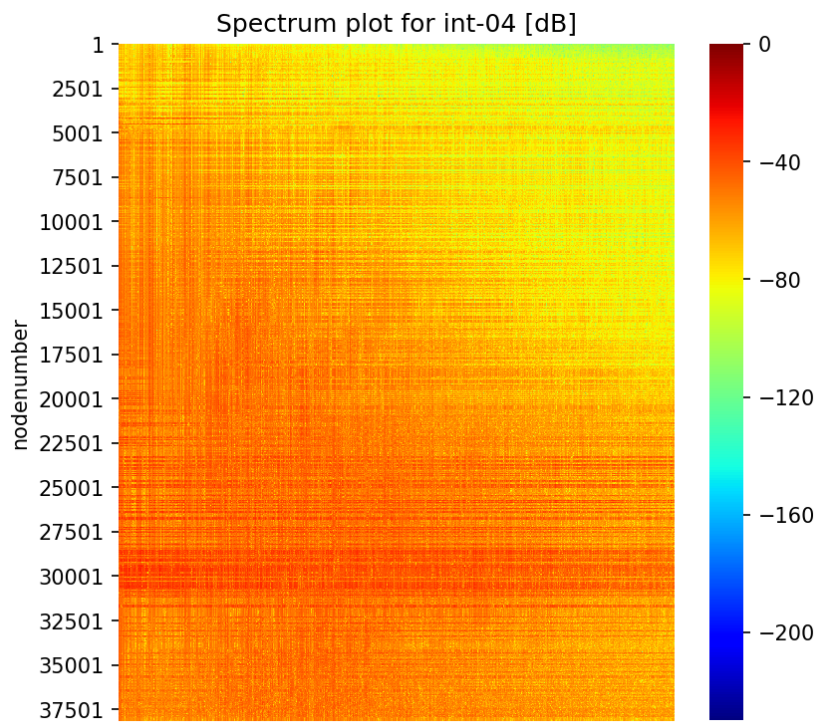


FIGURE B.16: Spectrum plot at int-04 mark

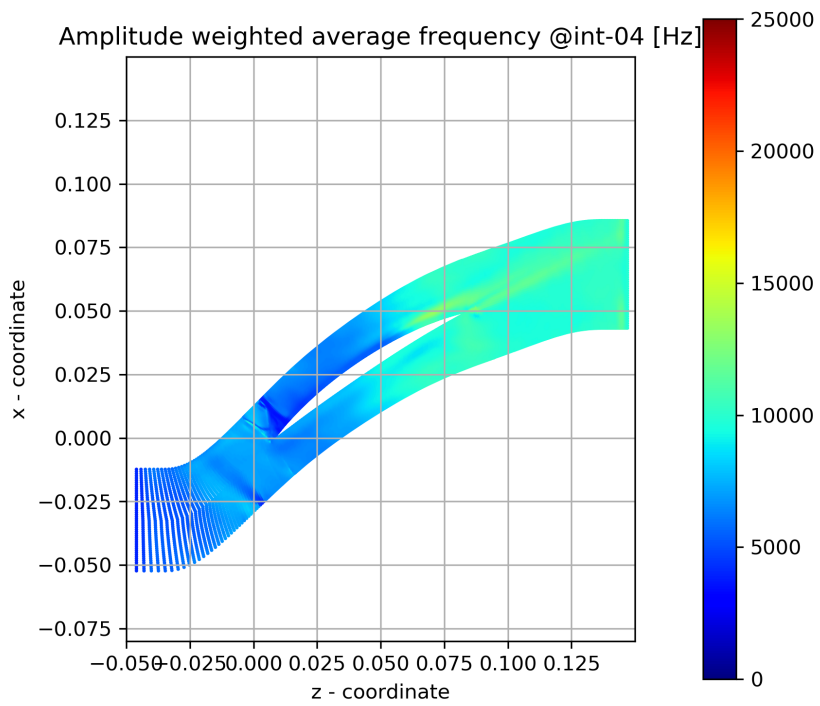


FIGURE B.17: Amplitude weighted average frequency at int-04 mark

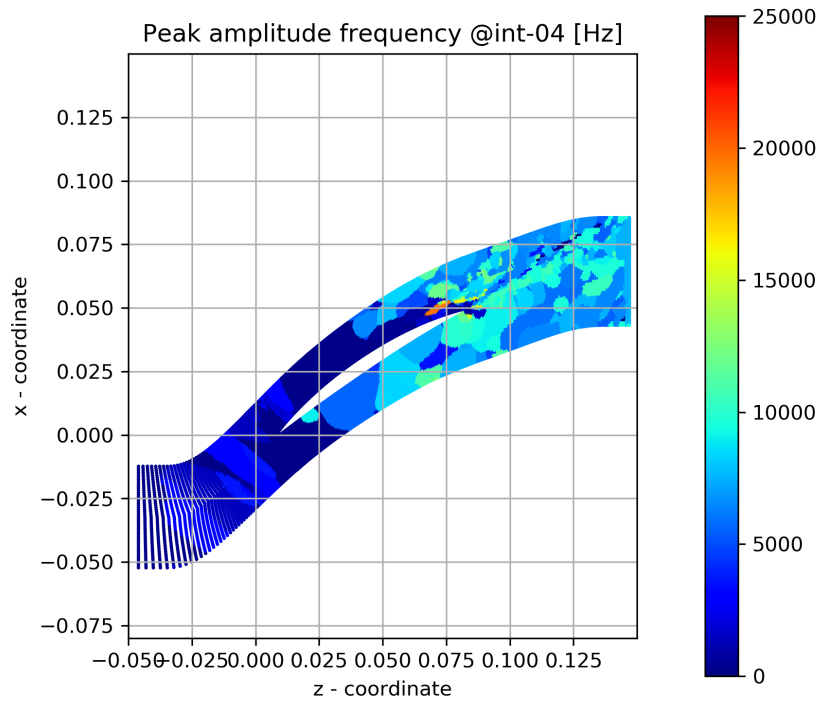


FIGURE B.18: Peak amplitude frequency int-04 mark

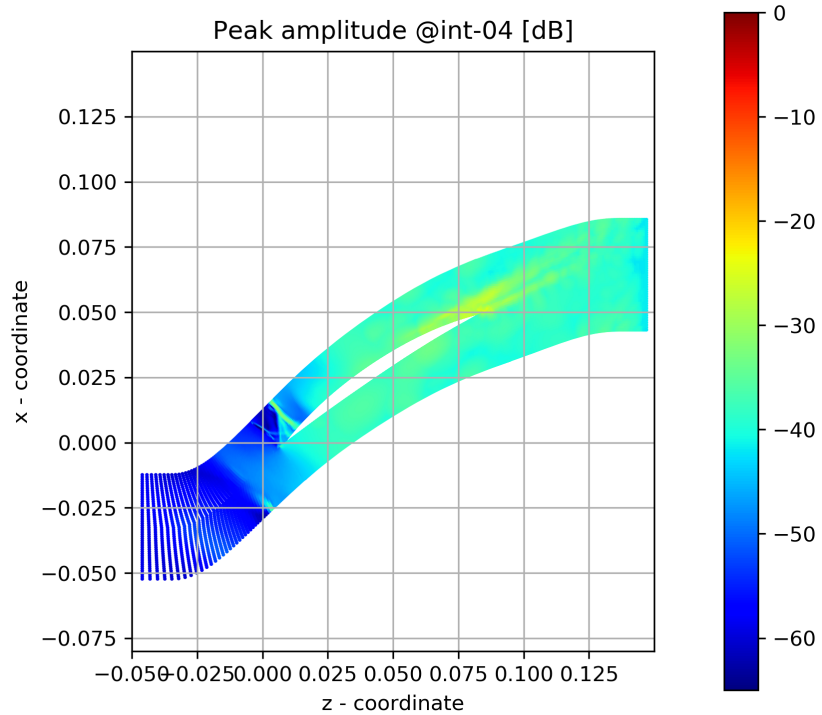


FIGURE B.19: Peak magnitude at int-04 mark

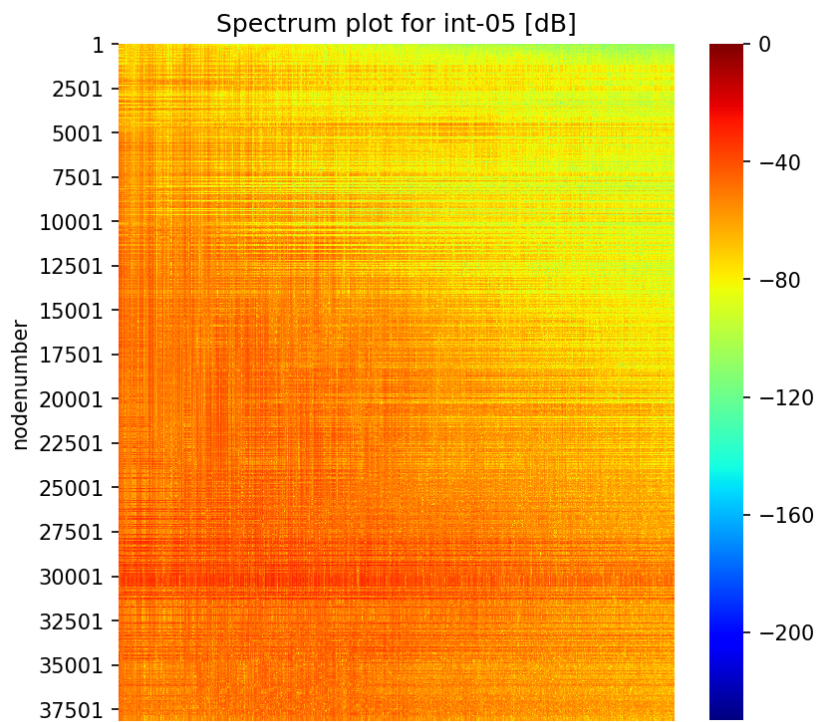


FIGURE B.20: Spectrum plot at int-05 mark

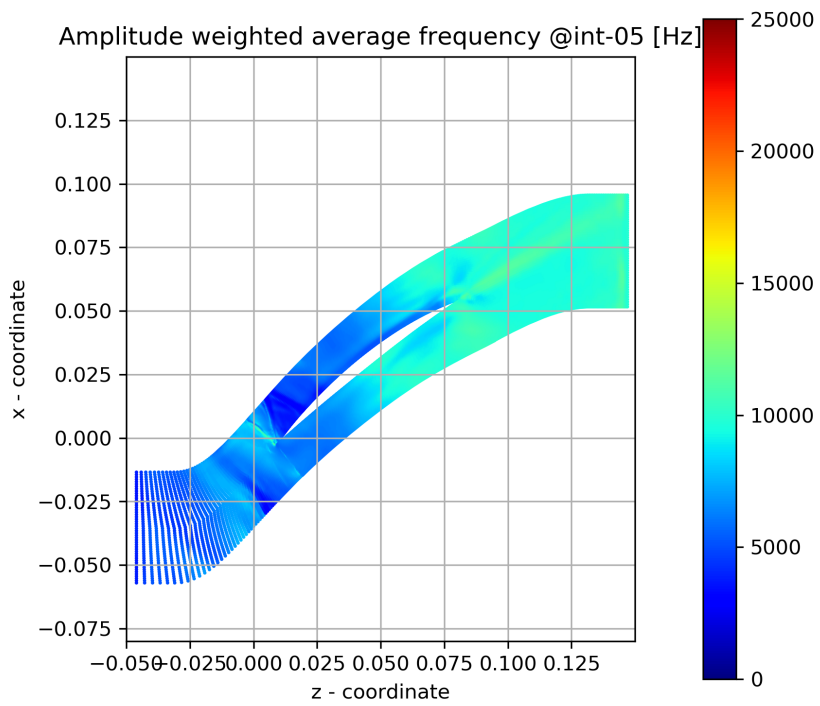


FIGURE B.21: Amplitude weighted average frequency at int-05 mark

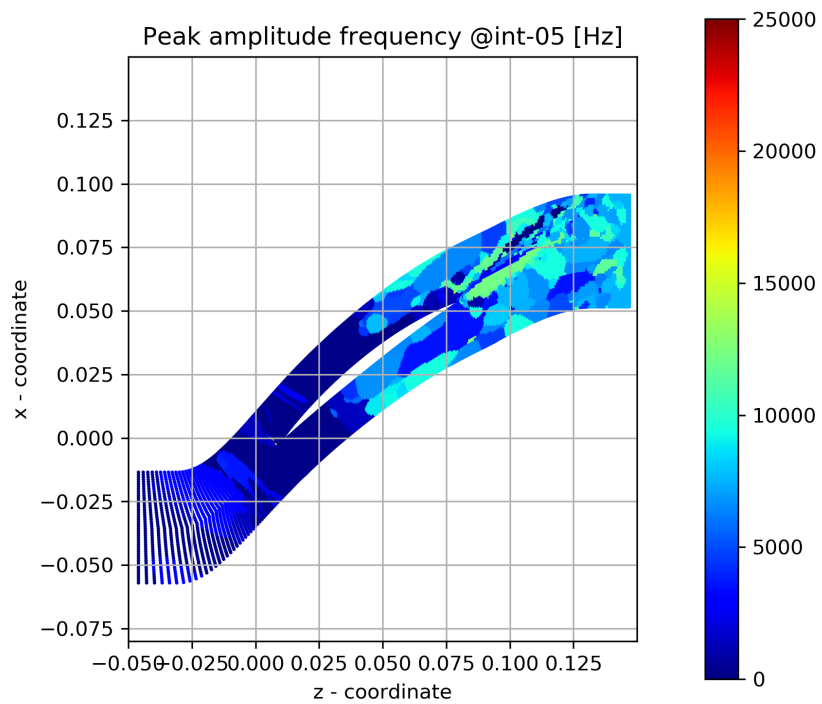


FIGURE B.22: Peak amplitude frequency int-05 mark

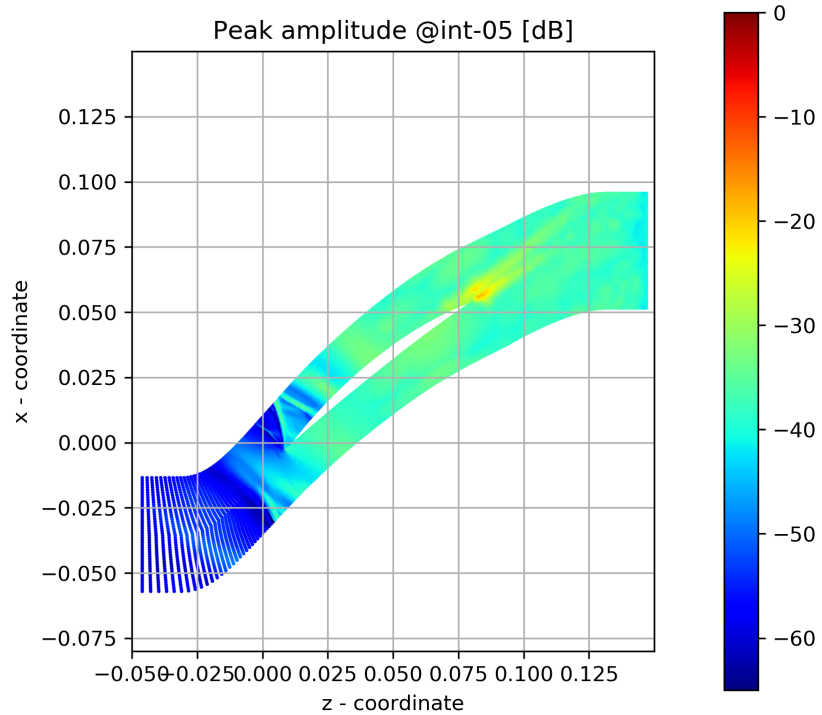


FIGURE B.23: Peak magnitude at int-05 mark

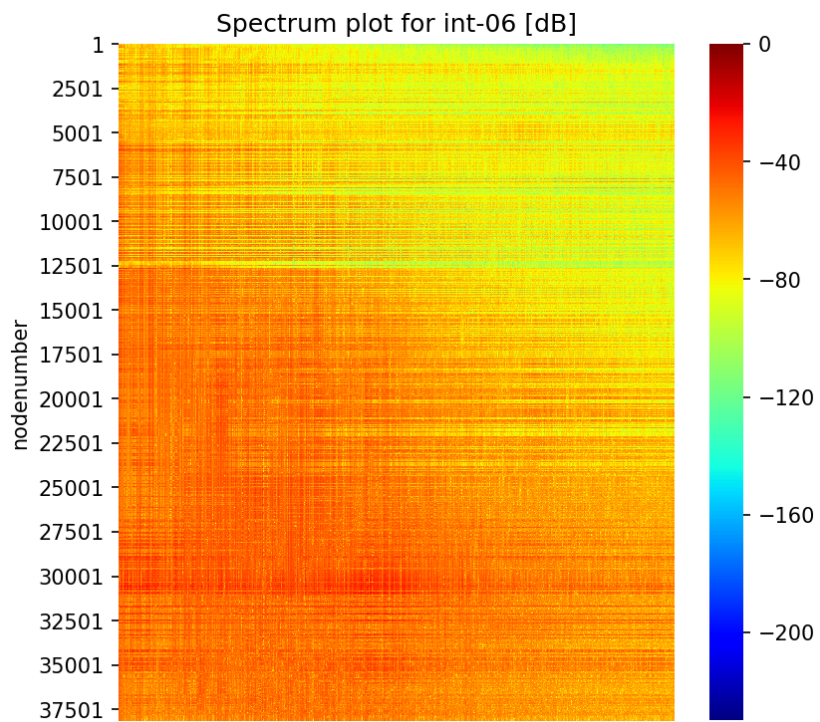


FIGURE B.24: Spectrum plot at int-06 mark

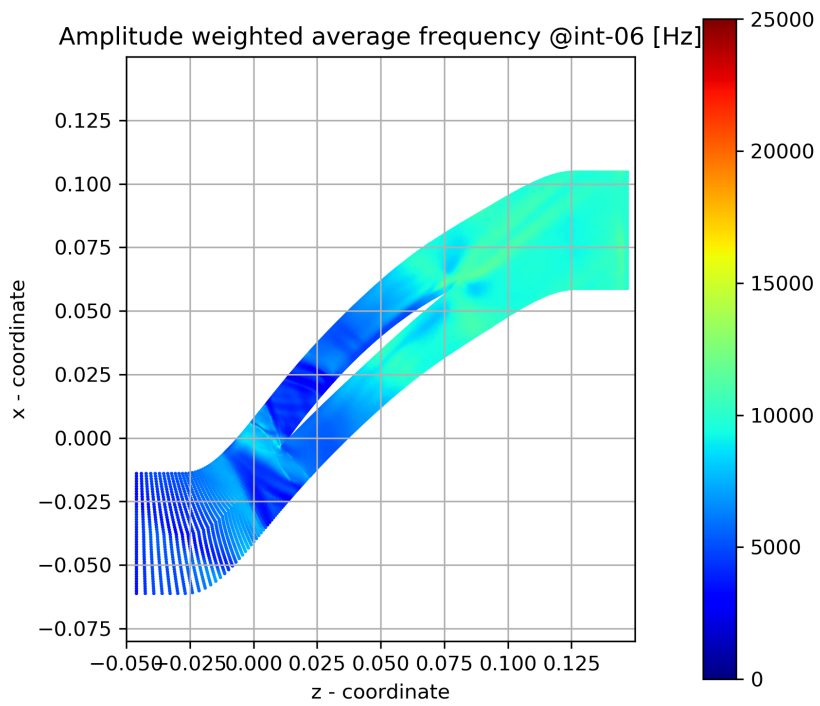


FIGURE B.25: Amplitude weighted average frequency at int-06 mark

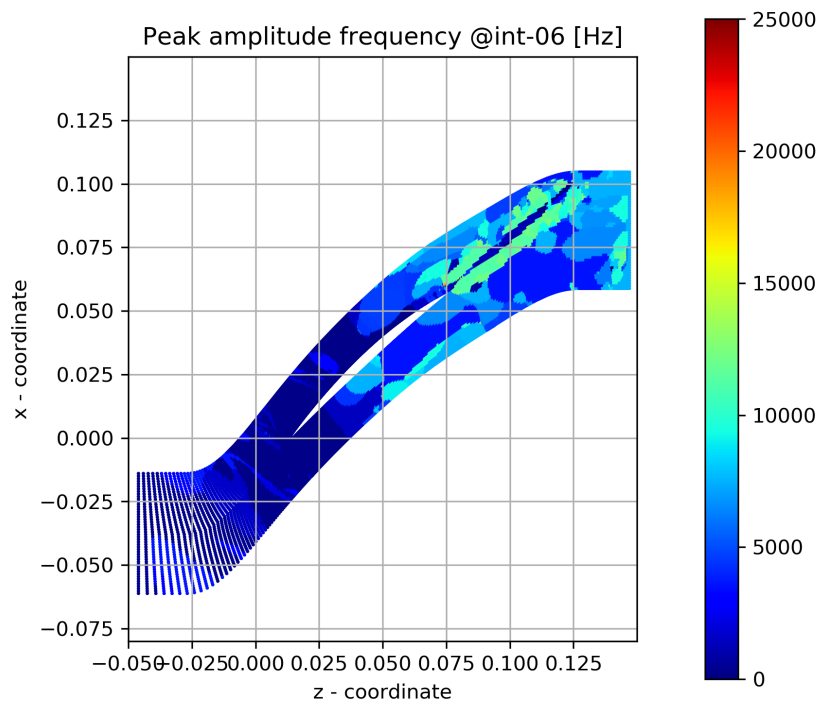


FIGURE B.26: Peak amplitude frequency int-06 mark

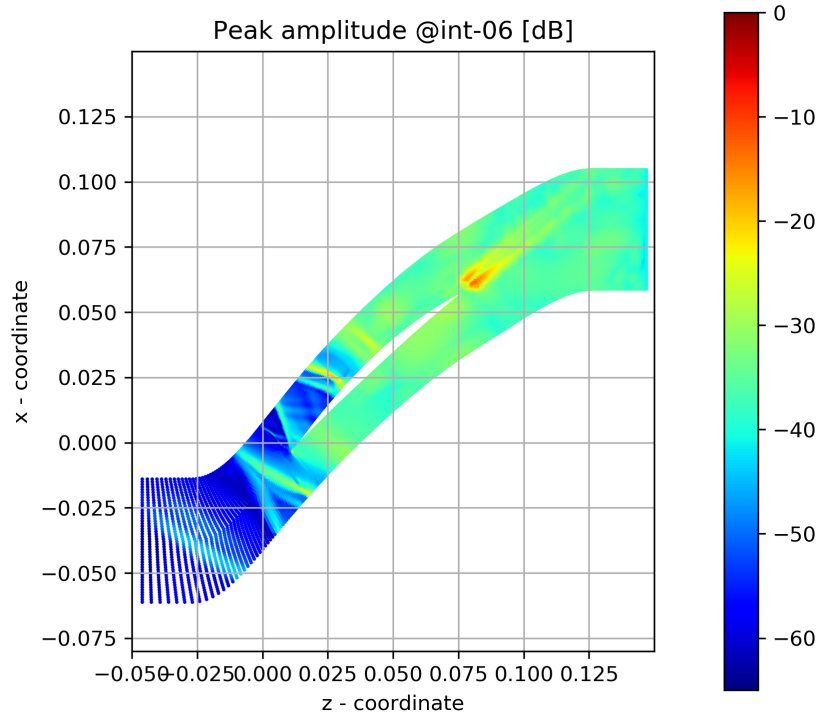


FIGURE B.27: Peak magnitude at int-06 mark

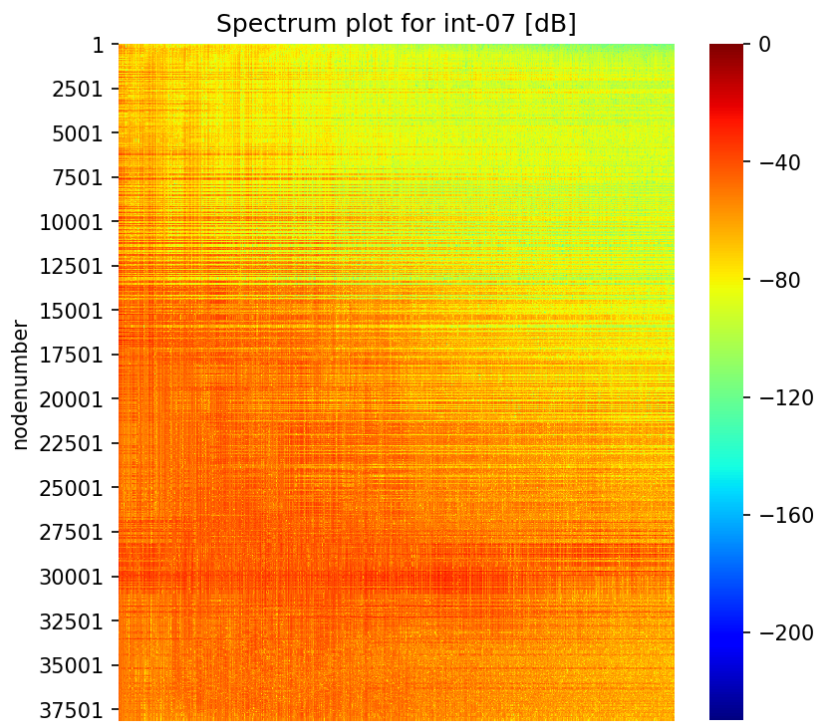


FIGURE B.28: Spectrum plot at int-07 mark

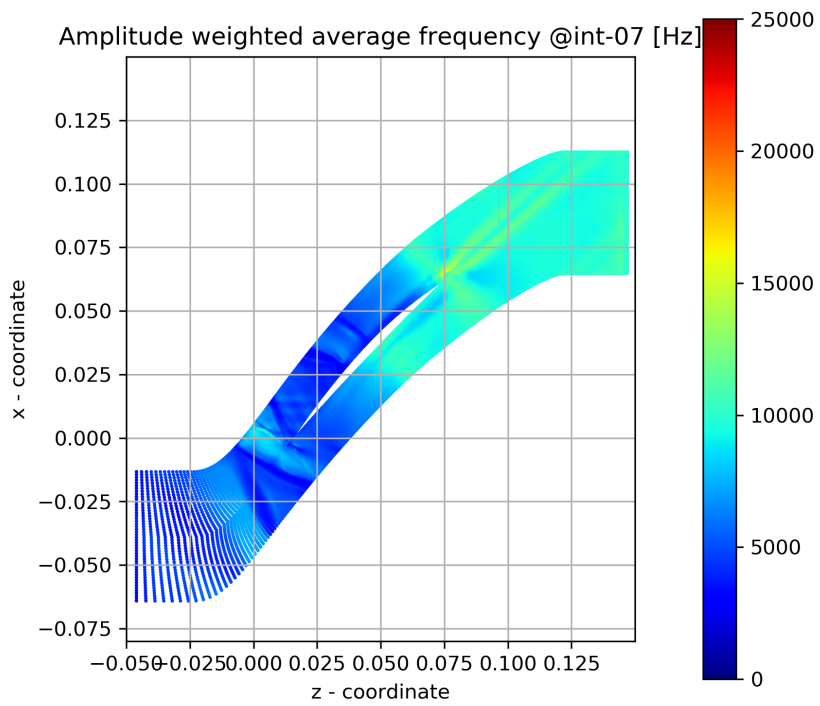


FIGURE B.29: Amplitude weighted average frequency at int-07 mark

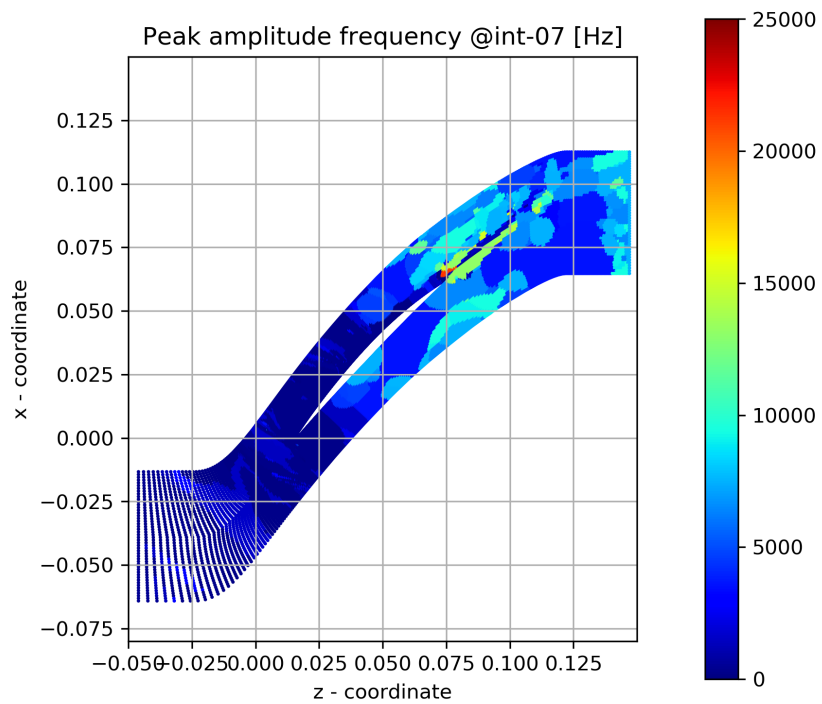


FIGURE B.30: Peak amplitude frequency int-07 mark

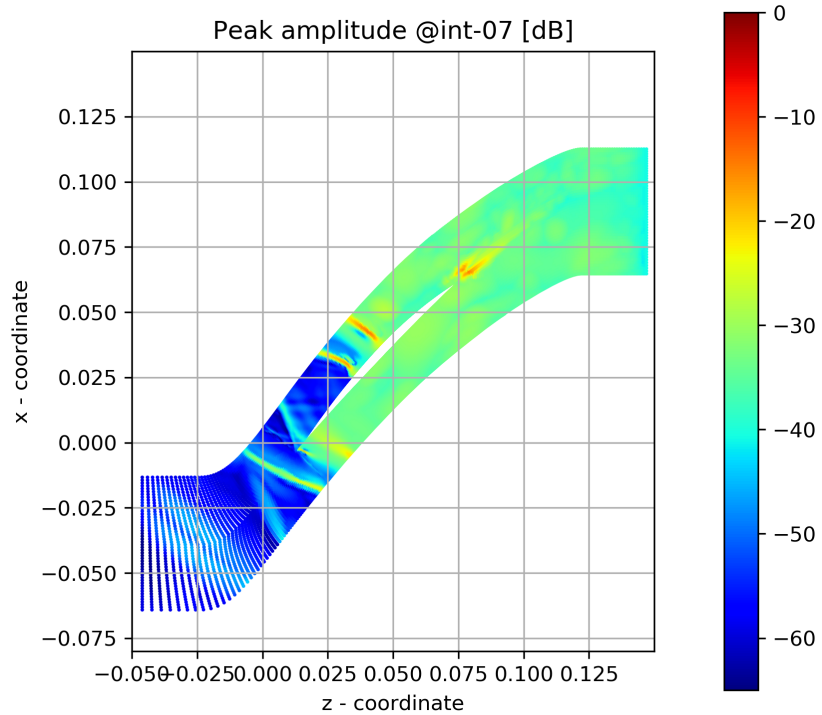


FIGURE B.31: Peak magnitude at int-07 mark

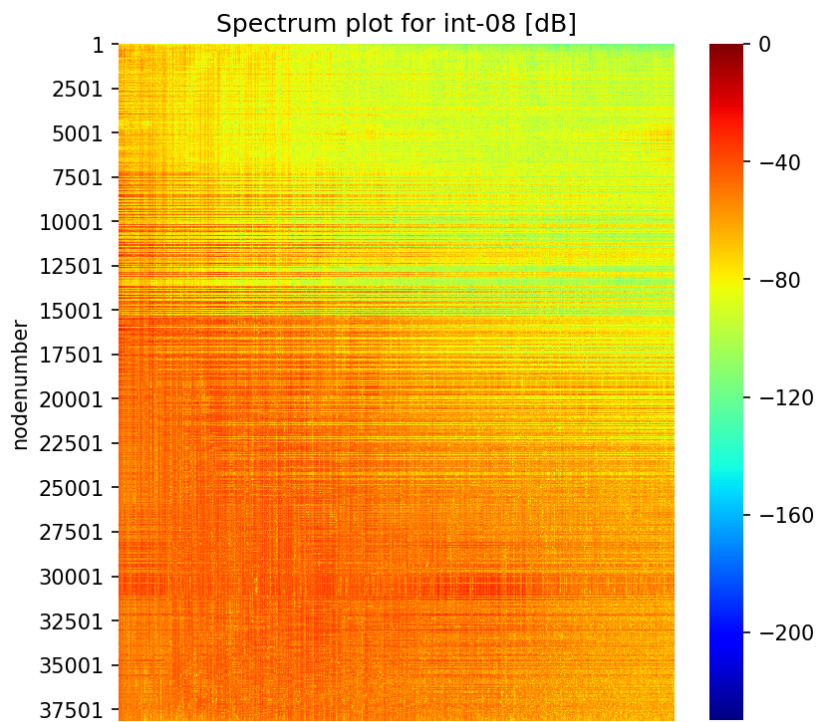


FIGURE B.32: Spectrum plot at int-08 mark

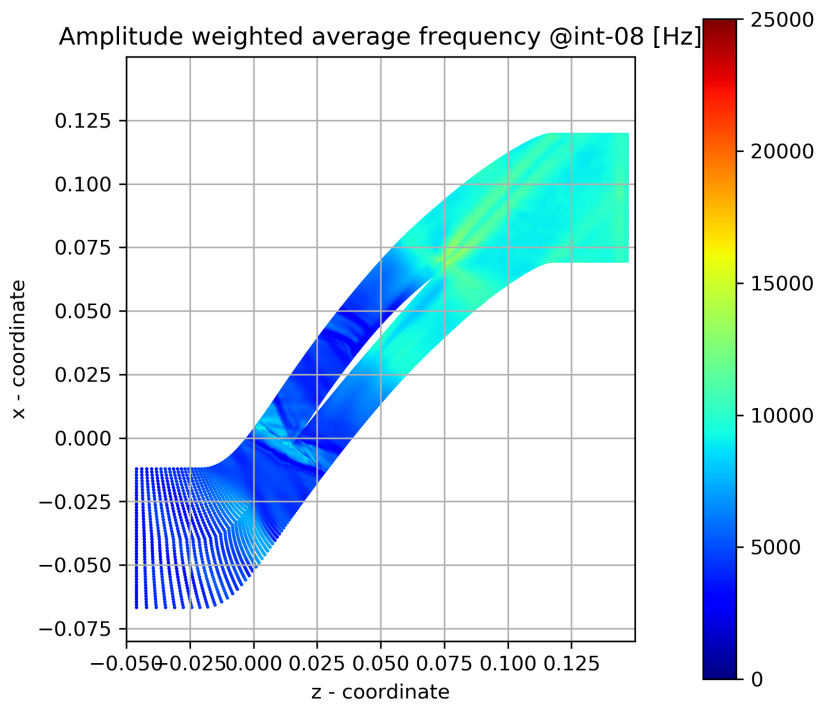


FIGURE B.33: Amplitude weighted average frequency at int-08 mark

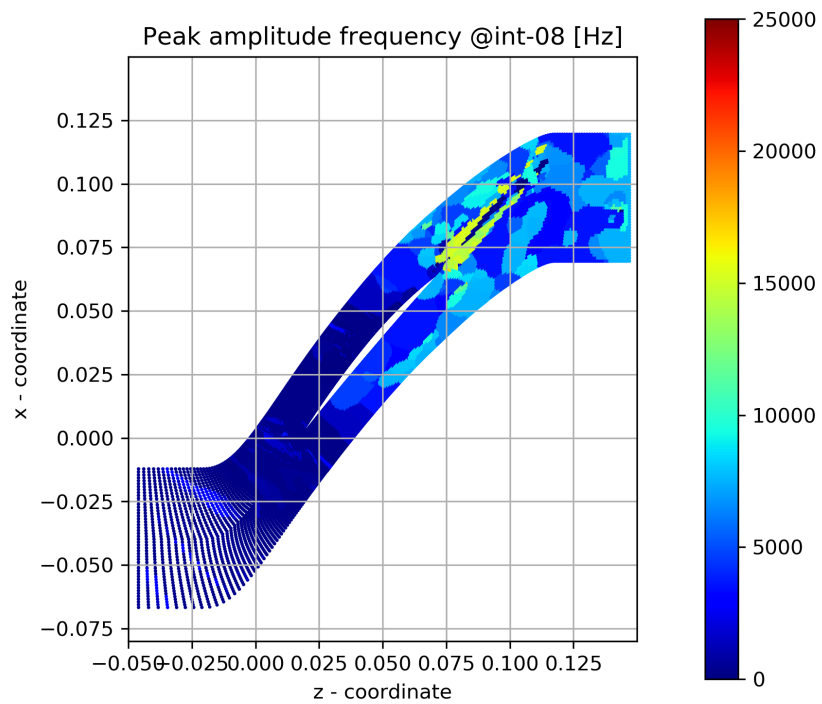


FIGURE B.34: Peak amplitude frequency int-08 mark

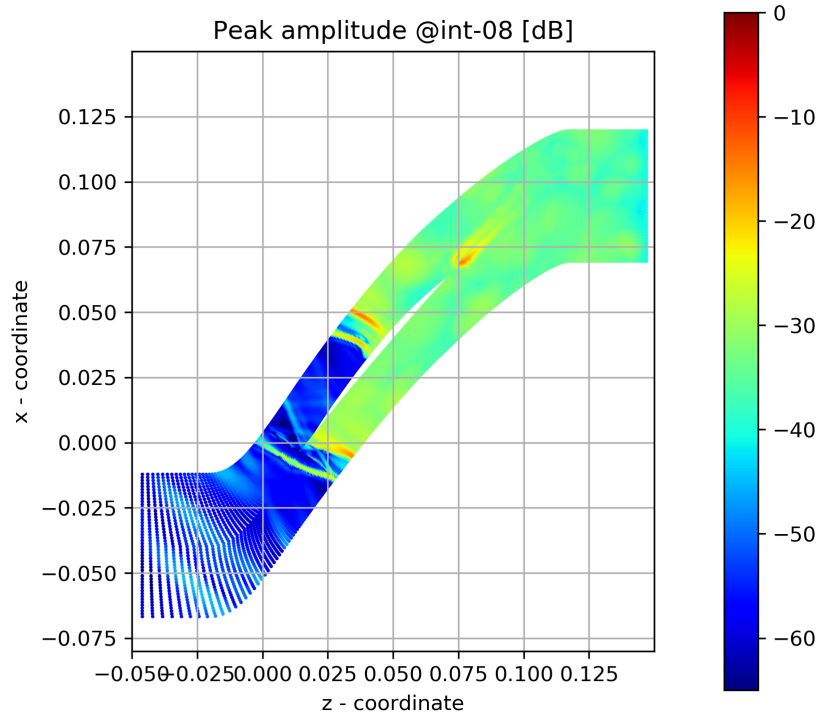


FIGURE B.35: Peak magnitude at int-08 mark

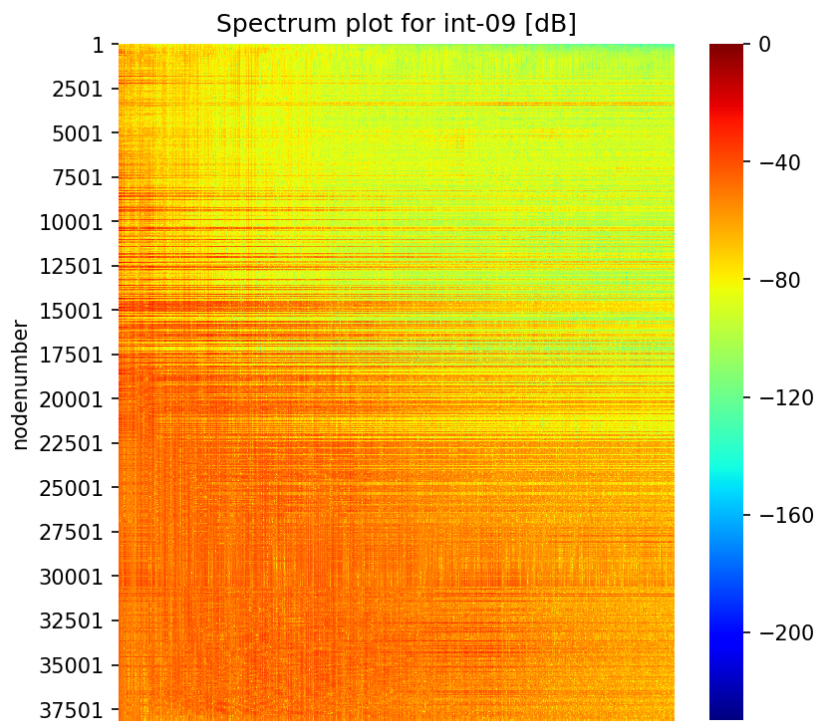


FIGURE B.36: Spectrum plot at int-09 mark

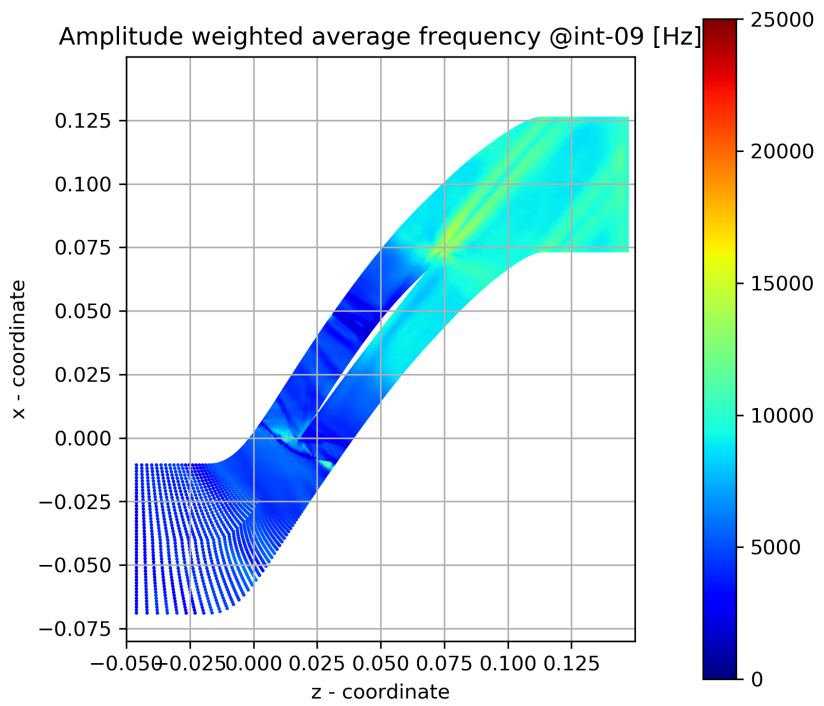


FIGURE B.37: Amplitude weighted average frequency at int-09 mark

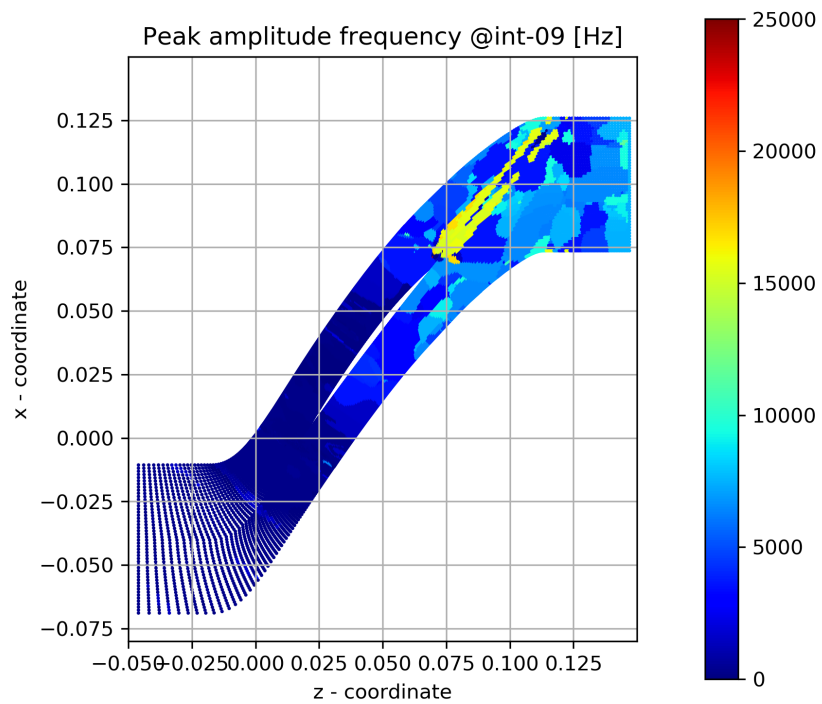


FIGURE B.38: Peak amplitude frequency int-09 mark

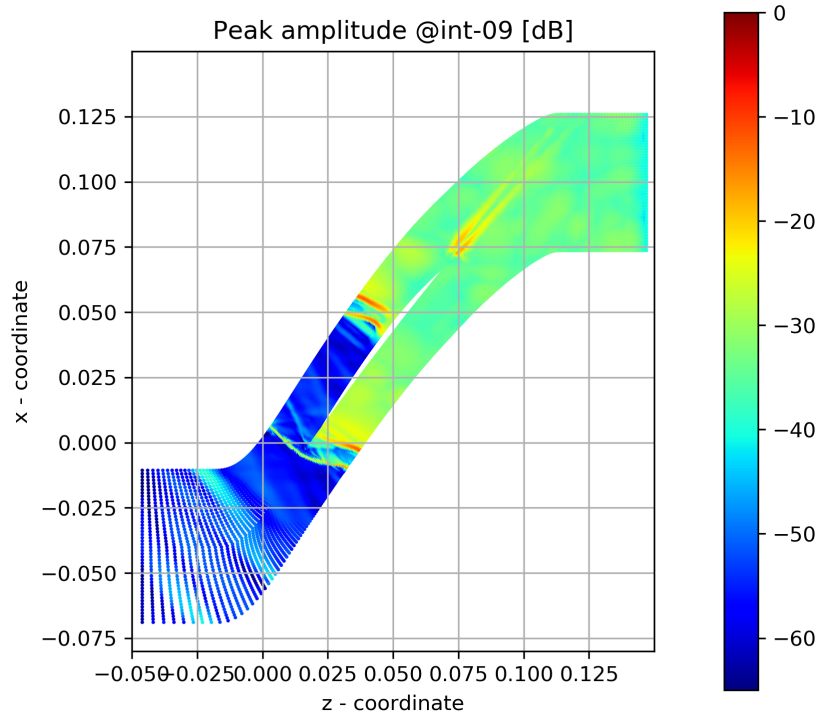


FIGURE B.39: Peak magnitude at int-09 mark

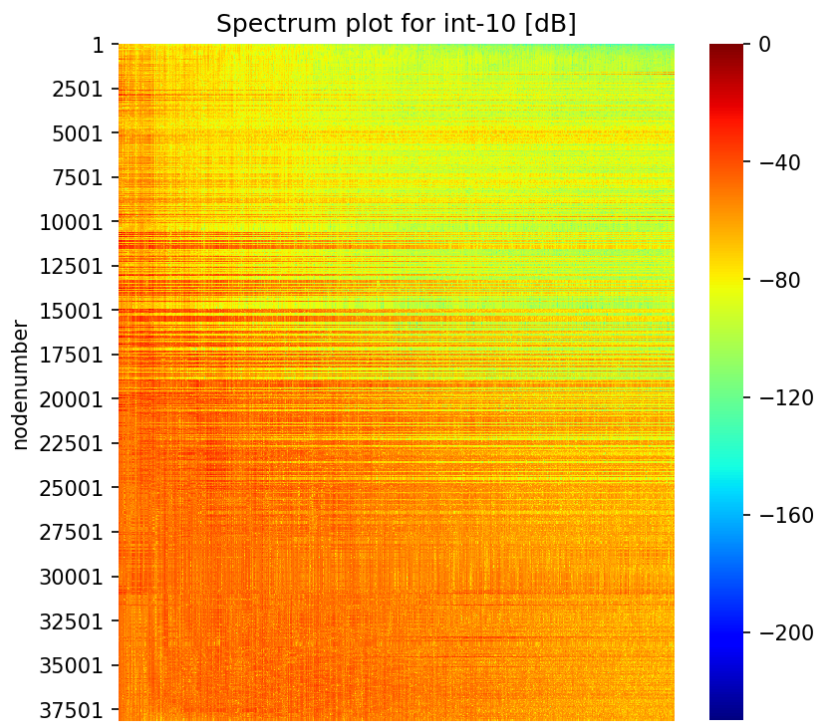


FIGURE B.40: Spectrum plot at int-10 mark

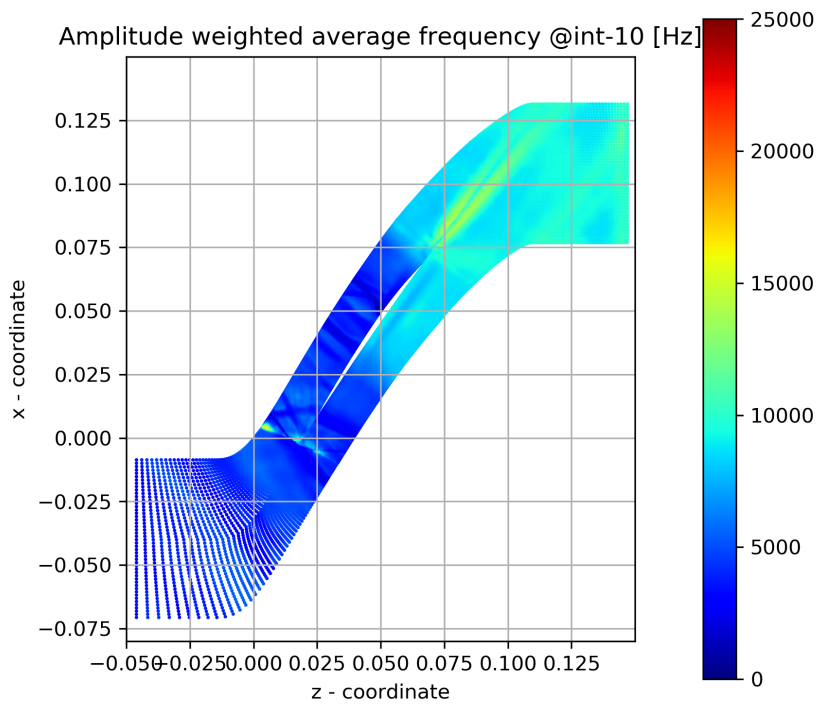


FIGURE B.41: Amplitude weighted average frequency at int-10 mark

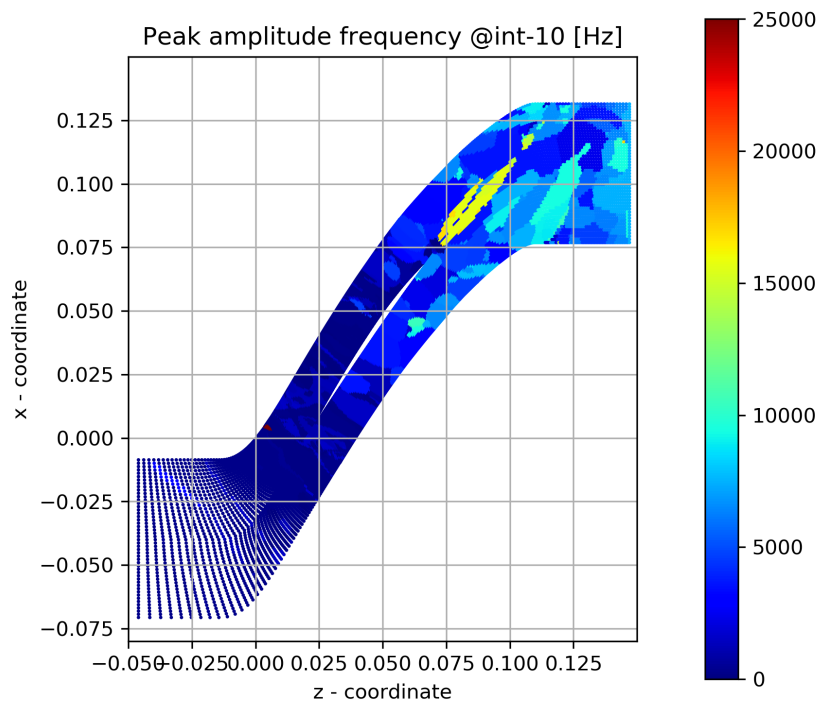


FIGURE B.42: Peak amplitude frequency int-10 mark

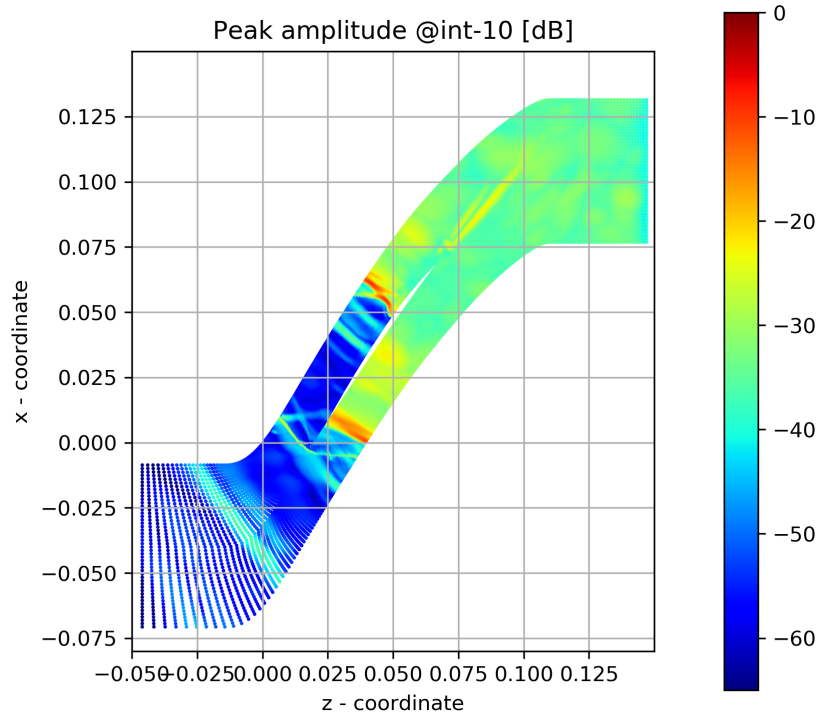


FIGURE B.43: Peak magnitude at int-10 mark

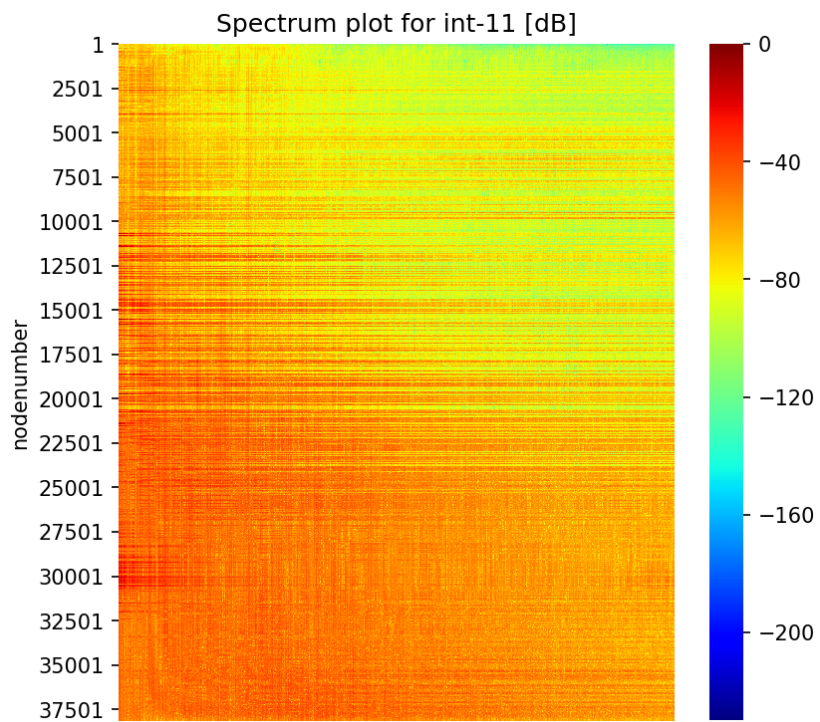


FIGURE B.44: Spectrum plot at int-11 mark

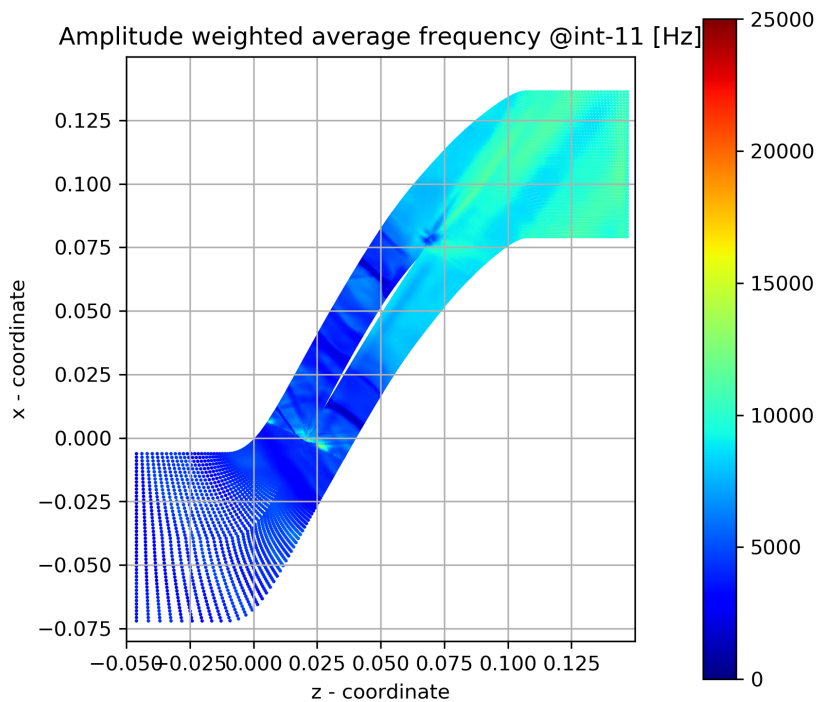


FIGURE B.45: Amplitude weighted average frequency at int-11 mark

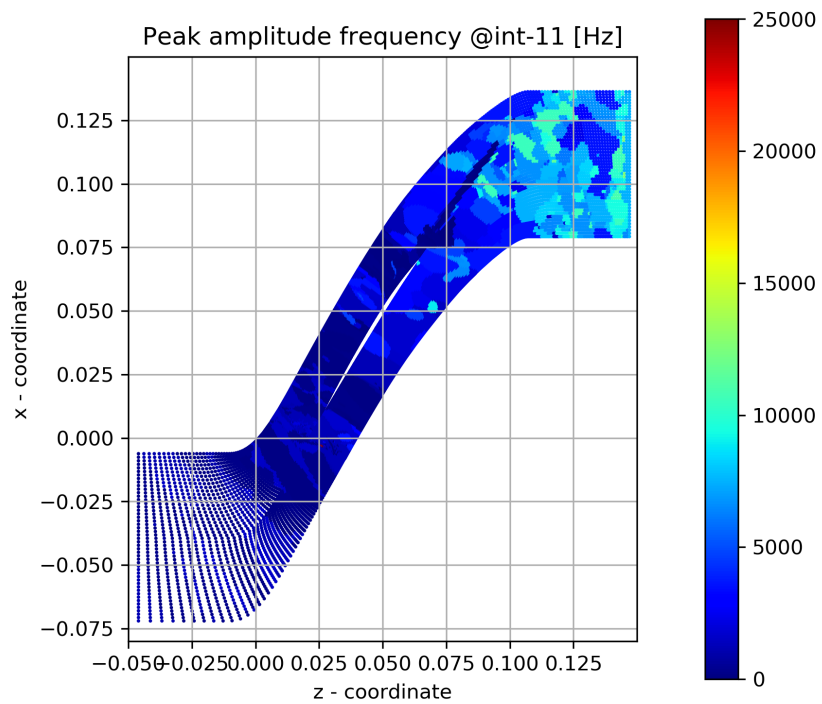


FIGURE B.46: Peak amplitude frequency int-11 mark

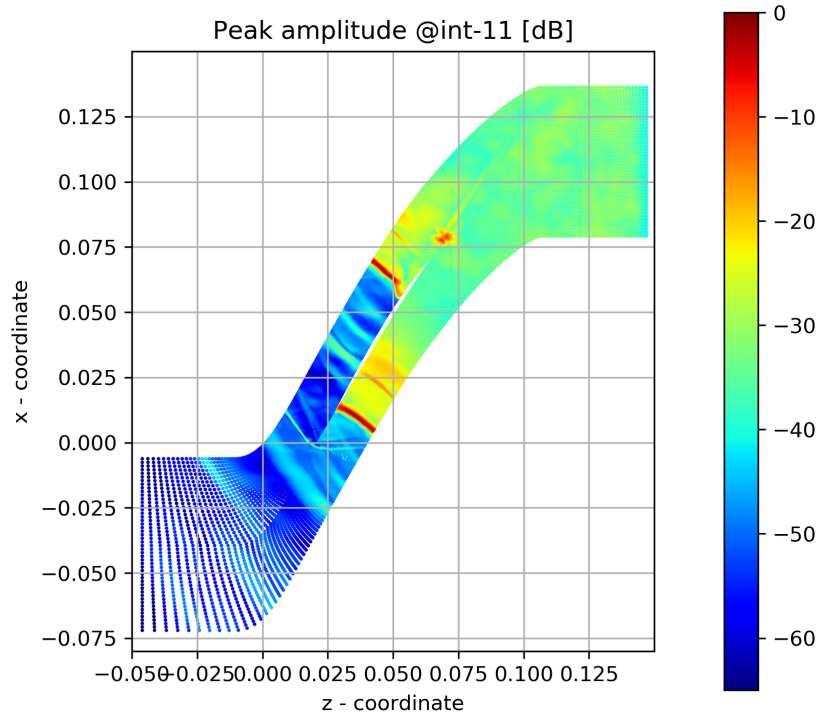


FIGURE B.47: Peak magnitude at int-11 mark

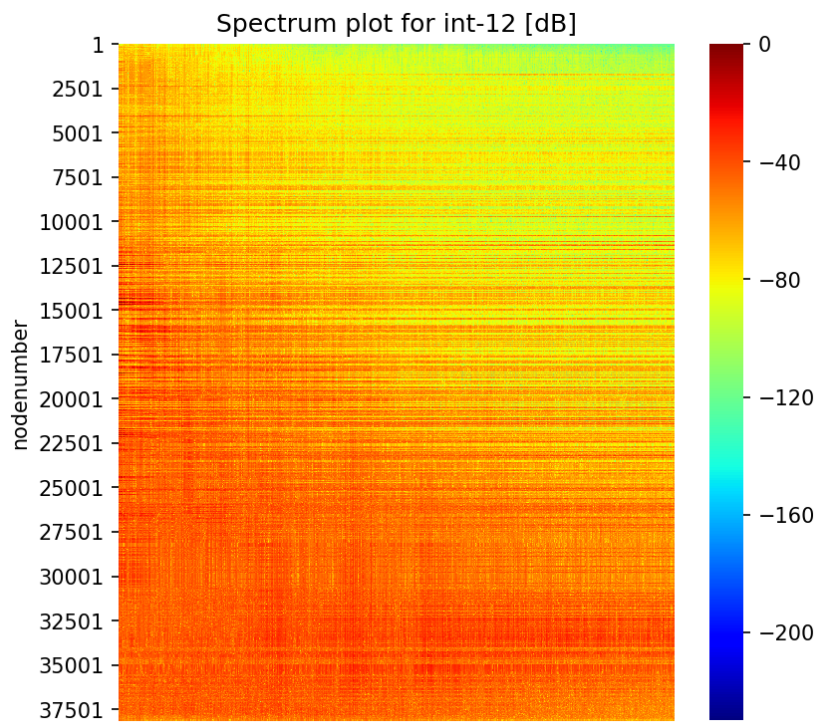


FIGURE B.48: Spectrum plot at int-12 mark

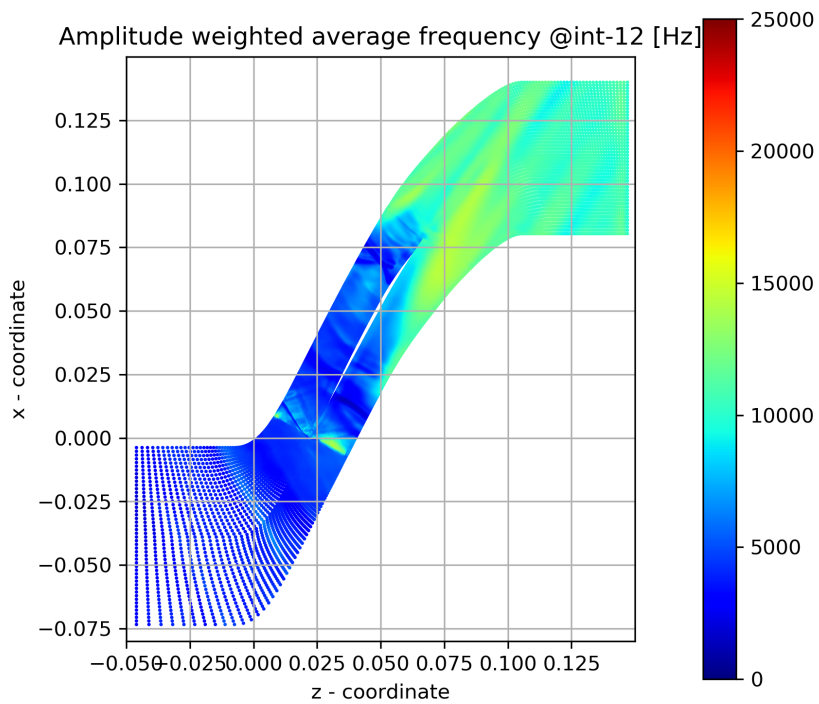


FIGURE B.49: Amplitude weighted average frequency at int-12 mark

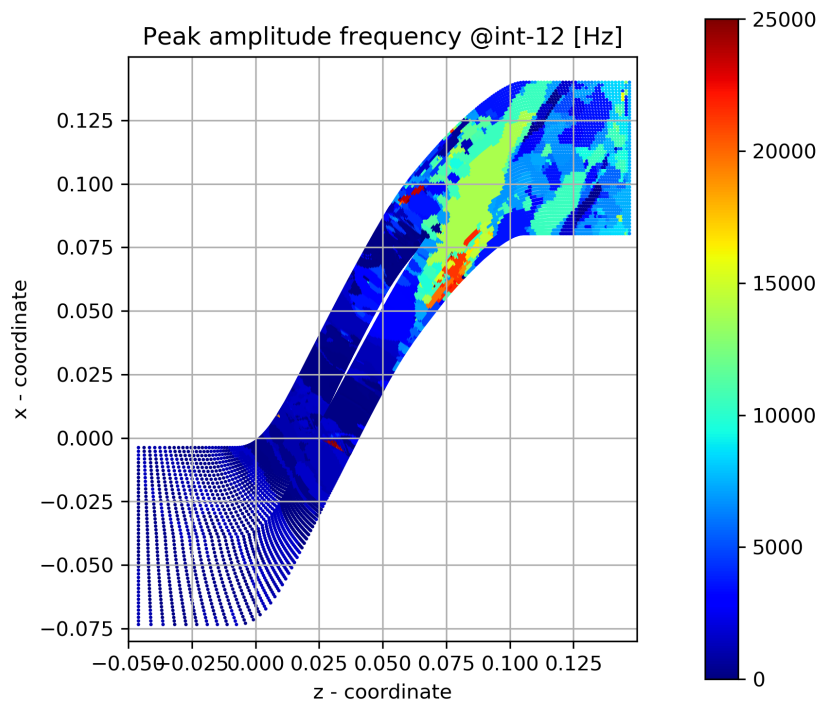


FIGURE B.50: Peak amplitude frequency int-12 mark

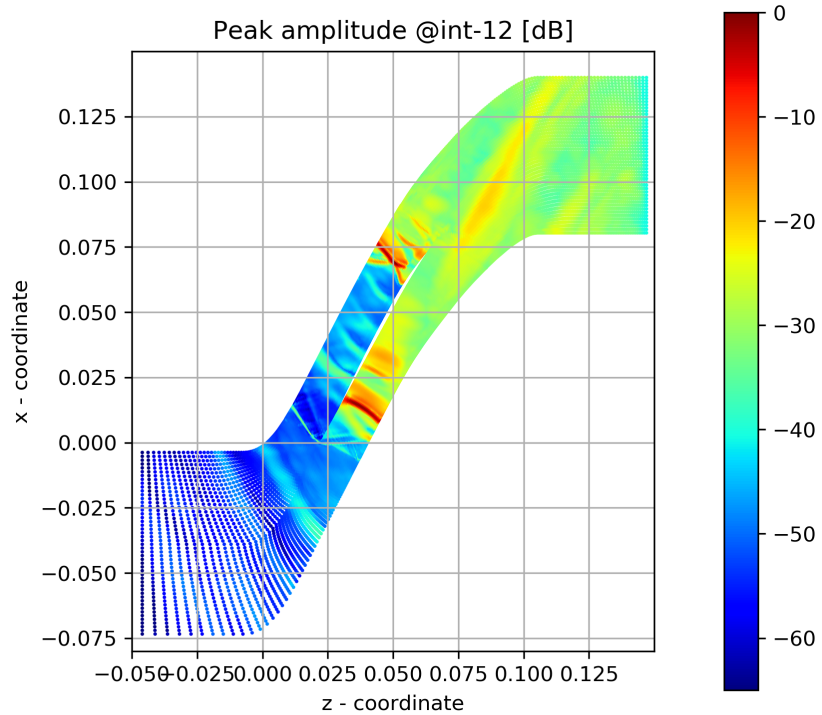


FIGURE B.51: Peak magnitude at int-12 mark

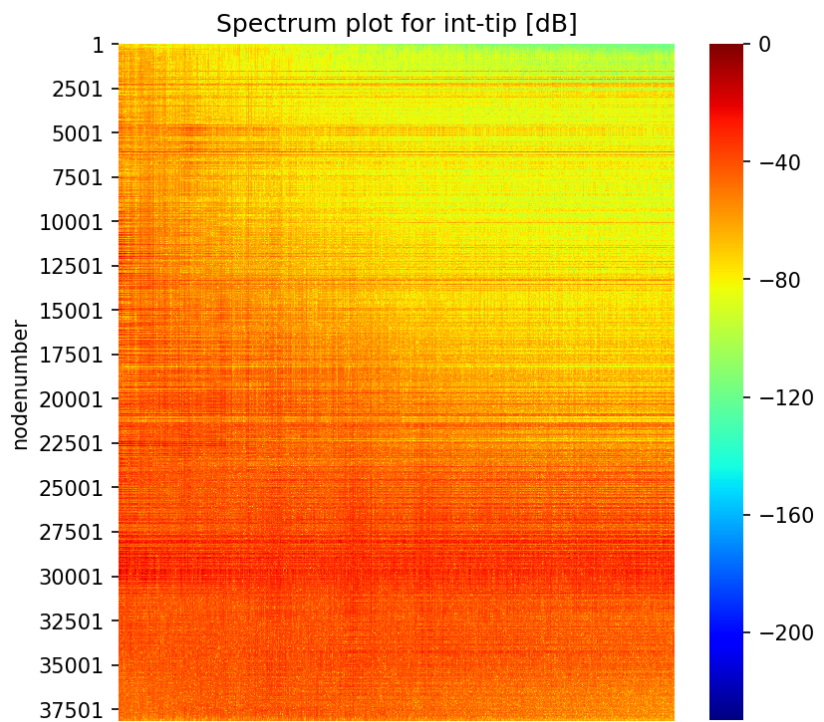


FIGURE B.52: Spectrum plot at int-tip mark

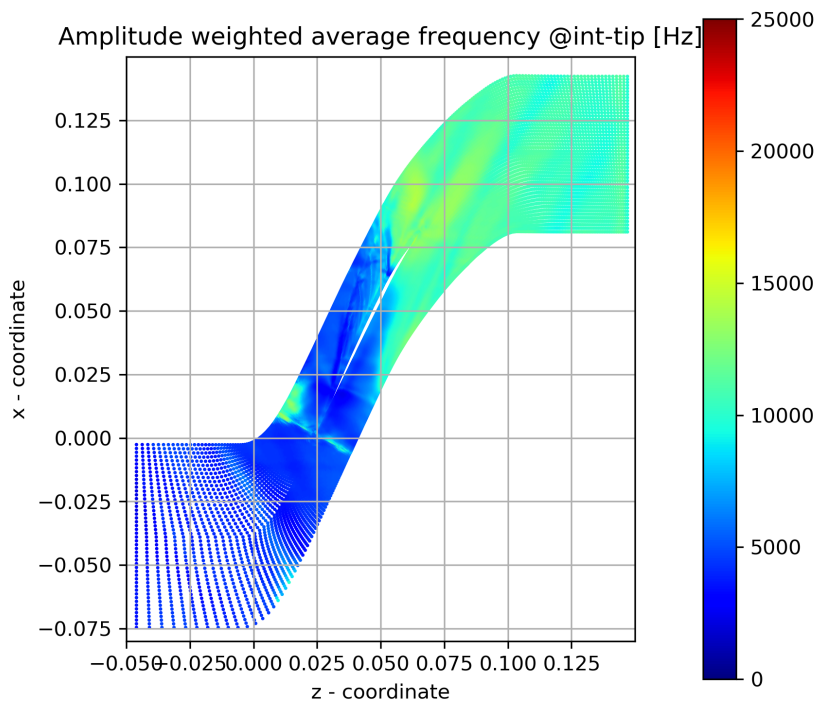


FIGURE B.53: Amplitude weighted average frequency at int-tip mark

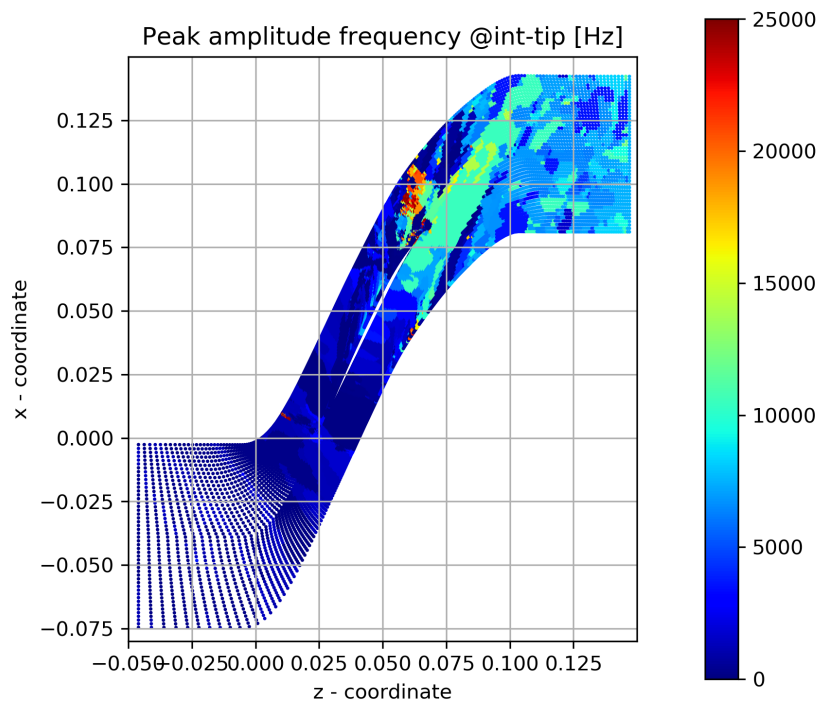


FIGURE B.54: Peak amplitude frequency int-tip mark

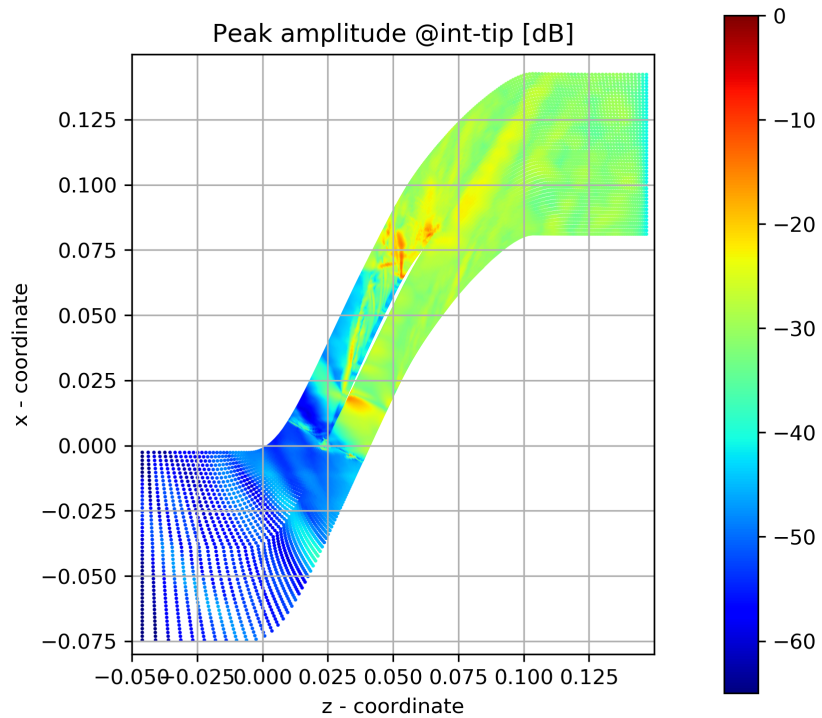


FIGURE B.55: Peak magnitude at int-tip mark

Appendix C

CFD validation

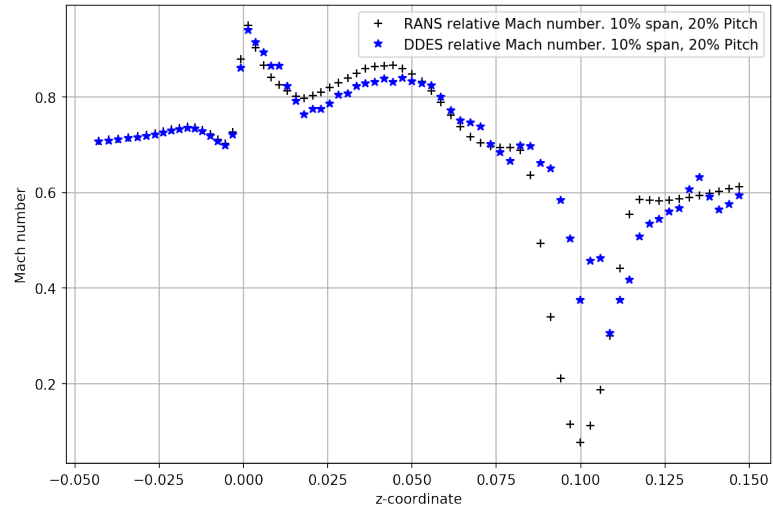


FIGURE C.1: Relative Mach number at S10P20 streamline

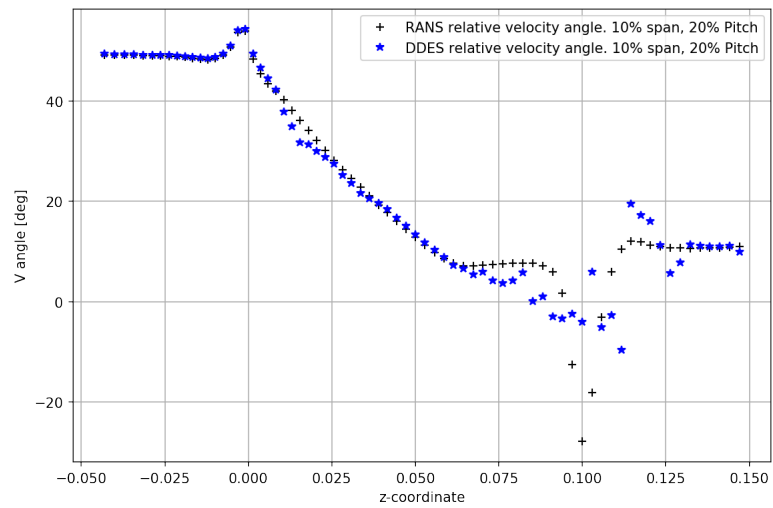


FIGURE C.2: Relative velocity angle at S10P20 streamline

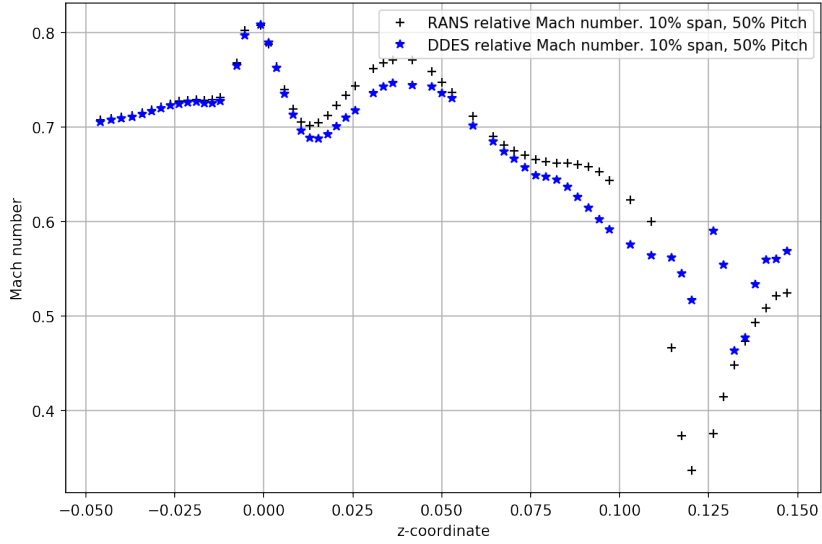


FIGURE C.3: Relative Mach number at S10P50 streamline

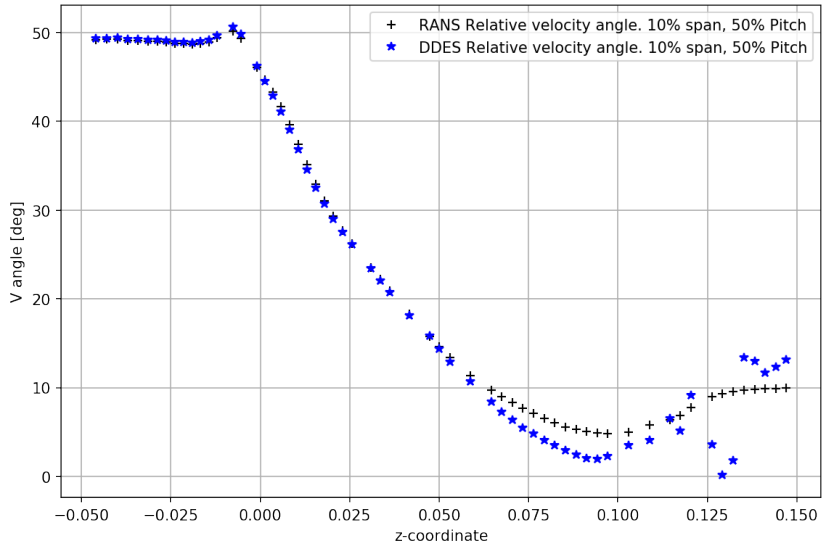


FIGURE C.4: Relative velocity angle at S10P50 streamline

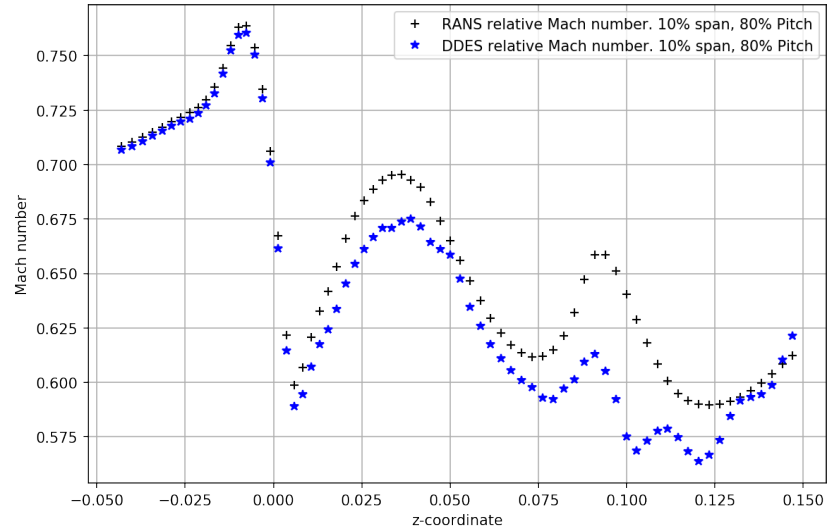


FIGURE C.5: Relative Mach number at S10P80 streamline

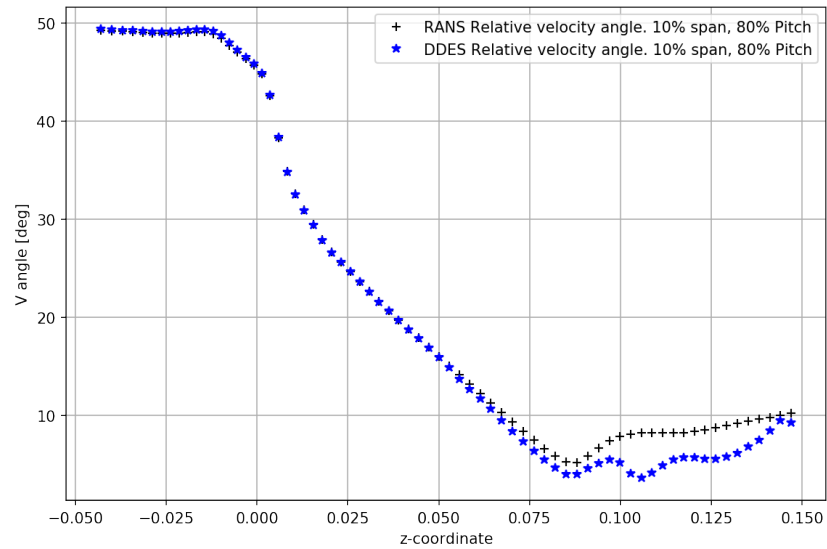


FIGURE C.6: Relative velocity angle at S10P80 streamline

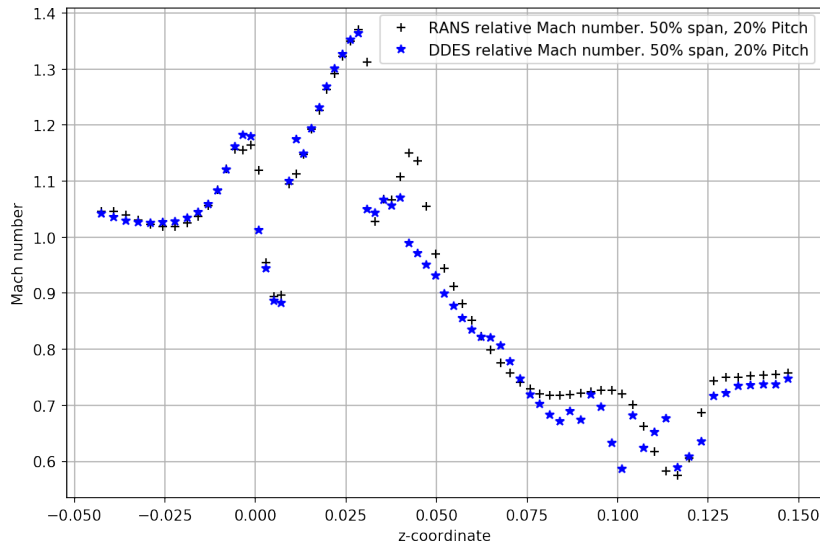


FIGURE C.7: Relative Mach number at S50P20 streamline

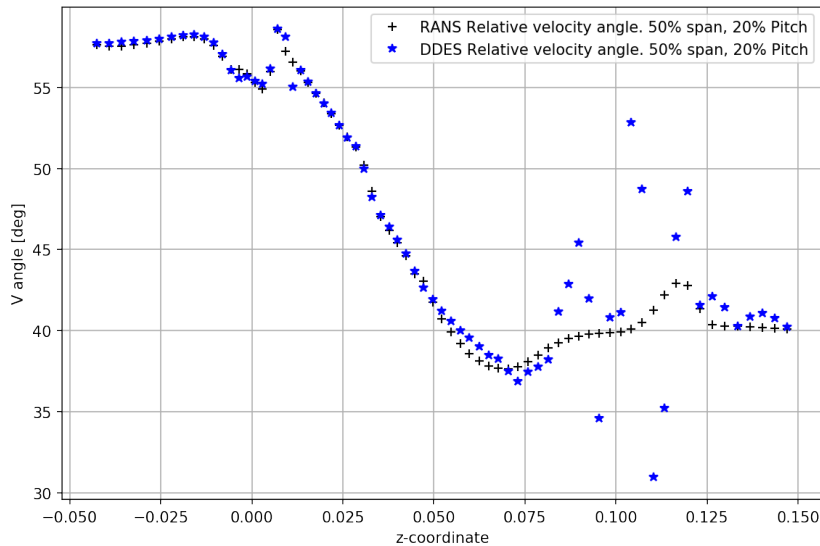


FIGURE C.8: Relative velocity angle at S50P20 streamline

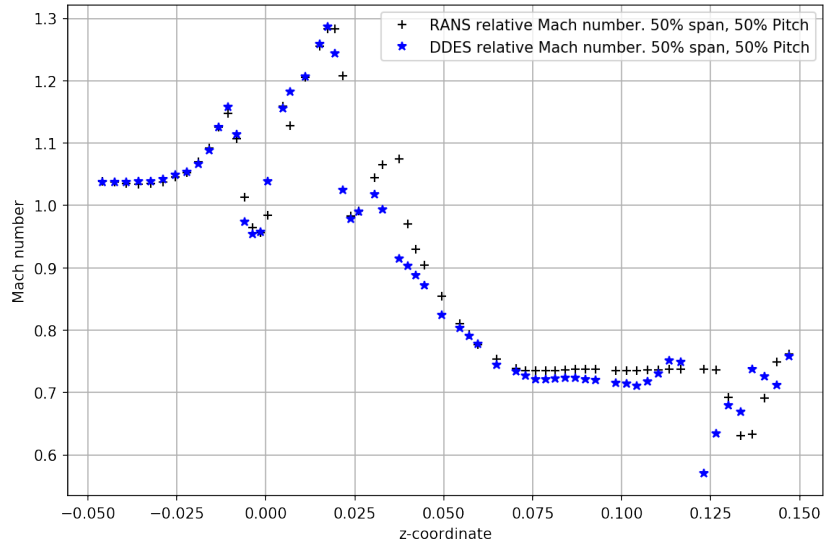


FIGURE C.9: Relative Mach number at S50P50 streamline

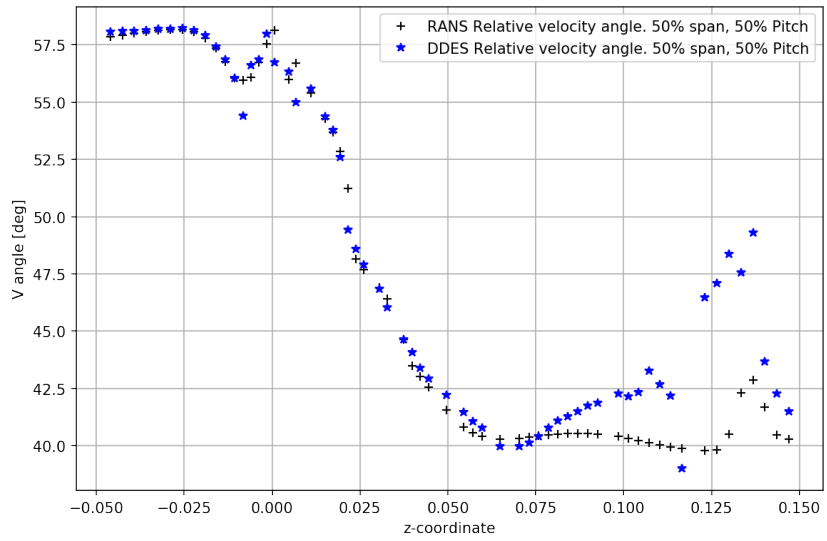


FIGURE C.10: Relative velocity angle at S50P50 streamline

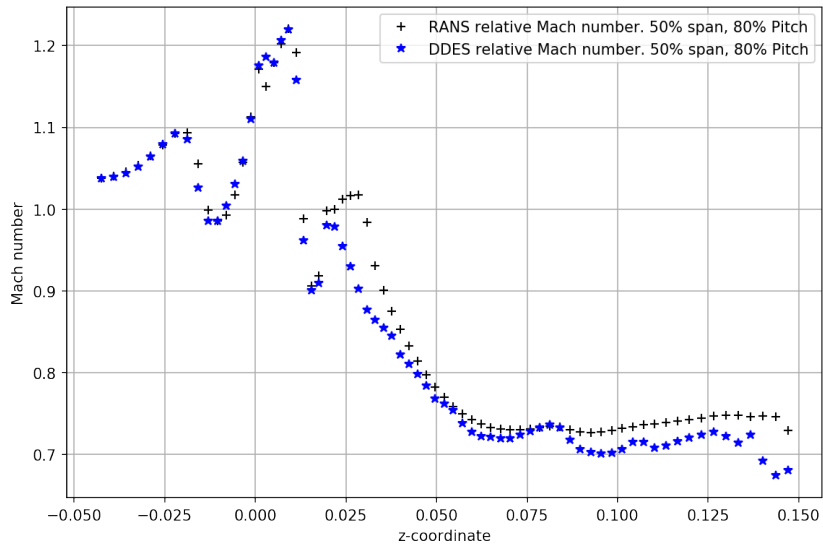


FIGURE C.11: Relative Mach number at S50P80 streamline

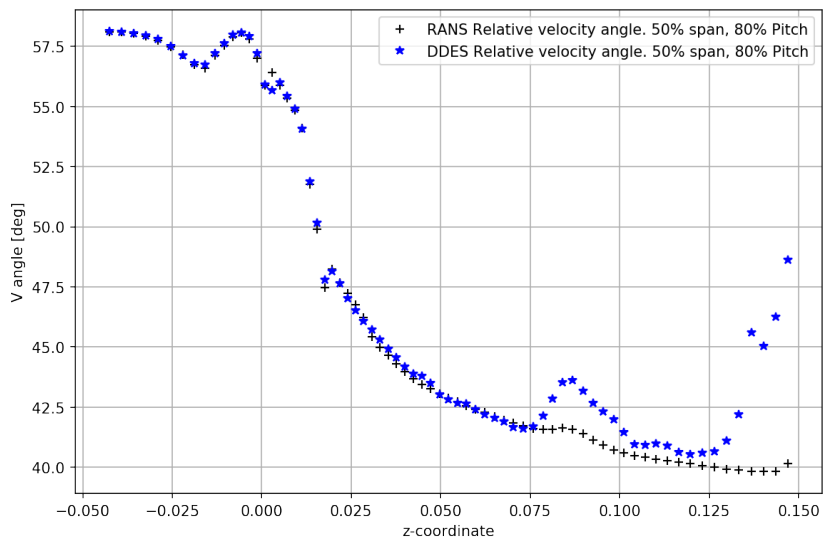


FIGURE C.12: Relative velocity angle at S50P80 streamline

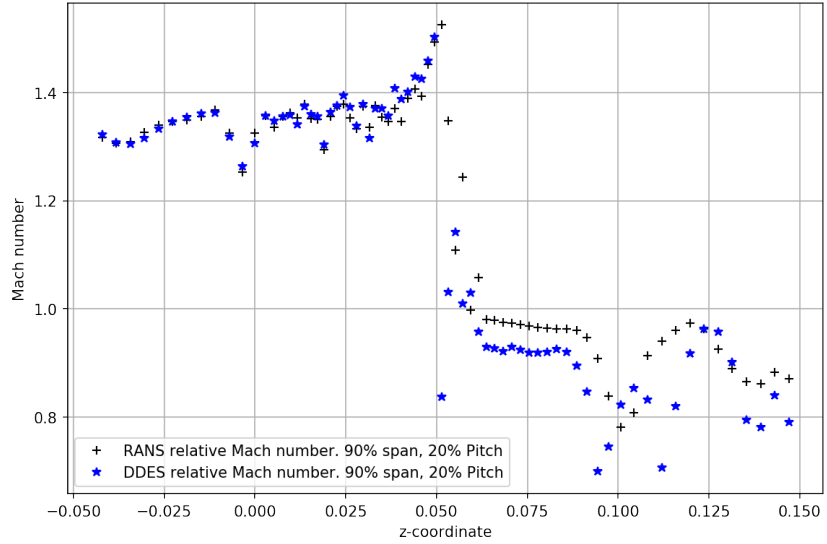


FIGURE C.13: Relative Mach number at S90P20 streamline

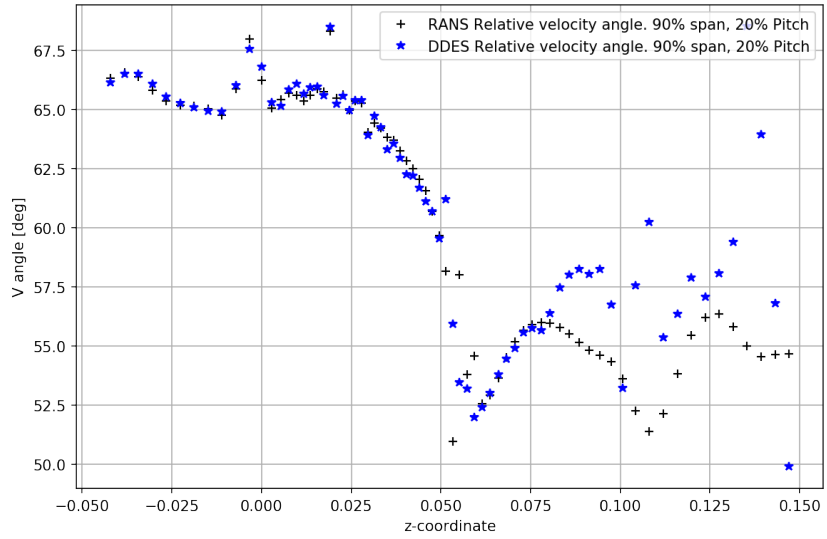


FIGURE C.14: Relative velocity angle at S90P20 streamline

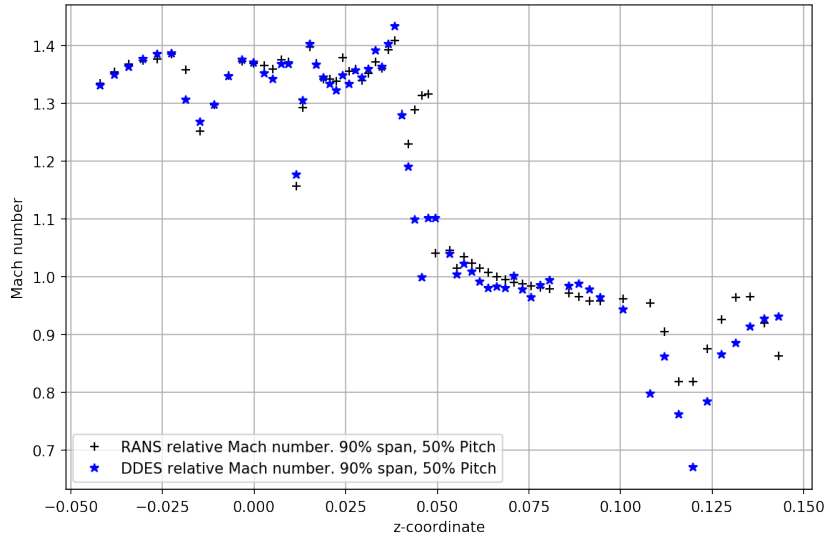


FIGURE C.15: Relative Mach number at S90P50 streamline

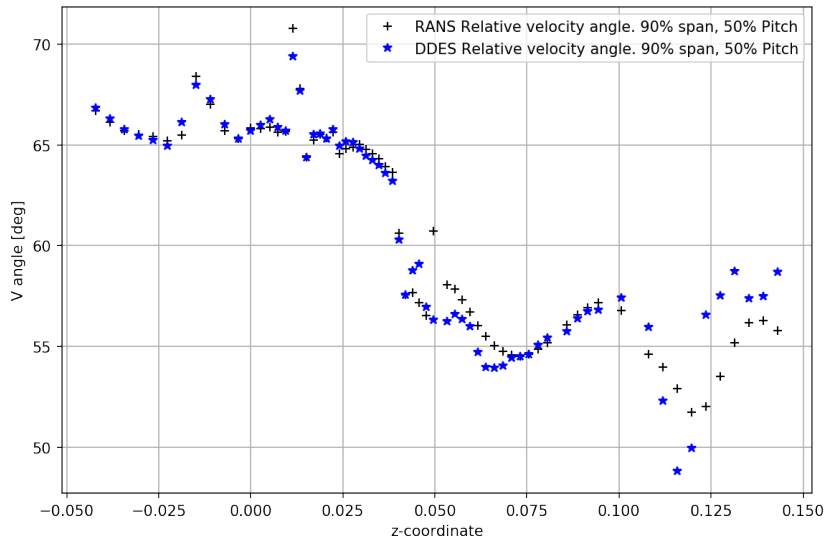


FIGURE C.16: Relative velocity angle at S90P50 streamline

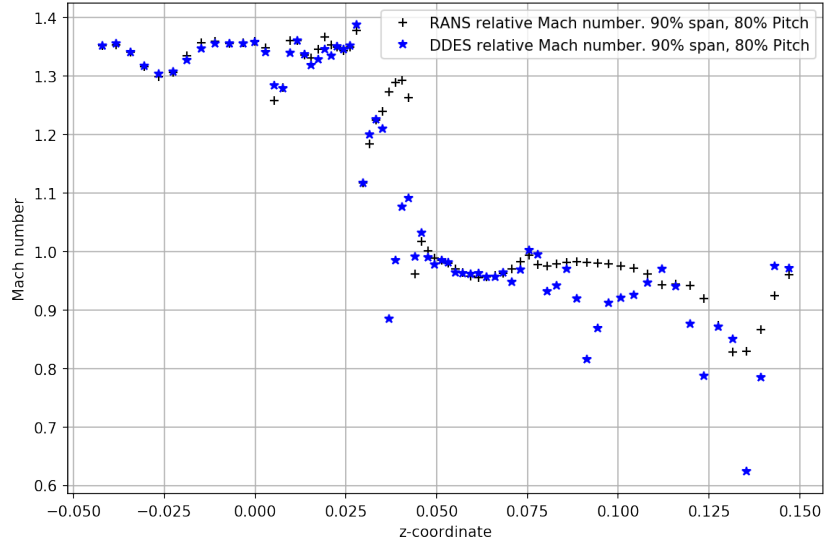


FIGURE C.17: Relative Mach number at S90P80 streamline

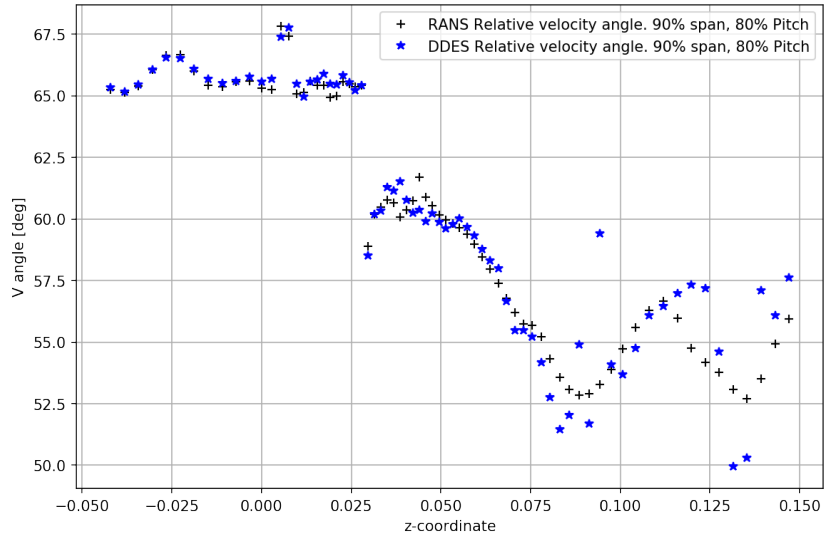


FIGURE C.18: Relative velocity angle at S90P80 streamline

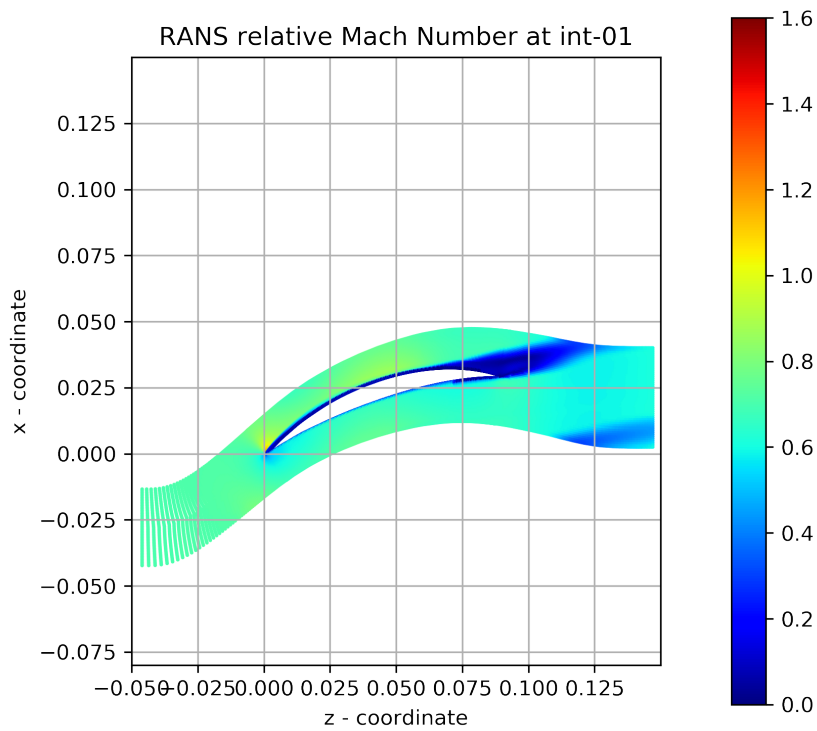


FIGURE C.19: RANS Mach number contour plot at int-01 mark

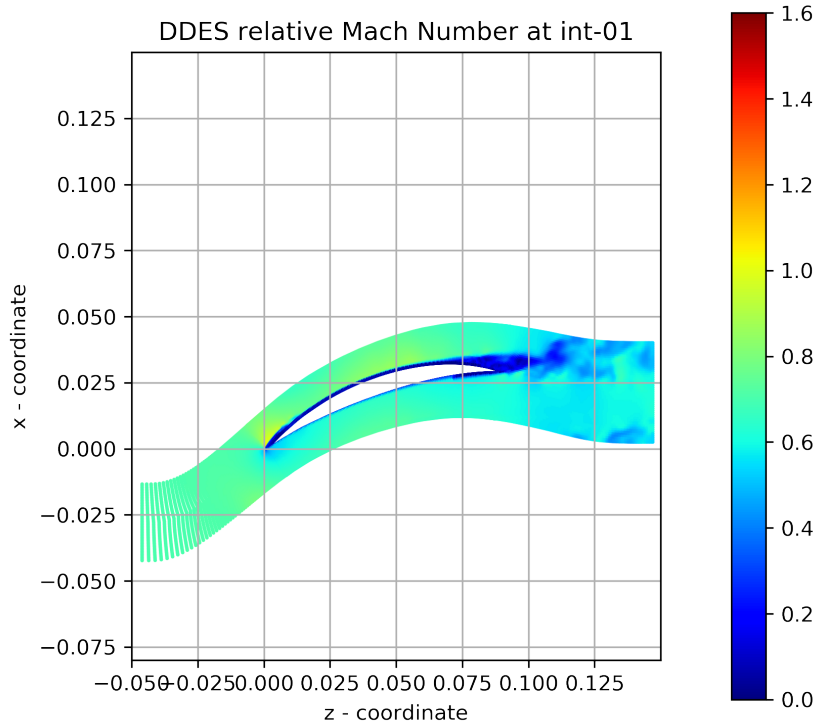


FIGURE C.20: DDES Mach number contour plot at int-01 mark

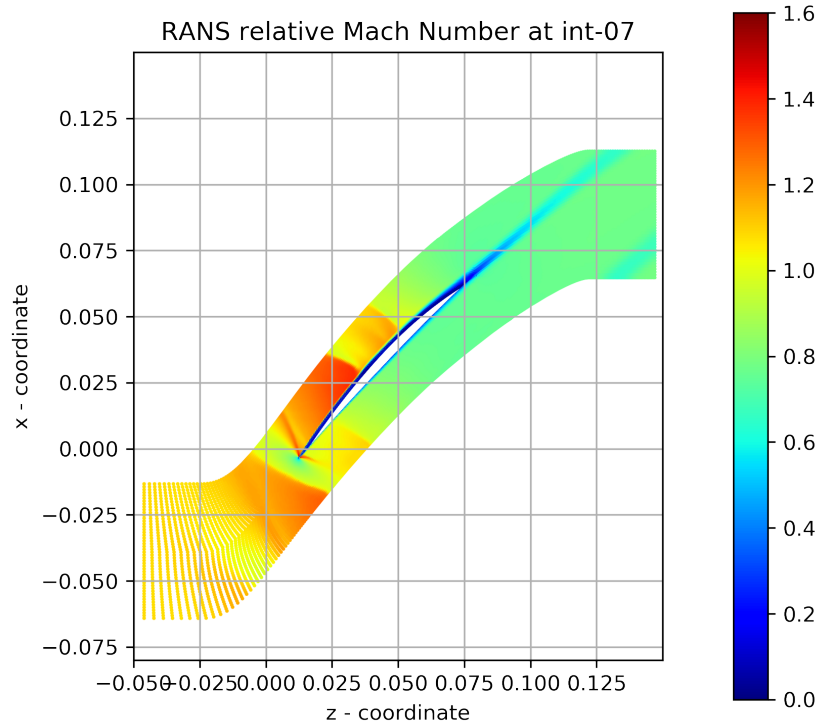


FIGURE C.21: RANS Mach number contour plot at int-07 mark

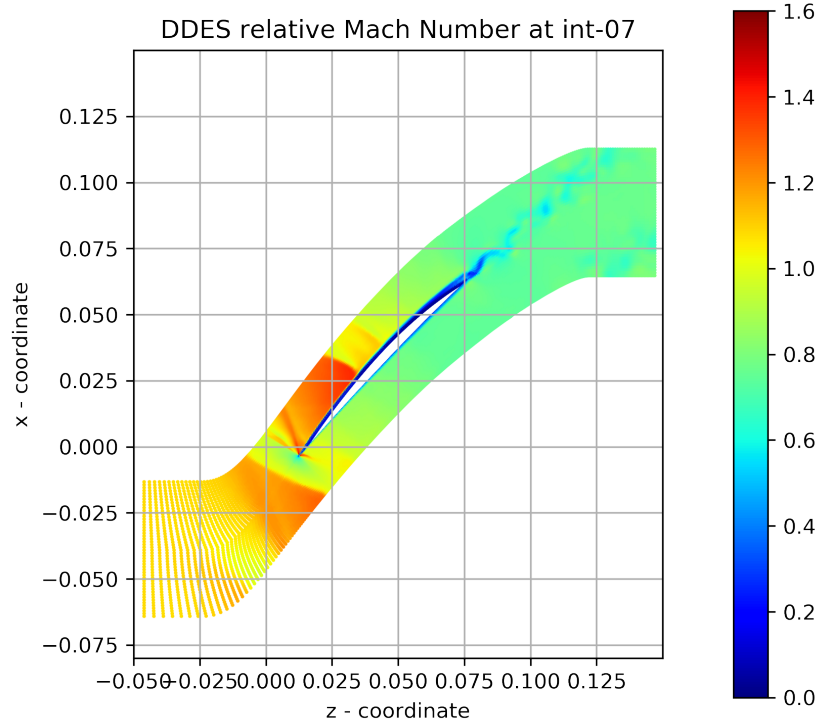


FIGURE C.22: DDES Mach number contour plot at int-07 mark

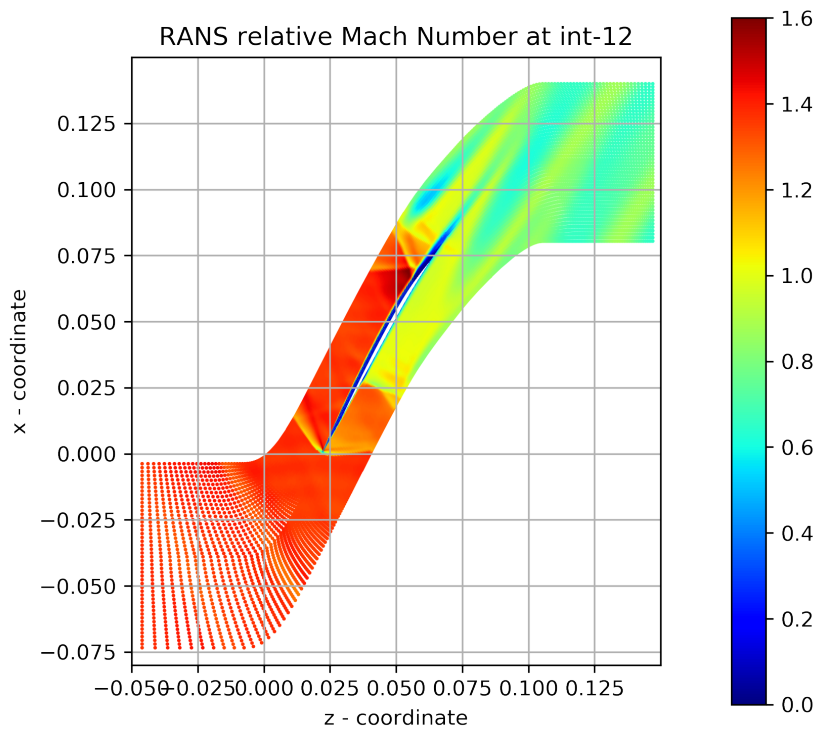


FIGURE C.23: RANS Mach number contour plot at int-12 mark

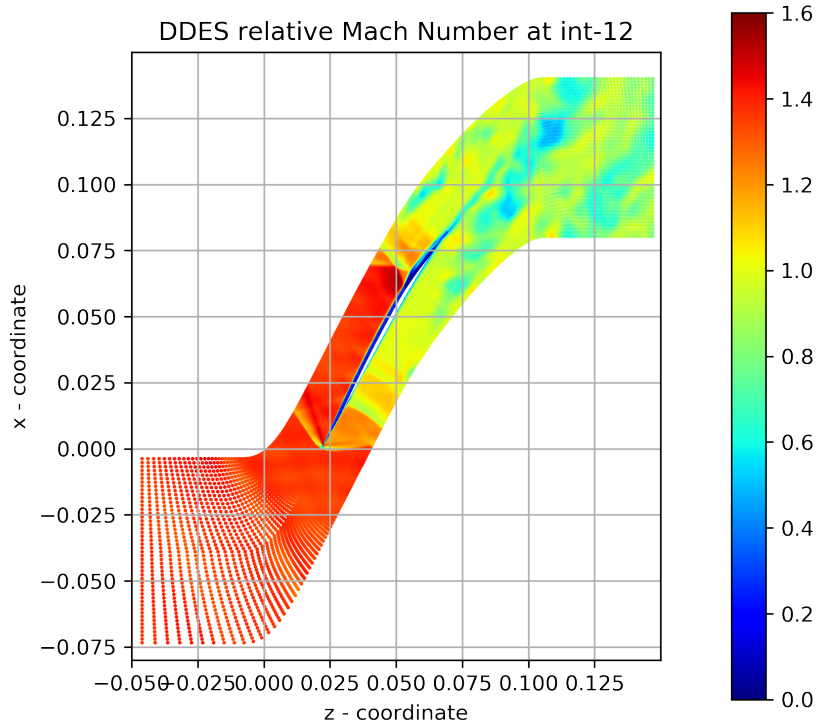


FIGURE C.24: DDES Mach number contour plot at int-12 mark

Appendix D

Code for direct formulation of noise analysis

```
# dask-noise.py
print("Loading Libraries...")
import os, sys
import csv
import platform
import numpy as np
import pandas as pd
import dask.dataframe as dd
import math
print("Loaded Libraries...")
print("Starting code...")
print("Loading directories...")
path_data = './flow-data/<folder_name>'
path_acu = './noise-data/<folder_name>/acu'
print("Loaded directories...")
print("Loading batch data...")
os.chdir(path_data)
batch_data = dd.read_csv('*/dat', delimiter=r"\s+", decimal='.')
print("Batch data done...")
print("Calculating batch averages...")
averages = pd.DataFrame(batch_data.groupby('nodenumber').mean().compute())
print("Batch averages done...")
print("Generating average pressure dataframe")
avg_static_p = pd.DataFrame({'pressure': averages['pressure']})
print("Generating average velocity dataframe")
avg_rel_v = pd.DataFrame(
    {'rel-velocity-magnitude': averages['rel-velocity-magnitude']})
print("Generating node coordinates...")
node_coords = pd.DataFrame({
    'x-coordinate': averages['x-coordinate'],
    'y-coordinate': averages['y-coordinate'],
    'z-coordinate': averages['z-coordinate']
})
del(batch_data)
print("Batch data deleted...")
```

```
print("Listing files...")
filelist = sorted(os.listdir(path_data)) [len(os.listdir(path_acu)):]
print("Starting noise analysis loop...")
for file in filelist:
    os.chdir(path_data)
    timestep = str(os.path.basename(str(file)))[7:-4]
    time_static_p = pd.DataFrame(pd.read_csv(file, delimiter=r"\s+"))
        .set_index('nodenumber')
    acoustic_p = time_static_p.subtract(avg_static_p, fill_value=None)
    spl_db = acoustic_p.apply(lambda x: 20 * np.log10(np.abs(x)/0.00002), axis=1)
    time_rel_vel = pd.DataFrame(pd.read_csv(file, delimiter=r"\s+"))
        .set_index('nodenumber')
    particle_v = time_rel_vel.subtract(avg_rel_v, fill_value=None).abs()
    sound_intensity = pd.DataFrame(
        acoustic_p.values*particle_v.values,
        index=acoustic_p.index)
    sil_db = sound_intensity.apply(
        lambda x: 10 * np.log10(np.abs(x)/1e-12), axis=1)
    acoustic_data = pd.concat(
        [node_coords,
        acoustic_p,
        spl_db,
        particle_v,
        sound_intensity,
        sil_db], axis=1)
    acoustic_data.columns =
        ['x-coordinate',
        'y-coordinate',
        'z-coordinate',
        'sound-pressure',
        'spl-db',
        'particle-velocity',
        'sound-intensity',
        'sil-db']
    os.chdir(path_acu)
    acoustic_data.to_csv(str('<filename>_') + str(timestep) + '.dat', sep=',')
    print(str('<filename>' + str(timestep) + '.dat done...'))
print("Exiting noise analysis loop...")
print("Script done, exiting.")
```

Appendix E

Folder Structure

```
flow-data
├── int-01 ... int-tip
│   └── ddes analysis output
└── lead pside sside tip trail
    └── ddes analysis output
```

```
noise-data
├── int-01-post ... int-tip-post
│   └── acu
│       └── sound-analysis-results
└── lead pside sside tip trail
    └── acu
        └── sound-analysis-results
```

```
results
├── coords
│   └── surface nodes coordinate files
├── fft
│   └── fft analysis results
├── rms
│   └── rms analysis results
└── plots
    └── output plots
```


Appendix F

Code for RMS computation

```
#rms.py
print("Loading Libraries...")
import os
import csv
import platform
import numpy as np
from scipy.fftpack import fft
import pandas as pd
import dask.dataframe as dd
import math
import matplotlib.pyplot as plt
print("Loaded Libraries...")

#PLGRID
print("Loading directories..")
path_acu = './noise-data/<folder_name>/acu'
path_rms = './results/rms'
print("Loaded directories...")

print("Loading batch data...")
os.chdir(path_acu)
batch_data = dd.read_csv('*1.dat',
                        delimiter=",",
                        decimal=',',
                        usecols=["nodenumber", "sound-pressure", "sound-intensity"])
batch_data = batch_data.set_index("nodenumber")
print("Batch data done...")

print("Calculating rms...")
rms = pd.DataFrame(batch_data.groupby('nodenumber').std().compute())
rms['rms_spldb'] = rms['sound-pressure'].apply(lambda x: 20*np.log10(x/0.00002))
rms['rms_sildb'] = rms['sound-intensity'].apply(lambda x: 10*np.log10(x/1e-12))

print("Saving...")
os.chdir(path_rms)
rms.to_csv(str('<filename>'), sep=",")
```

Appendix G

Code for discrete Fourier analysis

```
#fft.py
print("Loading Libraries...")
import os
import numpy as np
import pandas as pd
print("Loaded Libraries...")
print("Starting code...")

#PLGRID
print("Loading directories...")
path_acu = './noise-data/<folder-name>/acu'
path_fft = './results/fft'
print("Loaded directories...")

print("Getting filelist...")
os.chdir(path_acu)
filelist = sorted(os.listdir(path_acu))[0::10]

print("Starting batch loop...")
batch_data = pd.DataFrame()
for file in filelist:
    batch_data[file] = pd.read_csv(file).set_index('nodenumber')['sound-pressure']
    print(str(file) + " done...")

print("Calculating FFT...")
fft_data = batch_data.apply(lambda x: np.fft.fft(x), axis=1)

print("Saving FFT to dataframe...")
os.chdir(path_fft)
fft_data.to_csv('<filename>', sep=',')
print("Dataframe saved...")
print("Script completed...")
```

Bibliography

- [1] *ANSYS Documentation. Fluent Theory Guide*, 2015.
- [2] *Prometheus HPC maunual*, 2018. <https://kdm.cyfronet.pl/portal/Prometheus>.
- [3] K. S. Brentner and F. Farassat. An analytical comparison of the acoustic analogy and kirchhoff formulations for moving surfaces. *AIAA Journal*, 36(8):1379–1386, 1998.
- [4] C. Choi and P. Moin. Grid-point requirements for large eddy simulation: Chapman’s estimates revisited. *Physics of Fluids*, 24(1), January 2012. <https://aip.scitation.org/doi/full/10.1063/1.3676783>.
- [5] J. E. Crouse, J. S. David, C. Janetzke, and R. E. Schwirian. A computer program for composing blading from simulated circular-arc elements on conical surfaces. Technical Report TN D-5437, NASA Langley Research Center, 1969.
- [6] W. S. Cunnan, W. Stevans, and D. C. Urasek. Design and performance of a 427-meter-per-second-tip-speed two stage fan having a 2.40 pressure ratio. Technical Report TP-1314, NASA Langley Research Center, 1978.
- [7] N. Curle. The influence of solid boundaries upon aerodynamic sound. *Proceedings of the Royal Society. Series A, Mathematical, Physical and Engineering Sciences*, 231(1187):505–514, September 1955. <http://rspa.royalsocietypublishing.org/content/231/1187/505>.
- [8] J. D. Durrant and J. H. Lovrinic. *Bases of Hearing Sciences. Second Edition*. Lip-pincott Williams and Wilkins, 1984.
- [9] J. O. Hinze. *Turbulence*. McGraw-Hill Publishing Co., 1975.
- [10] M. J. Lighthill. On sound generated aerodynamically i. general theory. *Proceedings of the Royal Society. Series A, Mathematical, Physical and Engineering Sciences*, 211(1107):564–587, March 1952. <http://rspa.royalsocietypublishing.org/content/211/1107/564>.

- [11] M. J. Lighthill. On sound generated aerodynamically ii. turbulence as a source of sound. *Proceedings of the Royal Society. Series A, Mathematical, Physical and Engineering Sciences*, 222(1148):1–32, March 1954. <http://rspa.royalsocietypublishing.org/content/222/1148/1>.
- [12] J. Mosiezny. Github repository for nasa r67 input data and noise analysis, 2018. <https://github.com/JedrzejMosiezny/R67-data-analysis>.
- [13] T. Oetkier, H. Partl, I. Hyba, and E. Schleg. *The Not So Short Introduction to LATEX 2e*, 2018. <https://tobi.oetiker.ch/lshort/lshort.pdf>.
- [14] J. Smagorinsky. General circulation experiments with the primitive equations. *Monthly Weather Review*, 91(3):99–164, 1963.
- [15] P. R. Spalart et al. A new version of detached-eddy simulation, resistant to ambiguous grid densities. *Theoretical and Computational Fluid Dynamics*, 20:181–195, 2006.
- [16] P. R. Spalart, W. H. Jou, M. Strelets, and S. R. Allmaras. Comments of feasibility of les for wings, and on a hybrid rans/les approach. In *First International conference: Advances in DNS LES: Direct numerical simulation and large eddy simulation*, pages 137–148, 1997.
- [17] A. J. Strazisar, J. R. Wood, M. D. Hathaway, and K. L. Suder. Laser anemometer measurements in a transonic axial-flow fan rotor. Technical Report TP-2897, NASA Langley Research Center, 1989.
- [18] D. C. Urasek, W. T. Gorrel, and W. S. Cunnan. Performance of a two-stage fan having a low-aspect-ratio, first-stage rotor blading. Technical Report TP-1493, NASA Langley Research Center, 1979.
- [19] C. Wagner, T. Hüttl, and P. Sagaut. *Large-Eddy Simulation for Acoustics*. Cambridge University Press, 2007.
- [20] J. E. F. Williams and D. L. Hawkings. Sound generation by turbulence and surfaces in arbitrary motion. *Philosophical Transactions of the Royal Society of London. Series A, Mathematical and Physical Sciences*, 264(1151):321–342, May 1969. <http://www.jstor.org/stable/73790>.